



**HEAT TRANSFER DUE TO UNSTEADY EFFECTS AS INVESTIGATED IN A HIGH-
SPEED, FULL-SCALE, FULLY-COOLED TURBINE VANE AND ROTOR STAGE**

THESIS

Jonathan Roy Mason, Ensign, USN

AFIT/GAE/ENY/08-J04

DEPARTMENT OF THE AIR FORCE

AIR UNIVERSITY

AIR FORCE INSTITUTE OF TECHNOLOGY

Wright Patterson Air Force Base, Ohio

APPROVED FOR PUBLIC RELEASE; DISTRIBUTION UNLIMITED

The views expressed in this thesis are those of the author and do not reflect the official policy or position of the United States Air Force, United States Navy, Department of Defense, or the United States Government.

**HEAT TRANSFER DUE TO UNSTEADY EFFECTS AS INVESTIGATED IN
A HIGH-SPEED, FULL-SCALE, FULLY-COOLED TURBINE VANE AND
ROTOR STAGE**

THESIS

Presented to the Faculty

Department of Aeronautics and Astronautics

Graduate School of Engineering and Management

Air Force Institute of Technology

Air University

Air Education and Training Command

In Partial Fulfillment of the Requirements for the
Degree of Master of Science in Aeronautical Engineering

Jonathan R. Mason, BS

Ensign, USN

June 2008

**HEAT TRANSFER DUE TO UNSTEADY EFFECTS AS INVESTIGATED IN
A HIGH-SPEED, FULL-SCALE, FULLY-COOLED TURBINE VANE AND
ROTOR STAGE**

Jonathan R. Mason

Ensign, USN

Approved:

//SIGNED//

Dr. Mark F. Reeder (Chairman)

03 JUNE 08

Date

//SIGNED//

Dr. Marcus D. Polanka (Member)

03 JUNE 08

Date

//SIGNED//

Dr. Paul I. King (Member)

03 JUNE 08

Date

Abstract

Experiments were conducted to examine the effects of film cooling on a gas turbine engine's high-pressure turbine section. The focus for this effort was in the tip/shroud region of a rotor stage and a high pressure turbine vane. A primary goal was to understand the unsteady flow effects. Attempts were also made to characterize the effects as caused by the fully-cooled rotor stage. Data for this investigation was taken at the U.S. Air Force's Turbine Research Facility (TRF), a transient blow-down facility with instrumentation fitted to a full-scale, high-speed, fully-cooled vane and rotor stage of proprietary design. Measurements of pressure, temperature, and heat flux were taken at flow conditions non-dimensionally matched to actual engine operation. From this high speed data the relevant film-cooling parameters (heat transfer coefficients, film cooling effectiveness, and overall effectiveness) were determined over a range of operating conditions. Of specific interest were the high frequency events associated with the blade passage frequency on both the vane and shroud surfaces. It was found that tip flow and vane wake-rotor interaction result in noticeable heat flux variations in time.

For our deployed brethren.

Acknowledgments

My sincerest thanks for the guidance, help, and patience of my advisers,
committee, and the men of the Air Force's Turbine Research Facility.

Jonathan R. Mason

Ensign, USN

Table of Contents

	Page
Abstract.....	iv
Acknowledgements.....	vi
Table of Contents.....	vii
List of Figures.....	x
List of Tables	xiii
List of Symbols	xiv
List of Acronyms	xvi
1. Introduction & Background.....	1
1.1 Film Cooling	1
1.2 Unsteadiness	2
1.3 Film-Cooling Parameters	3
2. Literature Review.....	4
2.1 Film-cooling.....	4
2.2 Unsteady Effects	5
2.2.1 Vane Unsteadiness	6
2.2.1.1 Vane-Rotor Interaction: Shock Reflection	6
2.2.1.2 Vane-Rotor Interaction: Inter-stage compression	11
2.2.2 Airfoil Tips/Rotor Shrouds	13
3. Experimental Setup.....	16
3.1 Experimental Facility.....	16
3.1.1 Parameter Matching	17
3.1.2 Facility Overview.....	18

3.1.2.1	<i>Combustor Simulator</i>	20
3.1.2.2	<i>Coolant System</i>	23
3.1.2.3	<i>Vane and Rotor Test Section</i>	24
3.1.3	<i>Experimental Procedure</i>	27
3.2	Instrumentation	30
3.3	Heat Flux Gauges.....	35
3.4	Test Matrices.....	39
4.	Methodology	42
4.1	Derivation of Film-Cooling Parameters.....	42
4.2	Popp Method of Determining Film-Cooling Parameters.....	45
4.3	Data Reduction: Time-Resolved.....	50
4.4	Time-Averaged Data Reduction Methods	58
4.4.1	<i>Overall Effectiveness</i>	58
4.4.2	<i>Adiabatic Effectiveness& Heat Transfer Coefficient: Popp Method</i>	62
4.5	Time-Resolved Data Reduction Methods.....	66
5.	Results and Analysis—Vane Stage.....	76
5.1	Time-Resolved Results	76
5.2	Time-Averaged Results & Film-Cooling Parameters.....	83
6.	Results and Analysis--BOAS.....	94
6.1	Time-Resolved Results	94
6.2	Time-Averaged Results	99
7.	Conclusions and Recommendations	102
7.1	Research Conclusions	102
7.2	Significance of Research.....	104
7.3	Recommendations for Future Research	104

Appendix: Determination of the True Driving Temperature	105
Bibliography	115
Vita.....	119

List of Figures

Figure 1: Film-cooled vane example	2
Figure 2: Shock-coolant film interaction (taken from Smith et al., 2000)	7
Figure 3: Vane shock wake travel and reflection	8
Figure 4: Unsteady, normalized pressure disturbances on vane suction surface (from Urbassik, 2003).....	10
Figure 5: Isentropic compression between vane and rotor stages	12
Figure 6: Unsteady heat flux, temperature, and Nusselt number in vane-rotor gap.....	12
Figure 7: Tip vortex flow	14
Figure 8: TRF experimental apparatus	18
Figure 9: Schematic of TRF	19
Figure 10: View of TRF combustor simulator, coolant delivery, and test section	20
Figure 11: Inlet Temperature and Pressure Profiles (from Barringer, et al., 2007).....	21
Figure 12: Total pressure losses at vane exit.....	22
Figure 13: Temperature profiles at vane exit.....	22
Figure 14: Coolant delivery system.....	23
Figure 15: Coolant delivery to vanes.....	24
Figure 16: Vane coolant schemes.....	25
Figure 17: Tip coolant schemes.....	25
Figure 18: Corrected speed maintenance.....	28
Figure 19: Sample test data collection.....	29
Figure 20: Instrumentation on shroud and vanes.....	31
Figure 21: Percent span depiction	32
Figure 22: Vane heat flux gauge mounting at 60 % span.....	33
Figure 23: Vane heat flux gauge mounting at 24 % span.....	33
Figure 24: 60 % Span pressure transducers.....	34
Figure 25: BOAS-mounted gauges	34
Figure 26: Heat flux gauge design.....	36
Figure 27: Sample heat flux gauge data	39
Figure 28: Film-cooled airfoil experimental values	44
Figure 29: Temperature, heat flux histories in uncooled experiment (from Popp et al., 2000).....	47
Figure 30: Regression of heat flux versus temperature difference (from Popp et al., 2000).....	48
Figure 31: Graph of normalized heat flux and driving temperature difference (taken from Popp, et al., 2000).....	49
Figure 32: Sample time-resolved pressure gauge traces	50
Figure 33: Sample time-resolved heat flux gauge traces: 74 % SS vane	51
Figure 34: Sample time-resolved heat flux gauge traces: 47 % x/C BOAS	51
Figure 35: BOAS-mounted pressure gauge: sample trace.....	52
Figure 36: Sample FFT: 47 % x/C BOAS thin-film temperature gauge	53
Figure 37: Sample FFT by engine order, 47 % x/C BOAS thin-film temperature gauge	54
Figure 38: Area view of sample FFT, 47 % x/C BOAS temperature gauge	55
Figure 39: Sample engine order FFT, 47 % x/C BOAS pressure gauge	56
Figure 40: Sample engine-order FFT, 90 % SS vane embedded thermocouple temperature.....	56

Figure 41: Sample engine-order FFT, 90 % PS vane pressure gauge	57
Figure 42: Overall effectiveness temperature histories--Run 1, 47 % x/C BOAS	59
Figure 43: Overall effectiveness temperature histories--Run 1, 90 % SS vane, 60 % span	60
Figure 44: Heat flux histories—Run 1, 47 % x/C BOAS and 90 % SS vane, 60 % span	61
Figure 45: Overall effectiveness histories in time of interest--Run 1	61
Figure 46: Temperature histories--Run 1, 47 % x/C BOAS gauge	63
Figure 47: Popp-style plot--Run 1, 47 % x/C BOAS gauge	64
Figure 48: Popp-style plot--Run 1, 86 % x/C BOAS gauge	64
Figure 49: Popp-style plot--Run 1, 63 % PS vane gauge, 60 % span	65
Figure 50: Popp-style plot—Run 1, 90 % SS vane gauge, 60 % span	65
Figure 51: Sample ensemble-averaged pressure data, 47 % x/C BOAS pressure gauge	68
Figure 52: Sample ensemble average, 47 % x/C BOAS pressure gauge	69
Figure 53: Sample freestream-normalized ensemble average, 47 % x/C BOAS pressure gauge .	70
Figure 54: Sample freestream-normalized, unsteady-only ensemble average, 47 % x/C BOAS pressure gauge	70
Figure 55: Blade phase convention	71
Figure 56: 47 % x/C BOAS-mounted pressure gauge: tip layouts	72
Figure 57: Sample phase-locking data gathering: 47 % x/C BOAS thin-film temperature and pressure gauges	73
Figure 58: Sample ensemble-averaged phase-locked blade passages: 47 % x/C BOAS thin-film temperature and pressure gauges	73
Figure 59: Ensemble-averaged heat flux, 45 % SS vane, 60 % span	74
Figure 60: Ensemble-averaged heat flux, 47 % x/C BOAS gauge	75
Figure 61: Pressure disturbance along vane surface, 60 % span, Run 3, 3.5-3.7 sec	77
Figure 62: Temperature disturbance (thin-film gauge) along vane, 60 % span, Run 3, 3.5-3.7 sec	78
Figure 63: Normalized temperature disturbances along vane suction side, 60 % span	79
Figure 64: Unsteady pressure variations on vane, 60 % span	81
Figure 65: Unsteady temperature variations on vane, 60 % span	81
Figure 66: Mean heat flux across vane surface, 60 % span	84
Figure 67: Popp-style plot for 14 % SS vane gauge, 60 % span	85
Figure 68: Popp-style plot for 62 % PS vane gauge, 60 % span	85
Figure 69: Popp-style plot for vane: 60 % span, 62 % PS	89
Figure 70: Adiabatic film-cooled effectiveness along vane surface, 60 % span	90
Figure 71: Heat flux coefficient along vane surface, 60 % span	90
Figure 72: Compound shaped holes, overall effectiveness, 60 % span	92
Figure 73: Compound shaped holes (second airfoil), overall effectiveness, 60 % span	93
Figure 74: Compound shaped holes, overall effectiveness, 90 % Span	93
Figure 75: Pressure disturbances along BOAS, Run 3, 3.5-3.7 sec	95
Figure 76: Temperature disturbances along BOAS, Run 3, 3.5-3.7 sec	96
Figure 77: Comparison of tip cooling schemes, 28 % axial chord	97
Figure 78: Unsteady pressure variations on BOAS	98
Figure 79: Unsteady temperature variations on BOAS	98
Figure 80: Popp-style uncooled plot for BOAS	100

Figure 81: Heat flux coefficients along BOAS	101
Figure 82: Overall effectiveness along BOAS	101
Figure 83: Normalized total pressure profile, vane inlet	105
Figure 84: Normalized total temperature profile, vane inlet	106
Figure 85: CFD-predicted local pressure ratio across vane surface	106
Figure 86: Vane local Mach numbers	107
Figure 87: Sample vane local recovery temperatures.....	108
Figure 88: Normalized exit total pressure profile, rotor exit.....	110
Figure 89: Normalized exit total temperature profile, rotor exit	110
Figure 90: Total pressure loss profile through test section.....	111
Figure 91: Total temperature loss profile through test section.....	111
Figure 92: Temperature and pressure ratios across test section	112
Figure 93: Experimentally-gathered local pressure ratios across BOAS	113
Figure 94: BOAS local Mach numbers	114
Figure 95: Sample BOAS local recovery temperatures.....	114

List of Tables

Table 1: Sample matching parameters of real engine conditions to experimental facility	17
Table 2: Tip clearances and schemes	26
Table 3: Time-resolved run parameters.....	40
Table 4: Time-averaged run parameters	41
Table 5: Heat flux variation at 60 % span	83
Table 6: X, Y pairs for Popp plotting	86
Table 7: Values for Popp plotting	88

List of Symbols

English Symbols

C_p	Coefficient of Pressure
c	Specific Heat Capacity
f	Frequency (Hz)
h	Convective Heat Transfer Coefficient (W/sq.m-K)
k	Thermal Conductivity (W/m-K)
l	Characteristic Length
M	Mach Number
N, n	Number of Blades or Summation Variable
P	Pressure (Pa)
Pr	Prandtl Number
q	Heat Transfer (W)
R	Gas constant (J/mol-K)
r	Rotor Blade Radius
r	Recovery Factor
Re	Reynolds Number
T	Temperature (K)
v	Velocity
x/C	Ratio: Axial Position/Total Axial Chord of Airfoil
x/S	Ratio: Surface Length/Total Surface Length
Z/S	Ratio: Spanwise Position/Total Span of Airfoil (or y/B)

Greek Symbols

Δ	Difference
η	Adiabatic Film-Cooling Effectiveness
γ	Ratio of Specific Heats
ρ	Density (g/cub.cm)
ξ	Total Pressure Losses
ϕ	Overall Effectiveness
Θ	Temperature Ratio
μ	Dynamic Viscosity (kg/m-s)

Subscripts

aw	Adiabatic Wall
c	Coolant
d	Difference (Temperature)
i	Inside Feed Plenums of Airfoil
f	Film (Temperature) or Film-Cooled (Heat Transfer)
m	Metal (Temperature)
r	Recovery (Temperature)
s	Static (Temperature)
t	Total (Temperature, Pressure)
w	Wall
∞	Freestream

Superscripts

"	Rate, per Unit Area (Heat Transfer)
---	-------------------------------------

List of Acronyms

FFT	Fast Fourier Transform
BOAS	Blade Outer Air Seal (Rotor Shroud)
ID	Inner Diameter
LE	Leading Edge
OD	Outer Diameter
PS	Pressure Side
RPM	Revolutions per Minute
SS	Suction Side
TE	Trailing Edge
TRF	Turbine Research Facility

HEAT TRANSFER DUE TO UNSTEADY EFFECTS AS INVESTIGATED IN A HIGH-SPEED, FULL-SCALE, FULLY-COOLED TURBINE VANE AND ROTOR STAGE

1. Introduction & Background

1.1 Film Cooling

Gas turbine engines and generators have become commonplace in their seventy years of existence. Though already a highly effective means of providing aerospace and naval propulsion and power generation, more efficient implementation of the technology is constantly being pursued. Efficiency and greater power delivery are highly dependent upon turbine inlet temperatures in these engines; however, raising this temperature beyond safe operating range for the metallic components of the vane and rotor stages can be an unsafe practice.

To resolve this dilemma, methods of cooling the airfoils of the turbine stages of these engines have been established. The predominant method of cooling vane and rotor airfoils, having been used for over thirty years, involves the bleeding of pressurized air from compressor stages and feeding back into the turbine section. In modern gas turbine film cooling, this bled air flows through drilled holes via internal passages in the individual airfoils. The ejected air forms a film over the airfoil surface, cooling the metal and impeding the hot freestream gas from heating the airfoils. With these methods of ‘film cooling,’ turbine inlet temperatures much higher than the metal’s sustainable fatigue-life temperature can be achieved, producing engines with higher efficiencies and

greater thrust. An example of how this film coolant might be employed in a vane blade is seen in Figure 1.

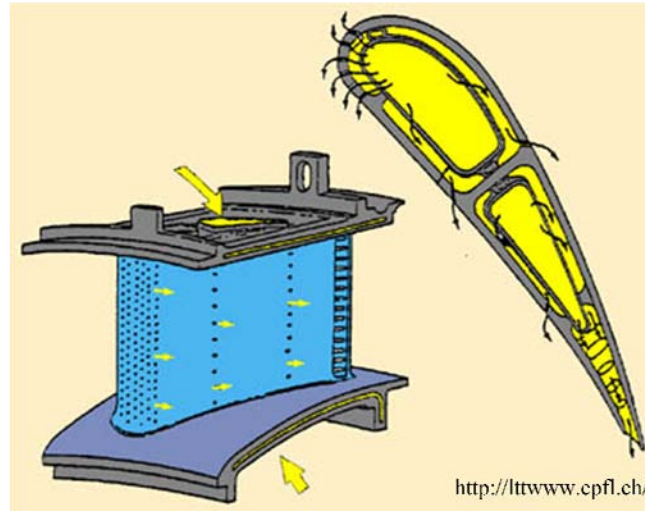


Figure 1: Film-cooled vane example

A myriad of concepts for implementing these film cooling techniques in today's gas turbines have been developed. Engine designers and maintainers depend upon the effective delivery of the coolant flow and its dependability in order to assure the reliability of the components of these airfoils. A review of many of the effects which affect the success and shortcomings of different film cooling schemes is seen in a 2006 review article by Bogard and Thole (2006: 249-270).

1.2 Unsteadiness

Of particular interest in the current study are both (1) the effectiveness of film cooling techniques on vane stages subject to the unsteady effects of rotor blade passage and (2) the impact of these same unsteady effects on the outer shroud of the rotor stages. This becomes especially important when considering that the effects of cyclic unsteadiness in turbomachinery (variations in pressures, temperatures, and heat transfer)

can lead to high-cycle fatigue in gas turbine stages. The induced aerothermodynamic unsteadiness can reduce the effectiveness of film cooling in the vane and rotor stages of turbine engines. Even today, fairly little experimentation has been performed on these unsteady effects in operating conditions which can truthfully represent the complex nature of a full-scale, high-speed rotating vane and rotor stage.

1.3 Film cooling parameters

Two primary parameters have been used as the industry standard for determining the effectiveness of employed film-cooling techniques: adiabatic film-cooling effectiveness (η) and film-cooled heat transfer coefficient (h_f). These will be discussed in further detail later, but are introduced here for the purposes of guiding further discussion:

$$q_{f,adaibatic}'' = h_f(T_{aw} - T_w)$$

and

$$\eta = \frac{T_{\infty} - T_{aw}}{T_{\infty} - T_{c,exit}}$$

Where heat flux (q) into a surface is a function of a convective heat transfer coefficient (h) and a temperature difference ($T_{aw} - T_w$). Adiabatic effectiveness is a function of the temperatures driving the heat transfer and those driving the cooling. These are determined in test setups that do not resemble the setup of the current study; however, they can be gained from the current study, as will be discussed later in further detail.

2. Literature Review

2.1 Film cooling

It should be noted that many of the techniques used to increase film cooling effectiveness will many times increase external heat transfer coefficients locally, adding difficulty to the design of cooled airfoils. As previously mentioned, a multitude of factors and operating parameters have been identified as critical in the resulting effectiveness of a film-cooling design. One operating parameter identified as of importance is the ratio of massflows (freestream and coolant). Higher massflows of coolant will intuitively cool more effectively until separation phenomenon (liftoff from the surface) occurs, at which point the film coolant loses its effect.

Also of importance are ejection hole geometries and schemes. Current technology in film-cooled airfoils employ slots and holes exiting at varying angles (with orientation to the surface and freestream). Coolant holes ideally will eject coolant flow that will effectively cover the surfaces exposed to hot freestream gases. In order to accomplish this, appropriate spacing, width, and length of the holes must be selected. In the current study, the airfoils chosen for study were angled, fan-shaped holes. Firstly, holes were inclined with respect to the surface (that is, the holes were not normal to the surface at the ejection point, providing for coverage immediately downstream of the hole, rather than suffering liftoff at this downstream point). The fan-shaping of the holes also provides for width-wise coverage along the airfoil surface downstream of the ejection holes (Umholtz, 2007). Of course, the effectiveness of the film-coolant scheme

employed is dependent upon the outlying pressures and temperatures seen in the turbine, a function of the unsteadiness seen in the vane and rotor stage.

2.2 Unsteady Effects

As mentioned previously, inherent periodic unsteadiness in turbomachinery can affect high-cycle fatigue in gas turbine stages. Effects of unsteadiness are defined as those both due to the turbulent nature of airflow and also the motion in turbomachinery; however, of primary concern in the studies of current interest are those effects due to turbomachinery motion. The periodic variable pressure, temperature, and heat transfer effects observed in vane and rotor stages has been observed to develop from the interaction between rotating rotor blades and the surrounding components. Film-cooling is not specifically designed around these unsteady effects. This creates a situation where investigation into the magnitude and impact of the inherent unsteadiness is not accounted for in a turbine engine environment. This is an area in need if turbines are to be properly designed and maintained.

While the aforementioned high-frequency interactions do certainly occur and affect most areas of the turbine stages, two are of chief interest. Firstly, as a rotor blade rotates, its tip passes very close to the metallic shroud in which it is encased. This passage causes high fluctuations in heat flux affecting the shroud, or blade outer air seal (BOAS). Also, as the leading edge of each rotor blade passes behind the upstream vanes, it causes similar high-frequency fluctuations along the surface of the vane.

2.2.1 Vane Unsteadiness

2.2.1.1 Vane-Rotor Interaction: Shock Reflection

Unsteadiness in turbines has been shown to produce inherent losses due to the nature of inviscid pressure variations due to relative motion between these vane and rotor stages, as well as shock & wake interactions. Of importance in understanding this interaction is characterizing the flow trailing a blade. Total and static temperatures in unsteady vane shock wakes were investigated in a transonic cascade facility at the Von Karman Institute for Fluid Dynamics (Sieverding et al., 2003: 11). Temperature data demonstrated hot spots at the outer borders of passing wake and a cold region near the center of the wake. The same trend profile was observed for the values of total temperature in these wakes. The pressure profile within this wake revealed a very low pressure region in the center of these wakes, with peaks in pressure at the edges. As the leading edge of downstream blades passes through this region of variant temperature and pressure, effects are threefold. Clearly, the driving temperature for heat transfer fluctuates. Secondly, as the pressure field external to the film-cooling jets varies, modulation of the film-cooling jets also occurs. This results in varying effectiveness in the showerhead-type region of these blades' leading edges. A tertiary effect of this wake's presence is the unsteadiness of the boundary layer upon a surface it strikes (Mailach and Vogeler, 2003: 1). In an investigation into the unsteady heat transfer conducted in a transonic blowdown wind tunnel (Smith et al., 2000), interaction between a vane trailing edge shock and the downstream rotor blade was simulated using a shock-tube generated shock in a cascade setup. It was shown by that the unsteadiness of heat flux was relatively independent of the unsteadiness of the heat transfer coefficient.

Shadowgraph visual imagery showed a strong interaction between the traveling shock wave and the layer of cooling air along the blade (previously-mentioned modulation in film-cooling jets), as shown in Figure 2. While this is not necessarily demonstrative of the exact occurrences seen in this study, it does introduce the effect of the shocks present in a transonic stage such as the one used in this experiment. Therefore, the heat flux was influenced by the coolant film's temperature variation due to the passing shock. Furthermore, the primary culprit in the unsteadiness of film effectiveness was determined not to be the shock's movement itself, but rather the temperature difference within the shock (from inner portions to outer boundaries).

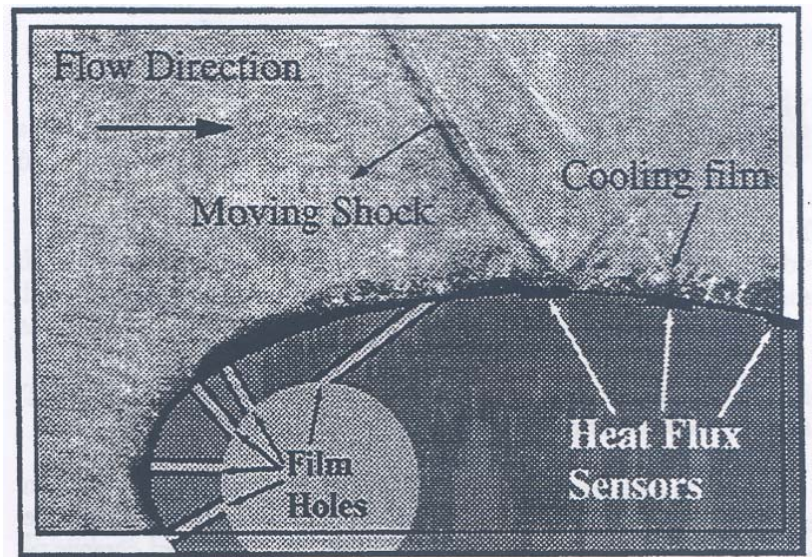


Figure 2: Shock-coolant film interaction (taken from Smith et al., 2000)

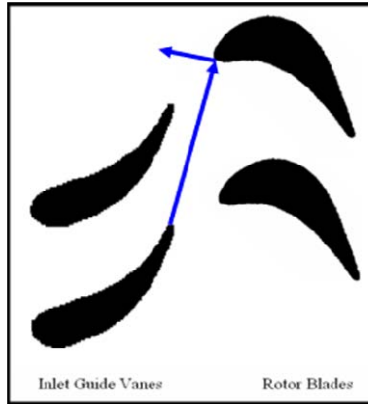


Figure 3: Vane shock wake travel and reflection

Important to the vane stage is the effect of this shock wake as it is reflected back upstream by a passing blade. A visual representation of this shock wake's travel from the trailing edge of the vane back upstream is seen in Figure 3. The results of this shock reflection phenomenon would be seen both along the blade surface downstream of the vane shock, as well as on the surfaces of the vane onto which it reflects and impinges.

In a study on a 1.5-stage high-pressure turbine by Miller et al. (2003: 33-39), vane wake-induced unsteadiness was observed, as well; however, alternate reasoning for the unsteadiness was presented. The shocks were found to have negligible effects on unsteady surface pressure and blade loading. Therefore, it was expected that driving temperature unsteadiness would largely correlate to heat transfer unsteadiness. Though oscillations in film-cooling effectiveness (η) may be observed, it would be the variations in overall effectiveness and film-cooled heat transfer that will most markedly characterize unsteady effects. This unsteadiness, of course, will be most pronounced on the surface where the shocks directly impinge (Didier, Denos and Arts, 2002: 6).

In experiments conducted previously at the U.S. Air Force's Turbine Research Facility (TRF) with an uncooled full turbine stage (high pressure vane and rotor, the same

geometry and setup as used in the current study), unsteady pressure measurements were taken and analyzed (Urbassik 2003). Propagation of the shock reflection back upstream was characterized in this study. In this vane and rotor stage, it was concluded that higher overall Nusselt numbers were seen along the aft portion of the vane's suction side (Polanka et al., 2002: 11), the surfaces along which this reflected shock would most directly impinge. This was possibly due to flow separation and changes in local driving temperature, respectively, resulting in higher heat transfer.

Figure 4 shows the variations of static pressure on the upstream vanes. Data is presented by first subtracting the average static pressure (P_{ave}) through the trace from the instantaneous measurements (P), and then normalizing by the upstream total pressure (P_{U_t}). This provides an accurate representation of the pressure disturbances on the vane's suction surface; while variations were also seen as on the pressure surface, they were not pronounced significantly. It was seen that, as the shock reflection traveled back upstream, pressure variation weakened. Due to the nature of the wake (with pressure and temperature variations from outside to inner portions), it can be expected that variations in temperature due to shock impingement are similar in fluctuation. In this study it was also seen that, due to flow being choked through the test section, changes in pressure ratios had no significant effects in the experimental transonic rig (Urbassik, 2003).

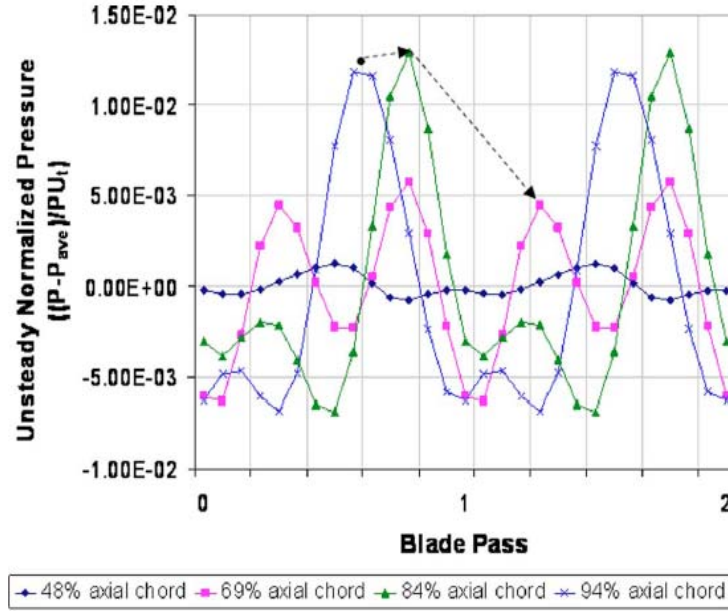


Figure 4: Unsteady, normalized pressure disturbances on vane suction surface (from Urbassik, 2003)

While of prime interest are the flow physics (resulting in heat transfer effects), it must be realized that the aforementioned unsteadiness results in efficiency losses through the turbine stages. A two-dimensional, second-order compressible Navier-Stokes-based CFD analysis has demonstrated that these losses were highest at higher inlet Mach numbers and smaller vane-to-rotor gaps (Moczala et al., 2003: 2, 9).

Finally, tests have been conducted to characterize effects of unsteady pressure distribution from a leading compressor blade stage onto stator vanes (Mailach, 2003: 1). While the interaction of a row of blades with a downstream guide vane stage is not the focus of this study (as only a single stage was rigged for experimentation), results from pressure and temperature data downstream of the test article may be used in research to the end of supporting and aiding this rotor TE-vane LE interaction.

2.2.1.2 Vane-Blade Interaction: Inter-Stage Potential Interactions

Shock impingement has been readily proven to result in unsteadiness of vane and blade aerodynamics, flow physics and heat transfer. Less widely-investigated is the phenomenon of rapid isentropic compression/heating, and resultant upstream potential variations which occurs in the gap between a rotor and vane stage. This occurs as a blade's leading edge passes by an upstream trailing edge of an inlet guide vane, as seen in Figure 5 (Johnson, et al., 1988). This causes high local driving temperatures and heat fluxes, most specifically along the rotor shroud surface; the effect of this heating as it convects upstream to the vane surface is of interest to the current study. In a test conducted in an uncooled vane and rotor rig, it was confirmed that the blade passage behind the trailing edge of a vane resulted in very quick heating of the fluid between the metal surfaces (at this point in very close immediacy to one another), consequently resulting in potential modulations and high heat flux values on the blade (Atkins et al., 2008: 8). The cyclic variation due to this unsteadiness saw its peak at 46-percent vane phase (that is, just before the leading edge of the blade passes directly behind the vane's trailing edge), depicted in Figure 5 and reproduced in Figure 6. This was also seen to be of significance in the driving temperature of heat transfer (T_r) in the blade tip region, causing variations in the freestream temperature immediately downstream of the trailing edge of the blade to elevate heat flux in this near-endwall region.

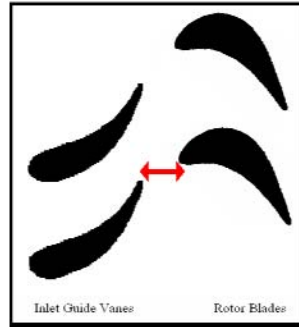


Figure 5: Isentropic compression between vane and rotor stages

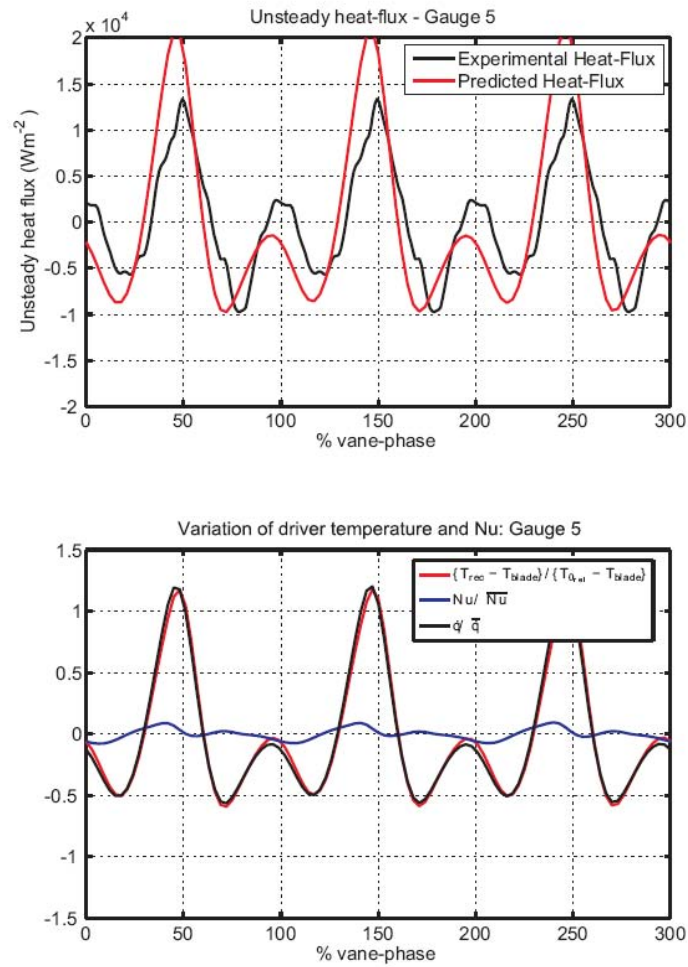


Figure 6: Unsteady heat flux, temperature, and Nusselt number in vane-rotor gap

(Taken from Atkins et al., 2008)

Agreement among the varying pressure gradient, driving temperature, and heat flux were seen with vane-phase passage, with the highest peaks in each occurring at this

46-percent vane-phase point, seen in Figure 6. While this represents the occurrences in the near-tip locality, it is characteristic of the trends throughout the area. This phenomenon therefore becomes of interest in unsteadiness along the vane surface.

2.2.2 Airfoil Tips/Rotor Shrouds

While full-scale investigations into heat transfer occurrences in the regions of airfoil tips and endwalls have been limited due to the cost and difficulty of such tests in fully-rotating apparatuses, many efforts (especially in cascade setups and modeling) have been undertaken in this area. The rotor blade's tip's flow physics are certainly of major importance in comprehending the heat transfer in the shroud region. Principally responsible for variations in rotor tip flow and heat transfer is the previously-explored vane-rotor interaction, which causes disturbances in the tip-gap region flow. Rotor tip passage produces significant pressure variations at 96.5 % span of the rotor blade at high frequencies (Urbassik 2003). These were observed at the vane-pass frequency (that is, the frequency at which the blade passes an upstream vane). These pressure variations (also, of course, occurring along the shroud) can result in near doubling of heat transfer in the tip gap region (Metzger and Rued, 1989). The rotor blade's passage led it through the guide vane-induced positive pressure gradient (in its moving frame of reference). Again, this causes the fluid's temperature to increase, moving through into the tip-gap region and causing higher blade-tip and shroud heat flux values (Atkins et al., 2008: 8). It was also noted in this study that CFD turbulence modeling was not highly accurate in predicting the local Reynolds numbers and driving temperatures in high-speed rotating rigs.

When investigating the effects of rotor passage along shroud surfaces, understanding of the complex flow field is necessary. The prime driver of aerodynamic unsteadiness in this region is the passage secondary flow (caused by the pressure difference between the rotor blade's pressure and suction surfaces, similar to the phenomenon of downwash in a finite wing). On the shroud surface, this results in a pressure gradient and velocity gradient (Herzig et al., 1954). Film-cooled tips (that is, airfoils which incorporate blowing along the blade tip) have shown to retard secondary flows by reenergizing the boundary layer in this region. This coolant flow is swept toward the blade's suction surface by the tip vortex, as shown in Figure 7 . Because of this travel of the coolant flow, the effects of the cooling fluid are highly pronounced with the passage of each blade's suction side, but diminished with the corresponding pressure sides. Though this blowing of cooling air does result in a lower average temperature along the endwall region, it can also result in higher mixing of flow--and thus higher heat transfer (Simon and Piggush, 2006: 303).

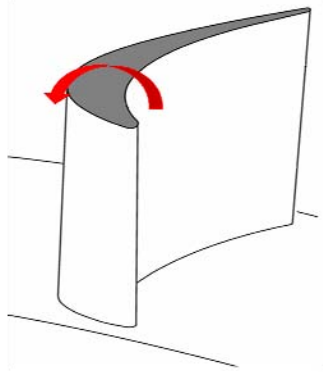


Figure 7: Tip vortex flow

In a study performed on a full-scale, uncooled high-pressure turbine stage, heat transfer results from the pressure gradient characteristic of blade endwalls were observed (Chana and Jones, 2003: 518). Heat flux along the shroud reached a minimum as the

blade's suction surface approached, then increased rapidly, reaching a maximum with the passage of the blade's pressure side. Largest variations were seen at the thickest portion of the blade, and smallest variations were seen toward the latter, thinner portion of the blade.

In a test conducted at TRF previously (Polanka et al., 2002: 11), rotor tip and shroud heat transfer and pressure measurements were gathered at varying flow parameters. The rig used was uncooled and had minimal tip clearance (for minimal losses across the rotor stage). Heat transfer levels along the blade tip and shroud region were seen to be as great as those at the stagnation points of the rotor blade airfoils.

Work to the aforementioned end also resulted in the general trend predictions of a three-dimensional Reynolds-averaged Navier-Stokes CFD simulation. Further examination of the experimental results concluded that the effects of varying tip clearances were much more pronounced along the aft portion of the rotor airfoils, most specifically after the throat of the stage (Polanka et al., 2002: 6). Validation of these predictions showed not only high-frequency positive variations in driving temperature, but also *negative* heat flux (due to local driving temperatures dropping below local wall temperatures at specific points in the blade pass period). This causes even greater concern for high-cycle fatigue. Because of the enthalpy extracted from the working fluid (especially after the majority of the work has been done upon the fluid—that is, toward the trailing edge of the blade), this freestream temperature drop occurs at a specific point along each blade passage (Clark, et al., 2006: 594).

3. Experimental Setup

As mentioned earlier, current testing and analysis was aimed toward more full understanding of unsteady heat transfer and loading in a turbine section, and the effects of film cooling in such an environment. The analysis of these experiments focused toward the tip/shroud region of the rotor stage and on the suction surface of a high pressure turbine vane.

Though significant research has been performed in these areas, measurements and results truly representative of actual unsteady heat transfer occurrences in turbine engines are difficult to obtain. This is due to (1) the survivability of instrumentation in the high temperature environment of the vane and rotor stages and (2) the cost and complexity of experimenting on full-scale, full-speed equipment. Current testing allows results to be analyzed from such a truly representative environment.

3.1 Experimental Facility

Experimentation was conducted at the U.S. Air Force's Turbine Research Facility, a transient blow-down facility, between 2005 and 2006. The facility is designed to conduct experimentation on air-breathing turbine engines, including gathering aerothermal and heat transfer data (Haldeman et al., 1992). Previous experimentation, cited extensively in the review of current literature, has collected data on this same vane and rotor section but in uncooled and vane-only setups.

3.1.1 Parameter Matching

As indicated earlier, establishing actual engine conditions would be impractical for experimentation, as instrumentation would not survive in such an environment. However, TRF allows the testing to nondimensionally match vital parameters for current testing to provide results which simulate (1) the aerothermodynamic environment of a film-cooled turbine section, and (2) the modes of heat transfer (convection and conduction) present in the metallic components therein. A table representative of testing parameters and nondimensional matching is seen in Table 1.

Table 1: Sample matching parameters of real engine conditions to experimental facility

	<u>Engine</u>	<u>TRF</u>		<u>Engine</u>	<u>TRF</u>
Fluid	Air	N ₂ +CO ₂	✓ T(gas)/T(metal)	1.66	1.66
Inlet Temp (K)	2130	500	✓ T(gas)/T(coolant)	2.22	2.22
Metal Temp (K)	1280	300	✓ Pressure Ratio	3.0	3.0
Coolant Temp (K)	960	225	✓ Reynolds No.	2.3x10 ⁶	2.3x10 ⁶
Pressure (kPa)	2750	700	✓ Mach No.(axial)	0.4	0.4
Rotor Speed (rpm)	12000	5800	✓ Corrected Speed	260	260
Mass Flow (kg/s)	45	19.5	✓ Mass ratio	0.133	0.133
Coolant Flow (kg/s)	6	2.6	✓ Specific Heat Ratio	1.3	1.3
Power (MW)	25	2	✓ Prandtl No.	0.695	0.713

Nondimensional flow parameters used for aerothermodynamic matching in TRF include Reynolds number, Mach number, engine pressure ratio, mass ratios, corrected speed, Prandtl number, gas-to-coolant temperature ratio, and corrected massflow. Nondimensional heat transfer parameters used for matching heat transfer conditions include temperature ratios, Reynolds number, Mach number, Prandtl number, and specific heat ratios. This heat transfer matching results not in an equivalent heat flux through the turbine, but rather matched Nusselt numbers, Nu , (the ratio of convective to conductive heat transfer).

It is of importance to note that the complex flow fields in this study (especially the tip flow region) are due in part to interaction between the rotating motion of the blade tip and the axial motion of the freestream flow. Matching corrected speed allows experimentation at a condition which matches the vectored components of flow (in the relative frame of the blade) in an actual engine representative. This is represented as wheel speed over the speed of sound in the blowdown facility:

$$r\omega / (\sqrt{\gamma}RT) \quad (1)$$

Where r is the radius of the blade, ω is the radial speed, and $(\sqrt{\gamma}RT)$ represents the speed of sound in the test section. Fuller description of this matching will follow.

3.1.2 Facility Overview

A view and diagram of the facility's setup are shown in Figure 8 and Figure 9.

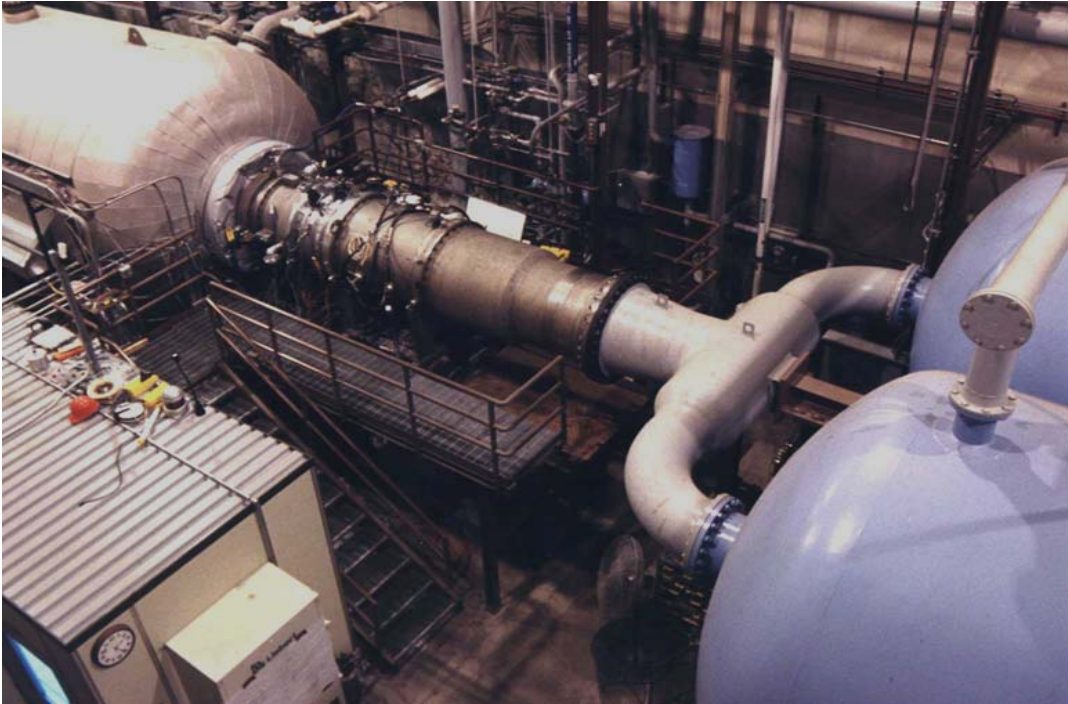


Figure 8: TRF experimental apparatus

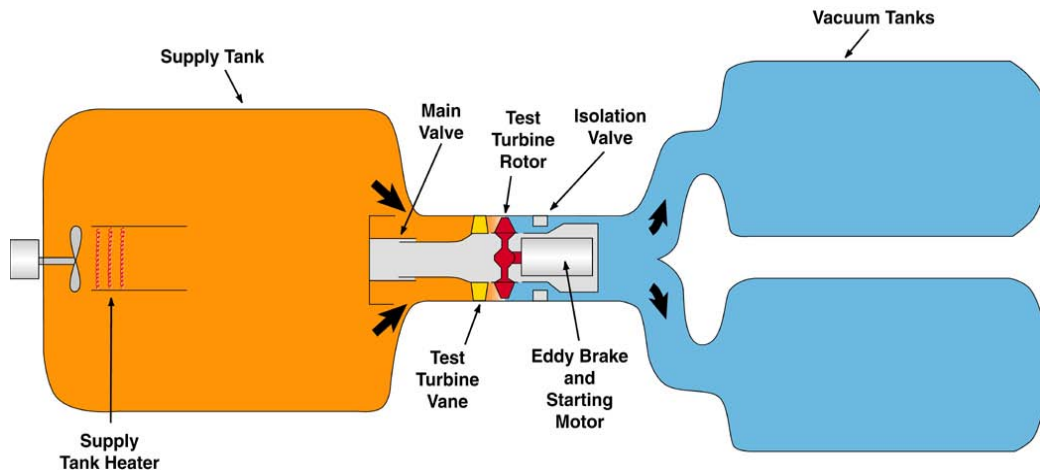


Figure 9: Schematic of TRF

Testing is conducted in a series of steps. First, the supply tank is filled with nitrogen, pressurized, and heated until matching the required aerothermodynamic parameters for simulating the inlet of the turbine vane stage. Uniformity is maintained by the fanned heater, and assured by spatial instrumentation within the supply tank. The tank has a volume of 91 cubic meters and can be pressurized up to 1034 kPa at a maximum temperature of 533° K. Tank surface temperatures are monitored by embedded thermocouples, and gas temperature probes monitor tank uniformity. A typical metal temperature variation throughout the tank is approximately 9.8° K, with gas variations closer to 2 ° K. These measurements of temperature and volume, coupled with a measurement of the pressure decay with time, are also used in calculating the massflow of the freestream gas through the test section. The main valve (directly aft of the supply tanks) holds this aerothermodynamically-matched nitrogen until testing. Meanwhile, the vacuum (dump) tanks, with a total 180 cubic meters of volume, are evacuated to form a vacuum of less than 0.689 kPa. This serves as the sink for the blowdown, while also ensuring that the isolation valve, aft of the test section, provides for a choke point in the freestream flow, setting the pressure ratio across the test section and maintaining a

choked condition through the test. This also forms a choke point at the vane throats in the test section, through which Mach numbers are nominally 1.0. Upon opening of the main valve, the nitrogen moves rapidly toward the vacuum tanks. Closing of the main valve (followed by closing of the isolation valve) ends flow of the nitrogen through the test section, effectively ending the blowdown.

The previously-described details allow for matching of the freestream fluid through the test section. Both an inlet profile generator (combustor simulator) and intricate coolant delivery system are required to further match the conditions a turbine section will experience. A view of the simulator is seen in Figure 10 .

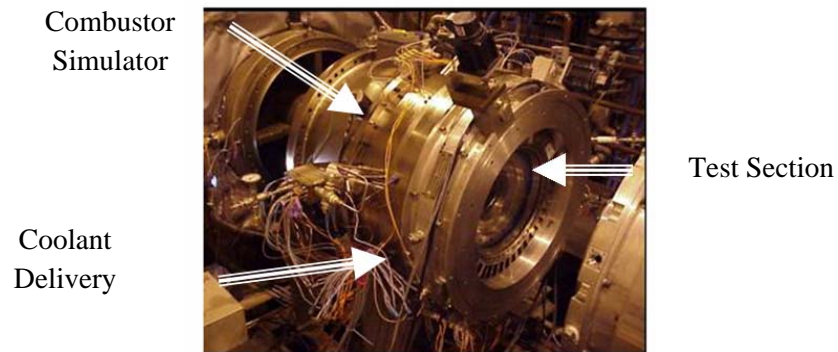


Figure 10: View of TRF combustor simulator, coolant delivery, and test section

3.1.2.1 Combustor Simulator

Aft of the main valve is the combustor simulator, an inlet profile generator intended to replicate the complex flow fields downstream of the combustor section in real engines (Barringer, et al., 2007: 1). The flows experienced during testing were circumferentially-uniform. The goal, however, was to create radially-variable profiles typical of a combustor. Seen in Figure 11 are the inlet profiles of C_p , coefficient of pressure, and Θ (a nondimensional temperature parameter), to the test section, defined as:

$$C_P = \frac{P - P_{AVE}}{\frac{1}{2} \rho_{ave} v_{ave}^2} \quad (2)$$

and

$$\theta = \frac{T - T_{ave}}{T_{ave}} \quad (3)$$

providing a ratio of the local temperatures and pressures over the span of the inlet (Z/S).

The inlet profiles maintained for current testing resemble Inlet Profile B. These inlet profiles were coupled with other CFD calculations, as shown in the Appendix, to gain local Mach number and driving temperature calculations at the vane and BOAS gauges. In order to properly calculate the inlet conditions to the BOAS, the losses through the vane section (and delivered at the rotor inlet) were determined.

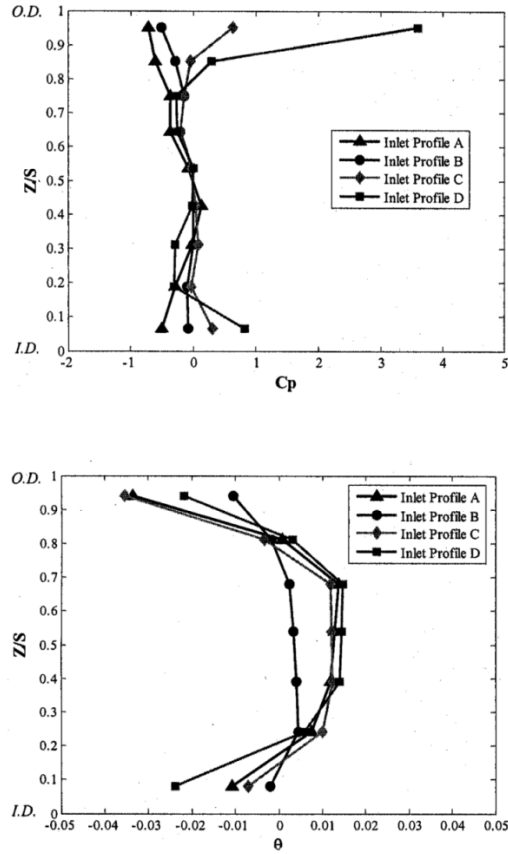


Figure 11: Inlet Temperature and Pressure Profiles (from Barringer, et al., 2007)

Total pressure losses (ξ) are seen in Figure 12 , and temperature profiles (Θ) in Figure 13.

Total pressure and temperature loss near the outer diameters (from which local temperatures and pressures at the BOAS could be determined) was 3.90 %.

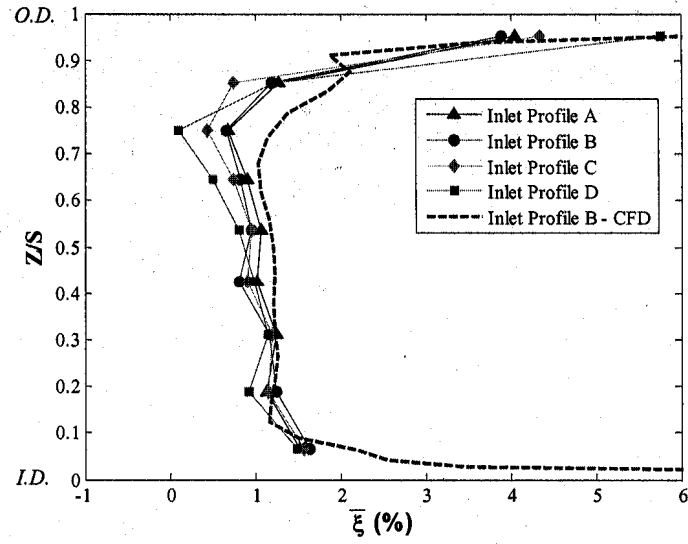


Figure 12: Total pressure losses at vane exit

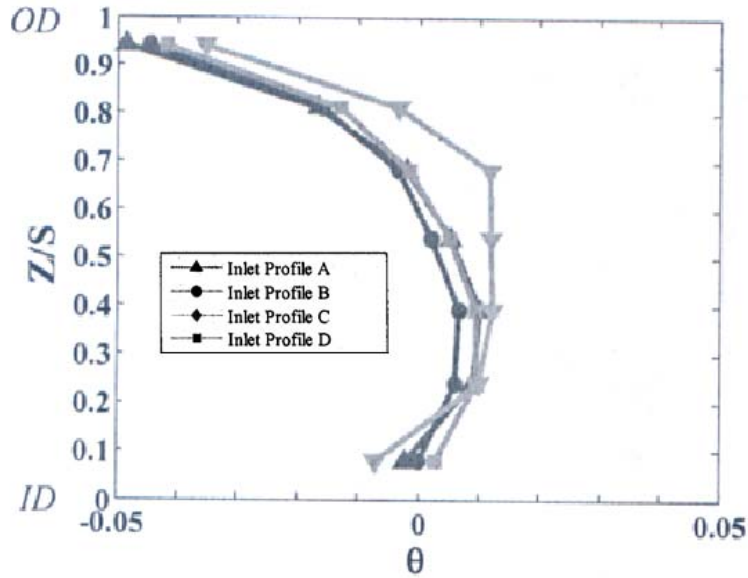


Figure 13: Temperature profiles at vane exit

3.1.2.2 Cooling System

The test section for this investigation is a single-stage, high-pressure turbine. This hardware is fully cooled and obtains its coolant flow from two separate delivery lines. A schematic of the coolant system is seen in Figure 14. Outer diameter flow supplies the film-ejection holes of the trailing edges of the vane (as seen in Figure 15) with coolant as well as the ejection ports in slotted areas of the BOAS. Inner diameter flow supplies the film-ejection holes of the leading edges of the vane and the rotor blades. For the purposes of data reduction, individual locations along the airfoil must be paired with the coolant supply that is ejected and flows over that surface location. Along the pressure side of the airfoils, the split between ID and OD feed occurs at approximately 50 % surface length (x/S), and at approximately 42 % surface length for the suction side.

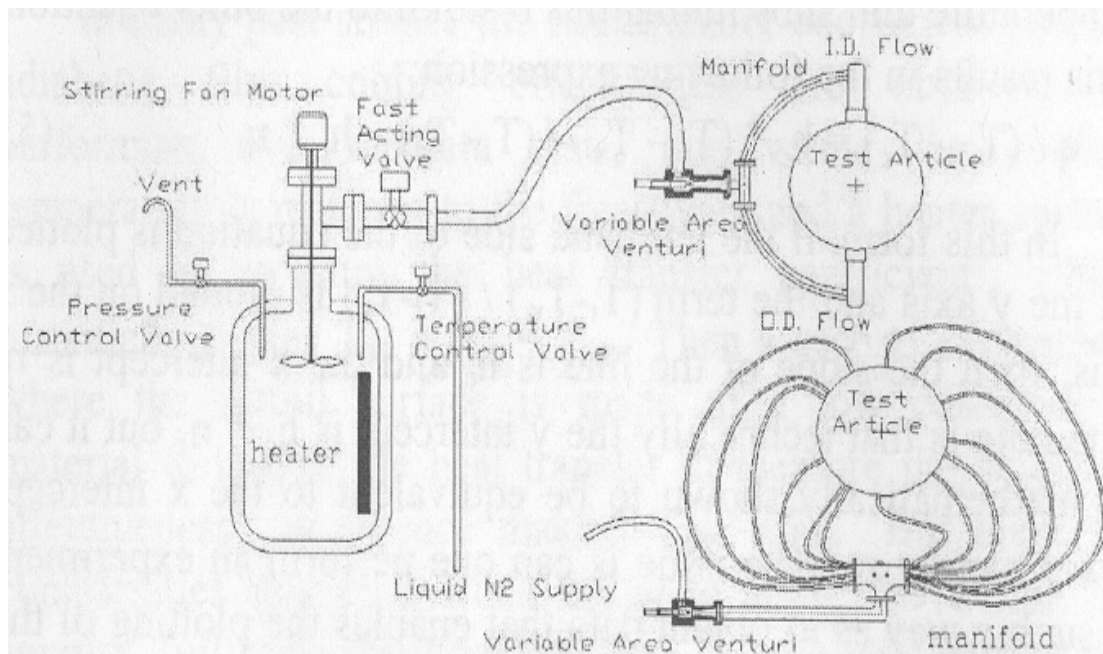


Figure 14: Coolant delivery system

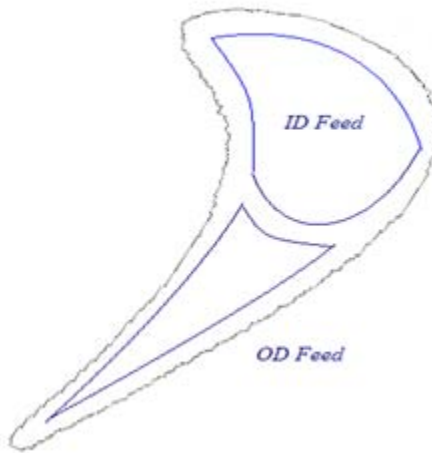


Figure 15: Coolant delivery to vanes

3.1.2.3 Vane and Rotor Test Section

The tested apparatus was a full-scale vane and rotor ring of proprietary design consisting of 44 vanes and 58 blades. While the airfoils were geometrically the same, the cooling schemes varied among two designs in the vanes and four designs in the rotor blades. Examples of these coolant schemes are seen in Figure 16 with shaped holes on the left and angled slots on the right. Tip cooling was incorporated into each blade of four differing designs, but all with the coolant ejected only through the first 31 % of the axial chord along the tip of the airfoil. Tip schemes are seen in Figure 17. Squealer tips consisted of depressions (seen in grey in the figure) of approximately 2.0 % of the radial span of the airfoil. Tip clearance among the blades varied from approximately 0.305 % to 0.675 % of the span of the rotor blades. A full layout of the blade types and average static tip clearances is seen in Table 2. The rotor shroud (BOAS) was divided circumferentially into 38 equal segments, between each of which was a cooled slot. The leading edge of the rotor blades was approximately 60 % of the axial chord of the blades from the trailing edge of the vanes. Several tests conducted previously at TRF spoke of

findings that were gathered from experiments on this vane and rotor stage's geometries and coolant schemes; however, the data presented hereafter is the first set of data from this setup to be fully-cooled, with both a vane and rotor stage.

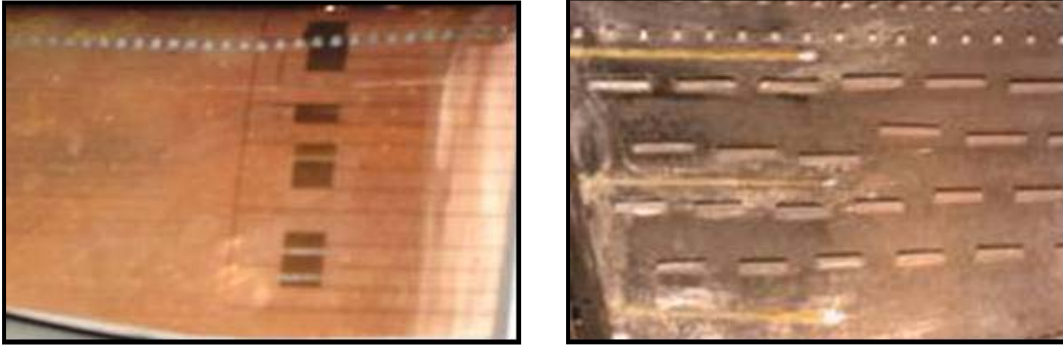


Figure 16: Vane coolant schemes

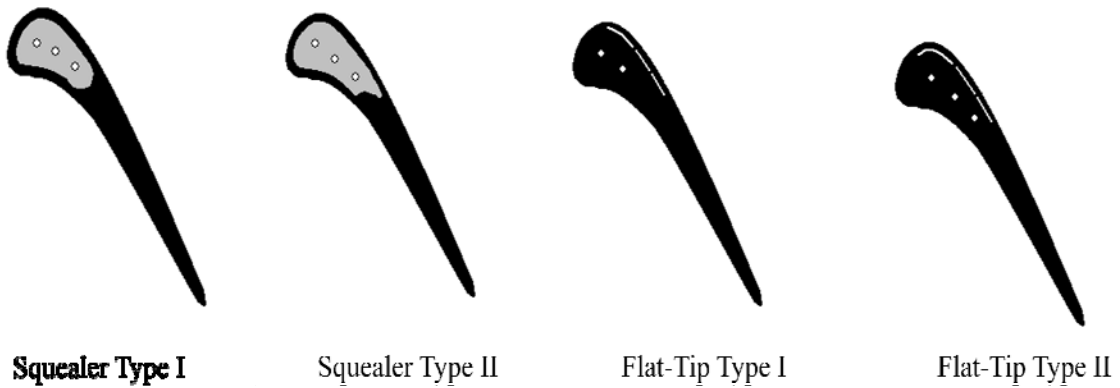


Figure 17: Tip coolant schemes

Table 2: Tip clearances and schemes

Blade	Tip Clearance (1/100 mm)	Tip Type
1	25	Squealer Type I
2	22.25	Squealer Type I
3	22.5	Squealer Type I
4	30.5	Squealer Type I
5	20.5	Squealer Type I
6	37.75	Squealer Type I
7	35.5	Squealer Type I
8	20.5	Squealer Type I
9	40.5	Squealer Type I
10	46.5	Flat Tip Type I
11	47	Flat Tip Type I
12	48	Flat Tip Type I
13	47.75	Flat Tip Type I
14	47.75	Flat Tip Type I
15	46.5	Flat Tip Type I
16	21.75	Squealer Type I
17	36.5	Squealer Type I
18	22	Squealer Type I
19	38.25	Squealer Type I
20	36.5	Squealer Type I
21	23.25	Squealer Type I
22	23.25	Squealer Type I
23	36	Squealer Type I
24	37.25	Squealer Type I
25	42.25	Squealer Type I
26	23	Squealer Type I
27	22.5	Squealer Type I
28	25	Squealer Type I
29	41.5	Squealer Type I
30	27.75	Squealer Type I
31	25.25	Squealer Type I
32	41.25	Squealer Type I
33	24.5	Squealer Type I
34	41.75	Squealer Type I
35	40	Squealer Type I
36	22.75	Squealer Type I
37	41.25	Squealer Type I
38	23.25	Squealer Type I
39	37.75	Squealer Type I
40	23.75	Squealer Type I
41	24.5	Squealer Type I
42	27.25	Squealer Type II
43	27	Squealer Type II
44	26.75	Squealer Type II
45	26	Squealer Type II
46	26.25	Squealer Type II
47	49.25	Flat Tip Type II
48	49	Flat Tip Type II
49	23	Squealer Type I
50	23.75	Squealer Type I
51	40.5	Squealer Type I
52	40.25	Squealer Type I
53	23	Squealer Type I
54	40.5	Squealer Type I
55	23.25	Squealer Type I
56	39.75	Squealer Type I
57	23.75	Squealer Type I
58	23.75	Squealer Type I

3.2 Experimental Procedure

In running a test, the rotor is spun by an air motor to a speed above the desired testing speed. The air motor is then disengaged and the test sequence starts automatically once the rotor slows down to the desired test speed. This includes the beginning of the data acquisition process followed by the flow of coolant to the inner and outer diameters of the test section. This premature flow of the coolant allows the flow to establish in relatively long supply lines, and also allows the coolant to achieve a lower value prior to testing. The main valve is then opened, which initiates the blowdown of flow from the main tank. This valve fully opens in approximately 100 milliseconds. The flow moves through the test section and back through to the dump tanks. It should be noted that, after this valve opening, a shock wave moves through the test section, and the development of the boundary layer in the test section occurs (both of which occur in finite periods of time). In transonic facilities such as TRF, full boundary layer development on the trailing edges of similar airfoils amounted to 30-35 ms (Johnson, et al., 2007: 7). After this, an essentially ‘steady-state’ condition of flow along the airfoils is reached and maintained until closing of the isolation valve. Coolant flow establishment takes additional time, to be discussed further shortly.

As stated before, matching of the corrected speed (plotted in units of RPM/°K) of a turbine section allows for experimentation which can truly represent the complex flow fields of the tip/shroud region. Because the fluid’s properties (γ and R) are known, the facility’s control software simplifies the equation for corrected speed to:

$$\text{RPM} / \sqrt{T}$$

(4)

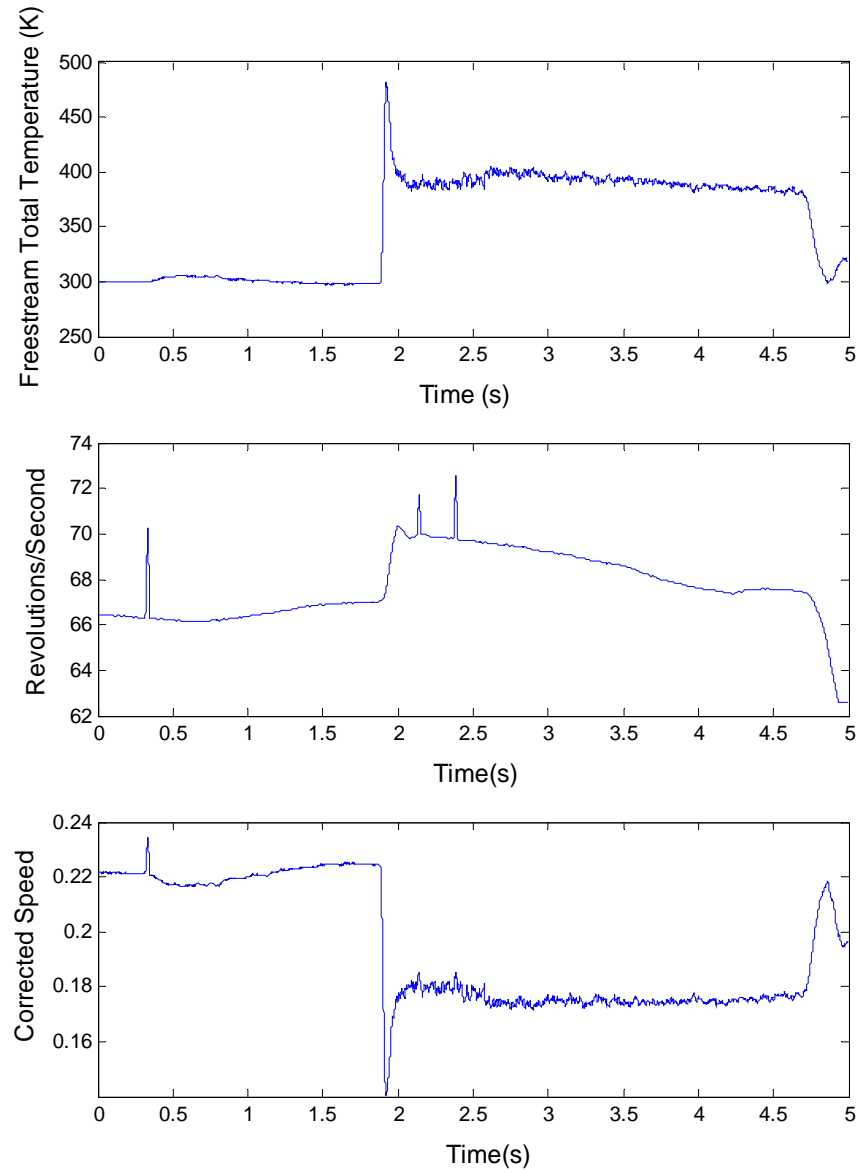


Figure 18: Corrected speed maintenance

To continue matching the corrected speed in a run, a complex sequencing is engaged for testing. Measurements of speed and inlet temperature are taken real time during the test. The calculated values from corrected speed are fed in (from inputs of mainstream temperature and engine RPM) into one side of a comparative op-amp in a comparison circuit. The calculation given in Equation (4) is performed and measured against the desired values input in the control module. The difference is then fed into the control circuit for the eddy brake, which controls a current which serves as a resisting force against the rotation of the motor, allowing for accurate matching. A view of the corrected freestream total temperature and rotor speed decay (from which corrected speed is measured in real-time), as well as the maintained corrected speed, is seen in Figure 18 for a sample run.

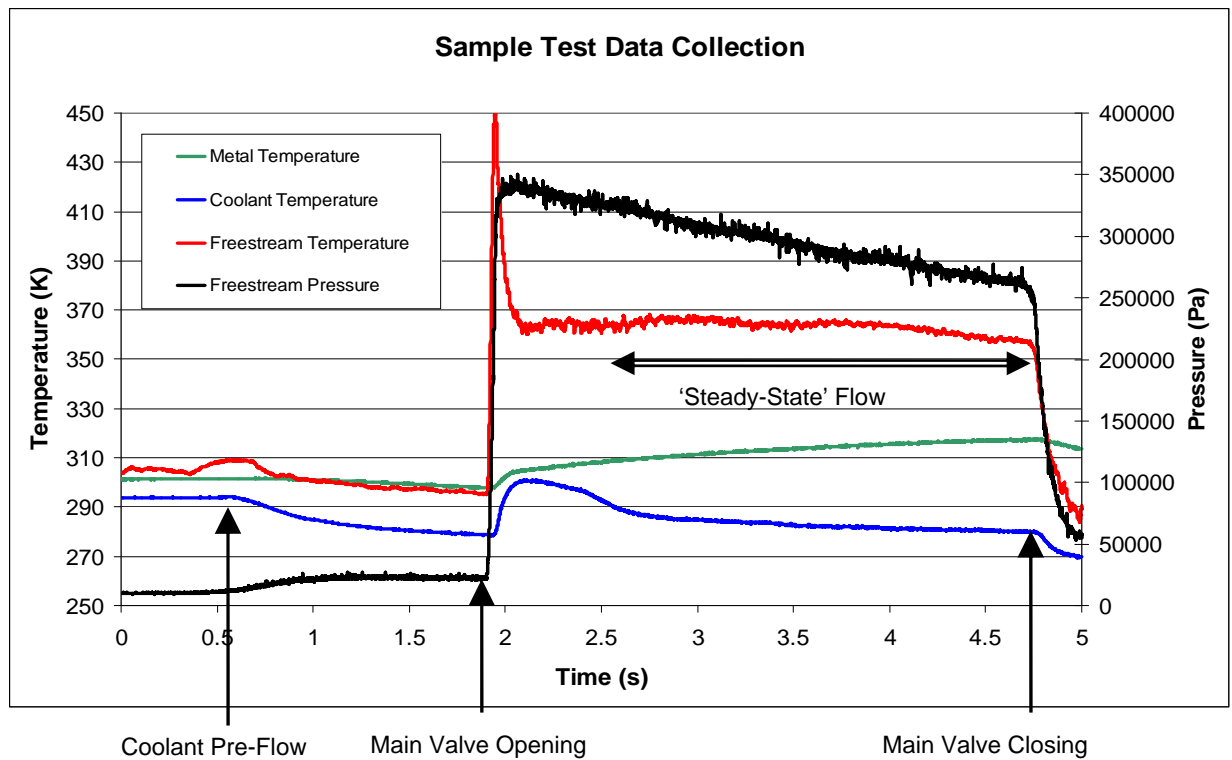


Figure 19: Sample test data collection

A sample of the data taken during a test, annotated as it pertains to the sequence of an experiment, is seen in Figure 19. The sample metal temperature trace is taken from the data trace of a vane-mounted thermocouple. Main valve opening can be seen at approximately 1.87 seconds and isolation valve closing at approximately 4.75 seconds. Further discussion regarding the section of ‘steady-state flow’ as it pertains to data results and analysis will follow.

3.2 Instrumentation

Instrumentation most vital to the current study included those which delivered total and static temperatures and pressures and heat flux data throughout the test. While sampling frequencies varied, nominal data collection speed was 50 kHz. At operating speed, one of 58 blades in the test section will pass any circumferential position over 6500 times per second. Because of the high frequency of these events, the TRF instrumentation’s high sampling frequency is of vital importance. The signal from each data channel individually experiences a low-pass filter (ensuring the frequencies acquired are only up to the Nyquist frequency) and a built-in amplifier to improve the signal-to-noise ratio.

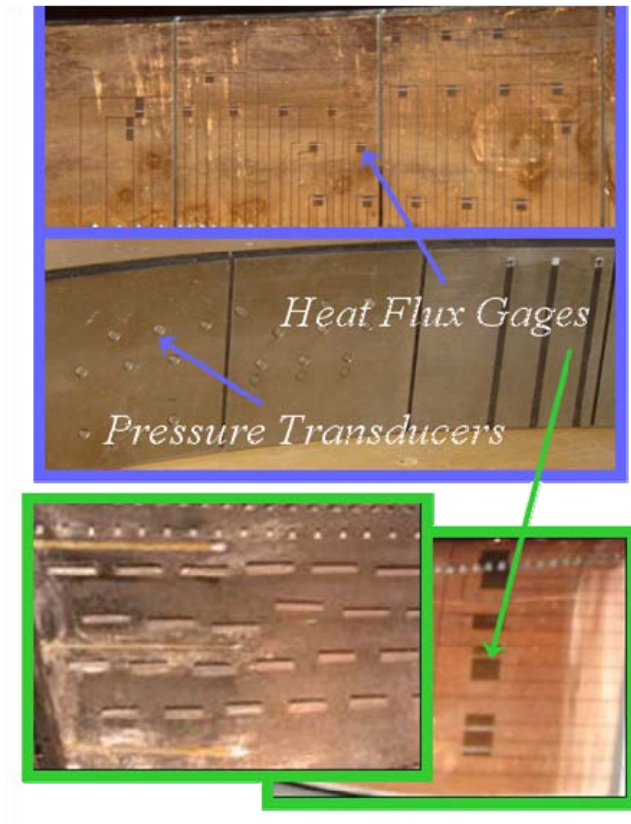


Figure 20: Instrumentation on shroud and vanes

Instrumentation along the shroud (outlined at the top) and vanes (outlined below these) are pictured in Figure 20. Most involved and least familiar in operation is the instrumentation for collection of heat flux data. These consist of a platinum thin-film gauge, sputtered onto a Kapton substrate under which lie surface-embedded thermocouples (3-mil, E-Type). Conductive heat flux is determined by comparison temperature measurements on both sides of this Kapton insulating layer, instrumented upon the surfaces of interest. Conductive heat transfer through this is equivalent to the convective heat flux imposed upon the surface. Exact details of this data reduction, a method originating from the University of Oxford, are described in more detail shortly.

Heat Flux Gauges are mounted along lengths of both the suction sides (SS) and pressure sides (PS) of the vanes at approximately 24-, 60-, and 90-percent of the vane's span (percent y/b , measured from the inner diameter of the airfoil, as seen in Figure 21)

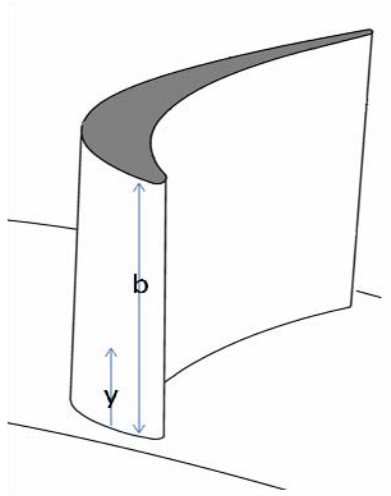


Figure 21: Percent span depiction

The functional thermocouples on the vane (named by their data trace's header in the TRF data acquisition system, such as *QVXI* or *PVPI*) are seen at their nominal mounting locations in Figure 22 (for those at 60 % span) and Figure 23 (for those at 24 % span). Mounting location is designated as the ratio of the surface distance of the gauge from the stagnation point of the airfoil to the total surface distance of the individual side. Kulite fast-response pressure transducers as well, are surface-mounted along both the suction sides and pressure sides of the vanes, but at approximately 60-, 91-, and 97-percent span. Locations of the pressure transducers located along the vane surface at nominally 60 % span are seen in Figure 24. Header names correspond as follows: embedded thermocouples are designated as *TVs*, Kulites as *PVs*, and thin-film temperature gauges as *QVs*.

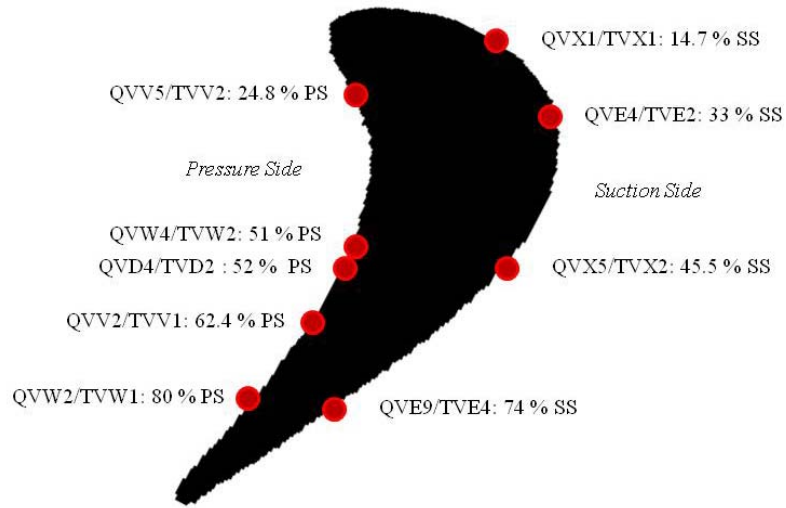


Figure 22: Vane heat flux gauge mounting at 60 % span

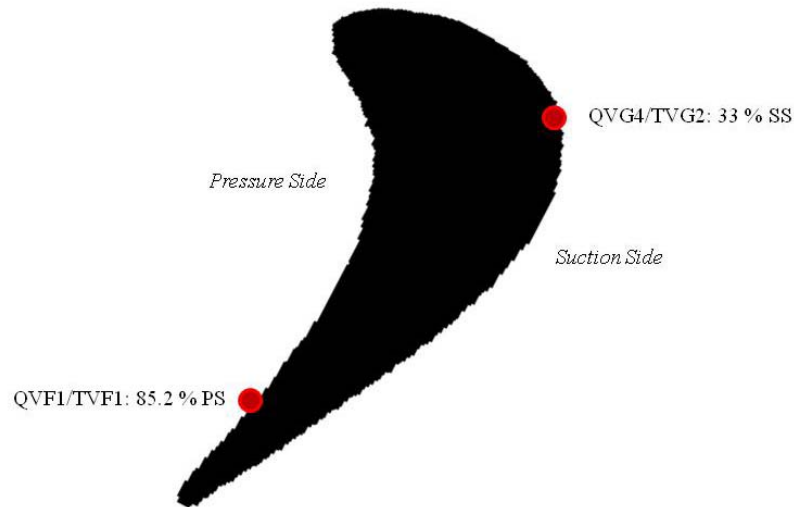


Figure 23: Vane heat flux gauge mounting at 24 % span

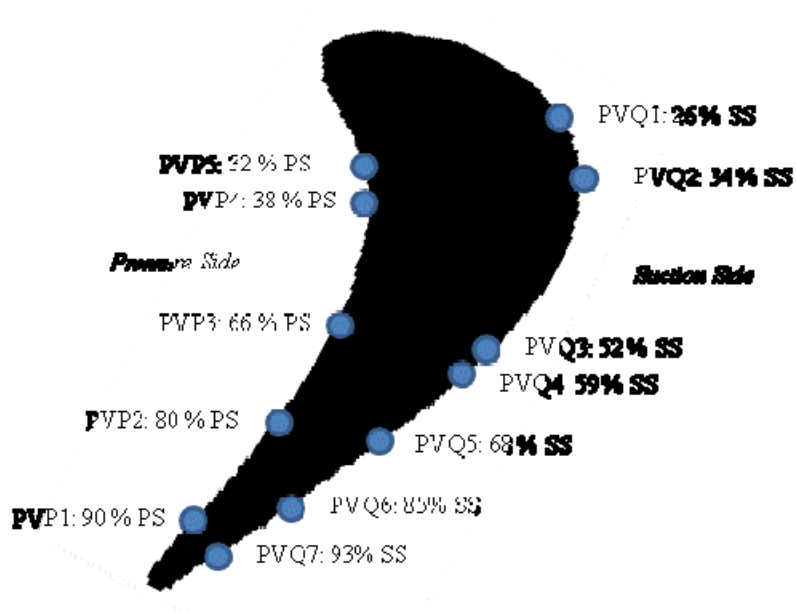


Figure 24: 60 % Span pressure transducers

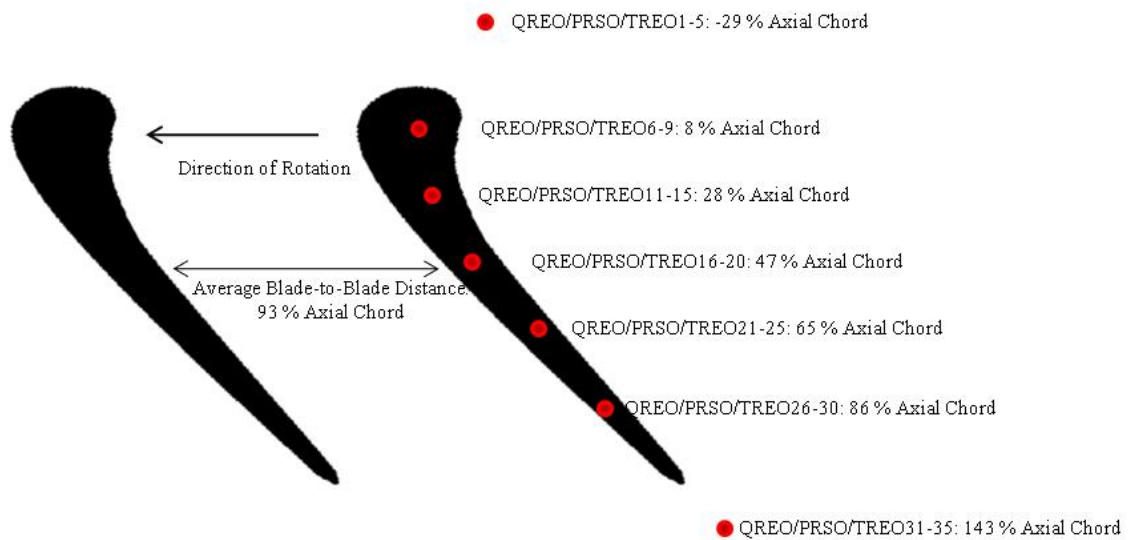


Figure 25: BOAS-mounted gauges

These heat flux gauges and pressure transducers are mounted fore to aft on the blade outer air seal (BOAS) along the predicted streamlines of four vane wakes as the wake passage is turned by passing rotor blades, located by percent axial chord of the blade itself (x/C). Though not all data traces were usable, all gauges are represented in Figure 25. The functional heat flux gauges and underlying thermocouples lay at 47 and 86 % axial chord.

Pressures and temperatures upstream and downstream of the test section were measured using nine-headed traversing rakes with instruments at locations along the span of the rig. These were located approximately one axial chord (of the vane) upstream and downstream of the test section. During the course of a test, these instrumented rakes traverse 120 circumferential degrees to gain temperature and pressure data representative of the flow through this radial section.

In order to accurately reduce and calculate several parameters, most specifically h , ϕ , and η , along the surfaces of the blades, local Mach numbers and effective driving temperatures along the surfaces of the vane and along the BOAS were determined. This was performed using isentropic relations coupled with CFD predictions and sample pressure and temperature values at each finite location, described in detail in the Appendix.

3.3 Heat Flux Gauges

The technique of heat flux measurements employed in this experiment rely upon temperature measurements on both sides of an insulating film layer instrumented upon the surfaces of interest. A representation of the configuration used in the current

experiment is seen in Figure 26. Two notes of importance arise in the use of this system: In order to derive usable, time-variant heat flux data, a discrete deconvolution is used for each given sampling rate (Oldfield, 1986). The reduction of this heat flux data was performed using the *Matlab* coding from Dr. Martin Oldfield of Oxford University. It has been used successfully at TRF previously (Umholtz, 2007: 52).

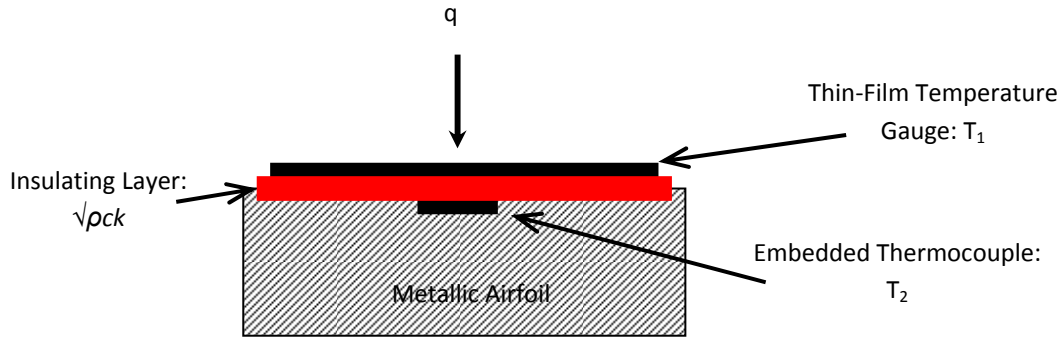


Figure 26: Heat flux gauge design

Heat flux measurements are obtained through considering the heat transfer into the gauge as a superposition of both a differential heat transfer and a common mode heat transfer. For differential heat transfer, q_d , a driving temperature difference $(T_1 - T_2)/2$ is applied at the top surface and $-(T_1 - T_2)/2$ is applied to the bottom, resulting in zero net temperature change in the insulating layer. In the common mode heat transfer, q_c , a driving temperature difference of $(T_1 + T_2)/2$ is applied at the top and bottom surfaces, resulting in no net heat transfer through the middle. These temperature differences are solved at a given total heat transfer, q_s , represented as a unit step function, by deconvoluting the sampled step heat flux and temperature pairs using a *Matlab* filter. Heat transfer coefficients for both the differential (h_d) and common mode (h_c) heat fluxes are obtained and recombined for both the top surface ($h_1 = (h_c + h_d)/2$) and the bottom ($h_s = (h_c + h_d)/2$) to form a unique solution for resultant heat flux through

Matlab's filtering of the resulting heat transfer coefficients with their respective temperature measurements:

$$q = \text{fftfilt}(h_1, T_1) + \text{fftfilt}(h_2, T_2) \quad (5)$$

(Doorly and Oldfield, 1986: 1159-67).

Of special note in transient and unsteady heat transfer is the accuracy of this method, which is highly-dependent upon the accuracy of material properties used in finding the thermal product of the insulating thin layer ($\sqrt{\rho ck}$), the square root of the product of density, specific heat capacity, and thermal conductivity (Umholtz, 2007: 21). In a series of Monte Carlo simulations performed with variations in the impulse functions used to find heat transfer, even very small variations in this thermal product (~ two percent) were seen to produce very large variations in the delivered heat flux, proving this to be the controlling parameter. Values of this thermal constant were given by the manufacturers. The thin-film temperature gauge mounted on the outer surface gains a temperature reading through simple reduction of measured output voltage from a Wheatstone bridge where the gauge resistor is supplied a constant current; this measurement became an object of interest in a tangential investigation surrounding the uncertainty induced. Uncertainty in the measurement of T_1 totaled approximately 0.8° K. The effect of this uncertainty on the resulting heat flux calculation was investigated; this deviation resulted in an uncertainty in heat flux calculation of only 6.7 (W/sq.m), or 0.02 % , deemed negligible.

It was also seen that the accuracy of this reduction was dependent upon exact superposition of the thin-film gauge on top of the underlying thermocouples. Because

several data channels failed during experimentation, ideal matching of thermocouples with thin-film gauges was not possible. It was hoped that the underlying thermocouples (of which there were a lesser amount) could be coupled with the numerous thin-film gauges surrounding that embedded locality to gain a trace of heat flux. To either disprove or confirm this hope, two gauges, mounted along the vane at 60 % span, 80 % surface length (pressure side) and along the BOAS at 47 % axial chord of the blade tip, were coupled with the thermocouple directly underlying, as well as with embedded thermocouples in the vicinity. From 2.5 to 4.5 seconds, the heat flux varied considerably with these errors in calculation: On the vane, error in calculated heat flux averaged 14 % with a thermocouple matched by 30 % chord away. On the BOAS, an underlying thermocouple matched with a 39 % departure in axial chord saw an average error of 50.8 %, and 10.7 % when off by radial location. It was therefore determined that heat flux could be accurately calculated from only locally-matched thin film gauges and embedded thermocouples. This resulted in considerably less data traces available for heat flux determination than instrumented originally.

A sample trace of the thin-film and underlying thermocouple data during a test (for a vane gauge--also generally representative of the traces for a shroud gauge) is seen in Figure 27. From this data, heat flux was calculated. As a side-note: as annotated, a high level of heat transfer is initially seen in the test article (due to the high freestream temperature moving through with the shock), shortly following initiation of the blowdown. As freestream temperature drops and metal temperature rises, heat transfer decays in magnitude until reaching a relatively steady-state value. As will be discussed later, 1.2 seconds of this steady-state flow window (2.5 to 3.7 sec for this test) were

processed for reduction of time-resolved data (during which the rotor disc made between 80 and 140 full revolutions, dependent upon rotation speed) The latter portion of this (3.5-3.7 seconds) was then found to be within the period of most steady-state heat transfer. In previous studies, a low-pass filter was used in order to eliminate high-frequency variations in the delivery of the temperatures and the calculated heat flux (Umholtz, 2007: 22). This was not used for the time-resolved data, however, because of the nature of the unsteady effects in a vane-rotor stage. It is preferred to analyze the high-frequency phenomenon.

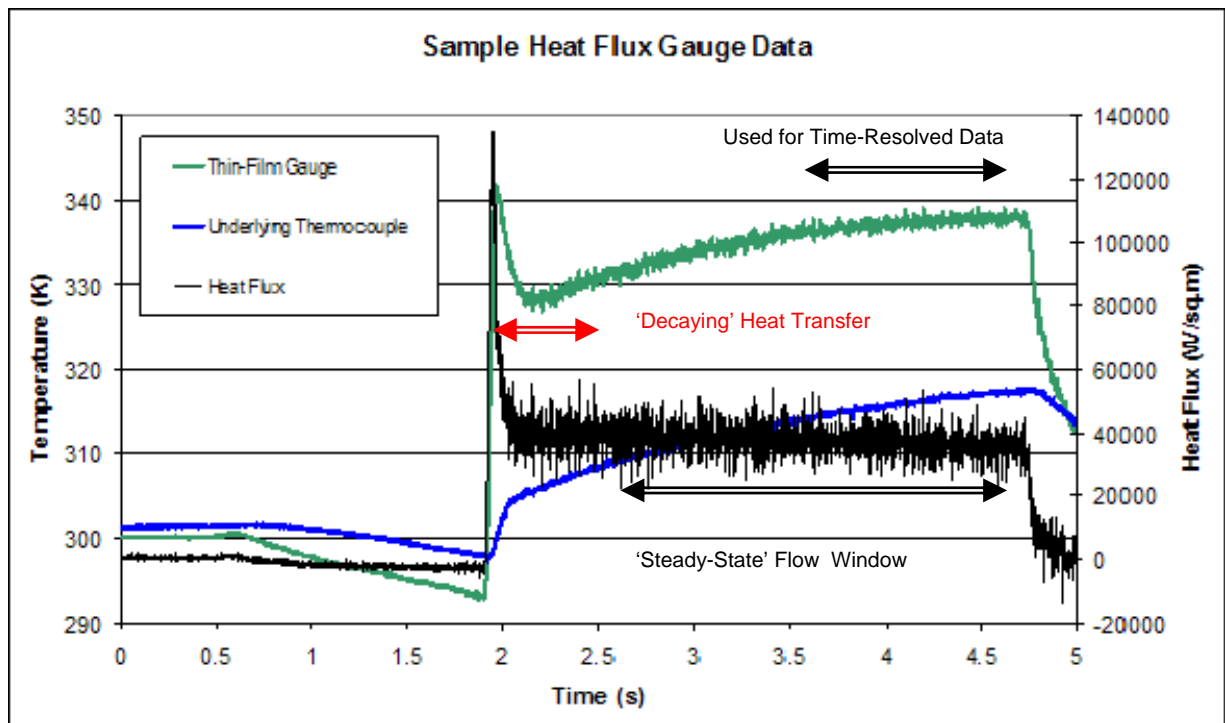


Figure 27: Sample heat flux gauge data

3.4 Test Matrcies

Because film-cooling is highly dependent upon the operating conditions, conditions were varied throughout the experimental trials. The most relevant operating

parameters are seen in Table 3. The values are averaged over the period determined to be most representative of steady heat transfer: 3.5 to 4.5 seconds. The determination of inlet Reynolds numbers is described in the Appendix. The notation (C/F) represents the ratio of the coolant to freestream. It should again be noted that the OD coolant feeds the TE gauges and rotor shroud slotted junctions and the ID coolant feeds the vane LE gauges and rotor blades. Each heat flux gauge is paired with the appropriate coolant flow for data reduction. Temperature and pressure ratios of the coolant to the fluid were taken as average temperature and pressure at the supply over the upstream static temperatures and pressures. Higher pressure ratios correspond to higher coolant massflow ratios. Runs 1-5 were used for results validation, and reduction of data for investigations into unsteadiness. For further data reduction, the same process for finding parameters was used in a set of data only for time-averaged reductions, as seen below in Table 4.

Table 3: Time-resolved run parameters

		<u>1</u>	<u>2</u>	<u>3</u>	<u>4</u>	<u>5</u>
Rotor Speed	(RPM)	4108.2	4096.8	6600	6624	7044
Testing Corrected Speed	(Unitless)	187	187	320	320	332
Freestream Massflow	(kg/s)	10.53	10.02	20.18	19.71	22.02
Freestream Temperature	(K)	389.3	371.4	361.1	367.5	379.6
ID Coolant Massflow	(kg/s)	0.479	0.6547	1.339	0.6316	1.141
ID Coolant Temperature	(K)	281.1	283.3	275.2	275.9	250.3
OD Coolant Massflow	(kg/s)	0.363	0.5874	0.721	0.3967	0.3211
OD Coolant Temperature	(K)	279.2	250	270	291.7	276
Avg. Massflow Ratio (C/F)	(Unitless)	0.03998	0.06198	0.05104	0.02609	0.0332
Avg. Temperature Ratio (C/F)	(Unitless)	0.71962	0.71796	0.75492	0.77224	0.69323
Inlet Reynolds Number (BOAS)	(Re), 10^5	5.627	5.453	4.573	4.663	6.087
Inlet Reynolds Number (Vane)	(Re), 10^6	1.017	0.993	1.636	1.632	1.882

Table 4: Time-averaged run parameters

	<i>Gas-to-Metal Temperature Ratio (T_g/T_m)</i>	<i>OD Coolant Temperature Ratio (C/F)</i>	<i>ID Coolant Temperature Ratio (C/F)</i>	<i>OD Coolant Pressure Ratio (C/F)</i>	<i>ID Coolant Pressure Ratio (C/F)</i>	<i>Test Rotor Speed (RPM)</i>
<u>A</u>	1.260	0.634	0.633	1.22	1.22	2800
<u>B</u>	1.287	0.645	0.604	1.18	1.15	2500
<u>C</u>	1.235	0.701	0.714	2.74	2.77	2600
<u>D</u>	1.283	0.683	0.647	2.73	2.66	1000
<u>E</u>	1.207	0.758	0.723	2.76	2.69	1000
<u>F</u>	1.192	0.791	0.716	2.77	2.63	2600
<u>G</u>	1.237	0.644	0.641	1.25	1.24	6875
<u>H</u>	1.098	0.787	0.771	1.33	1.32	6469
<u>I</u>	1.134	0.739	0.699	1.29	1.25	6469
<u>J</u>	1.241	0.695	0.615	1.06	1.00	7444

4. Methodology

4.1 Derivation of Film-cooling Parameters

The primary device of local heat transfer in a turbine is convection, represented as:

$$q'' = h \Delta T \quad (6)$$

Where the heat flux (q'') into a surface (in this case, the metallic components of a engine's turbine section) is a function of a heat flux coefficient (h) and a temperature gradient (ΔT). For the case of heat transfer in a turbine section, this driving temperature gradient is defined as:

$$\Delta T = T_f - T_w \quad (7)$$

Where T_f represents the temperature of the film of fluid directly above the metal surface and T_w represents the temperature of the wall, or surface, itself. However, for cooled turbine components, the fluid temperature is highly variant across the airfoil, and is a combination of both coolant and freestream flow. Because of this, finding the true driving temperature for convective heat transfer is difficult.

For this condition, when uncooled, the driving temperature for convective heat transfer becomes the freestream temperature (T_∞), as represented by:

$$q_{uncooled}'' = h (T_\infty - T_w) \quad (8)$$

In a metallic airfoil, heat flux into the surface ($q_{convective}$) is equivalent to that through the surface ($q_{conductive}$), and the conductive heat transfer is driven by the convective heat transfer at the airfoil surface. This allows one to gain useful and highly-representative

results from many experiments conducted with a nearly non-conductive material for the airfoils. Many typical film-cooling experiments are conducted with a nearly non-conductive material for the airfoil. This forces zero conductive heat transfer ($q_{conductive} = 0$), and an adiabatic surface temperature is achieved at the wall. Therefore, the convective, adiabatic heat transfer becomes:

$$q_{f,adaibatic}'' = h_f(T_{aw} - T_w) \quad (9)$$

where the temperature gradient (ΔT) becomes the difference between the surface itself and the temperature just above the surface (T_{aw}), described as the adiabatic wall temperature in these experiments. This is vital for determining the adiabatic effectiveness:

$$\eta = \frac{T_{\infty} - T_{aw}}{T_{\infty} - T_{c,exit}} \quad (10)$$

where $T_{c,exit}$ represents the temperature of the coolant at the exit of the ejection holes.

This value (η) thus represents the effectiveness with which the coolant flow lowers the temperature of the hot freestream gases at the airfoil surface. For a film-cooled experiment this is the driving temperature that would be achieved for heat transfer.

Therefore, film-cooled heat transfer in adiabatic conditions is simply:

$$q_f'' = h_f(T_{aw} - T_w)$$

The local film-cooled heat transfer coefficient thus becomes h_f . It should be noted that this adiabatic wall temperature and local heat transfer coefficient can vary over the airfoil surface. A representation of some of these values using a generic airfoil coolant ejection hole is seen in Figure 28. Two sample temperature profiles are shown in this figure: on the right, the profile is representative of what actually may occur; on the left the situation

used to perform experiments on adiabatic effectiveness (with no heat flux onto a non-conducting surface) is seen. Both these cannot be achieved with the same test.

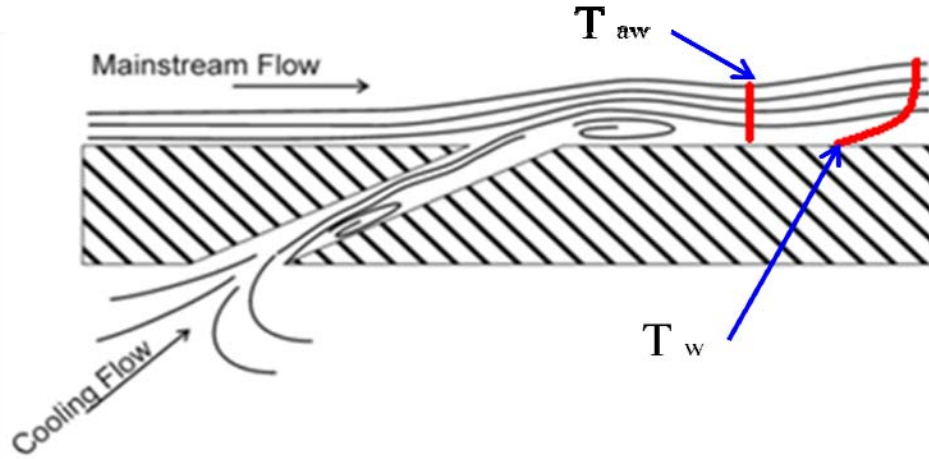


Figure 28: Film-cooled airfoil experimental values

These parameters, h_f (heat transfer coefficient with film cooling) and η (film cooling effectiveness), have become the traditional standard of the industry in deliverable parameters for any film-cooling scheme. Several techniques have been developed for finding these values, but they are most often experimentally determined through two tests, both of which usually rely upon one-dimensional, semi-infinite assumptions: One test using a constant, known heat flux as a surface boundary condition (to determine h_f) and thermal or mass transfer techniques over a non-conductive material (for η). True airfoils, it is realized, are non-adiabatic. Therefore, the assumption of using the adiabatic wall becomes limited in accuracy.

When compared to an experiment that is non-cooled, a net heat flux reduction (NHFR, Δq_r), as defined by:

$$\text{NHFR} = \Delta q_{\text{reduced}} = 1 - q_f'' / q_{\text{uncooled}}'' \quad (11)$$

(or, using the values of heat transfer coefficients h and h_f),

$$\Delta q_{\text{reduction}} = 1 - \frac{h_f(T_{\text{aw}} - T_w)}{h(T_{\infty} - T_w)} \quad (12)$$

This characterizes the net effect of the addition of coolant flow to the airfoils (comparing net heat flux on the airfoil without film cooling compared to that with film cooling).

Intuitively, a positive value of NHFR is desirable in turbine sections.

Another parameter, overall effectiveness, is used to characterize the cooling scheme for a non-adiabatic wall material:

$$\phi = \frac{T_{\infty} - T_w}{T_{\infty} - T_{c,i}} \quad (13)$$

Where $T_{c,i}$ represents the temperature of the coolant inside the feed plenum of the airfoils, and T_w is the actual metal temperature. This becomes a useful parameter because the metal temperature is actually a function of coolant flow both internally and on the outer surface of the airfoil. However, it also presents challenges when addressing specific occurrences along airfoil surfaces. When external heat transfer coefficients (h_f), internal heat transfer coefficients (h_f), and Biot numbers are matched, overall effectiveness in scaled testing (such as the current testing) are wholly representative of those seen in a real engine. This proves the parameter of overall effectiveness to be a greatly useful parameter from the results at TRF.

4.2 Popp Method of Determining Film-Cooling Parameters

In tests conducted in an annulus test section on a generic high pressure turbine vane (Popp et al., 2000: 5), heat transfer results from both cooled and uncooled airfoils

were compared. In this investigation, a highly useful technique was described which allows the non-adiabatic data collected at TRF to be transformed into the traditional metric of adiabatic film cooling effectiveness and heat transfer coefficient. Similar testing apparatus to TRF was used, with surface-mounted heat flux gauges mounted on a film-cooled airfoil in a blowdown facility.

This method relies upon the calculation of a temperature difference (T_d) between the freestream total temperature (T_t) and the local recovery temperature (T_r), shown as:

$$T_d = T_t - T_r \quad (14)$$

When an airfoil is uncooled, this difference can be related by a recovery factor (r) and the freestream velocity:

$$T_d = (1 - r) \frac{v^2}{2C_p} \quad (15)$$

where the recovery factor is a function of the dynamics of the boundary layer. Inlet Reynolds numbers of the test section are characteristic turbulent flow. For flow in this regime, this recovery factor is:

$$r = Pr^{1/3} \quad (16)$$

As shown previously, for cooled experiments, the heat flux is shown by:

$$q_f'' = h_f(T_{aw} - T_w) \quad (17)$$

However, in uncooled experiments the adiabatic wall temperature can be equated to the recovery temperature, constraining the heat flux to:

$$q = h(T_r - T_w) \quad (18)$$

The uncooled heat flux thus becomes

$$q = h(T_t - T_w) - h \cdot T_d \quad (19)$$

Necessitating that, as would be expected, zero heat transfer (q) occurs when the wall temperature equals the recovery temperature. This may be of use in finding the cooling parameters for the outer air seal, whose film temperature is not heavily coolant-driven.

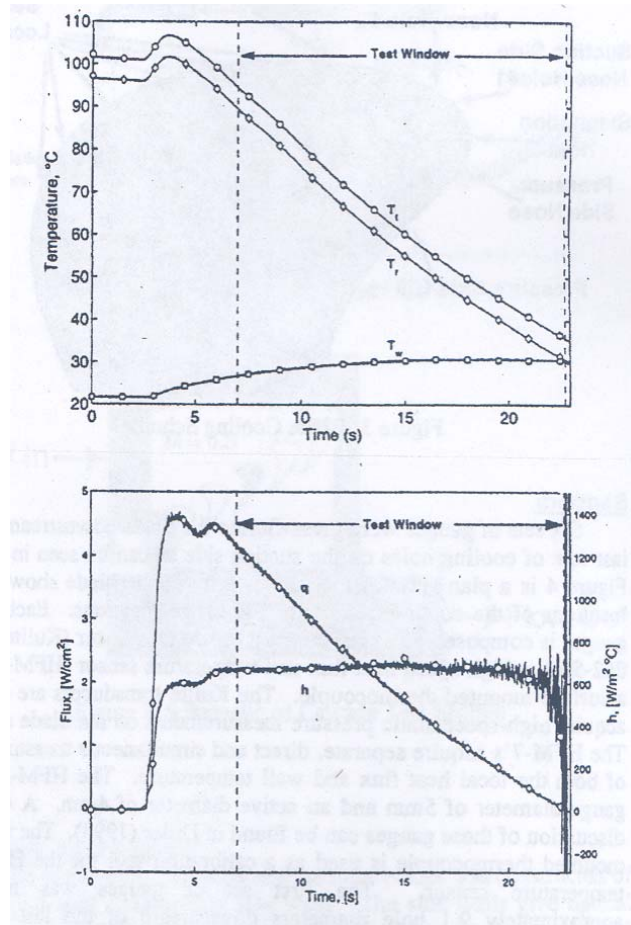


Figure 29: Temperature, heat flux histories in uncooled experiment (from Popp et al., 2000)

A sample of the data from an uncooled experiment from Popp's study is seen in Figure 29 and the plotting of the heat fluxes (q) and temperature difference ($T_t - T_w$) is seen in Figure 30. The recovery temperature's shape follows the decays of the freestream

temperature. When this data is applied in the slope-intercept form of (19), it becomes apparent that the slope represents the heat transfer coefficient.

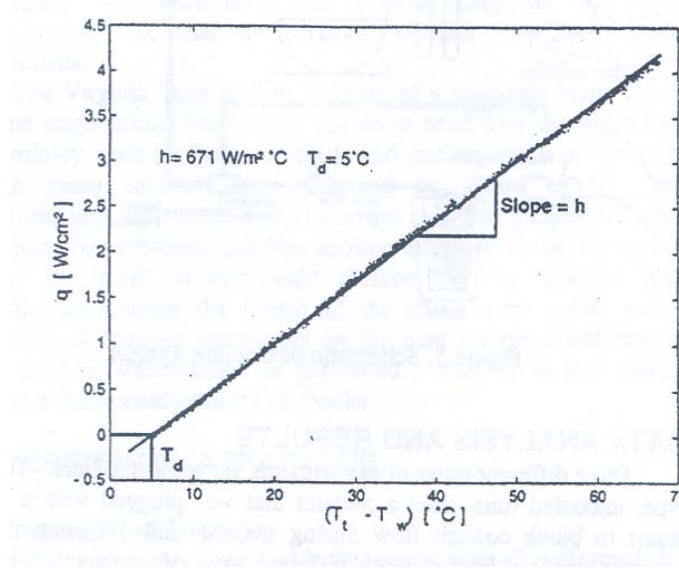


Figure 30: Regression of heat flux versus temperature difference (from Popp et al., 2000)

In cooled cases, however, the adiabatic wall temperature becomes a function of the mixing of both the freestream (and thus recovery) and the coolant temperatures. T_{aw} is used in the nondimensionalized adiabatic film-cooling effectiveness, in this case defined as:

$$\eta = \frac{T_{aw} - T_r}{T_c - T_r} \quad (20)$$

Solving this for T_{aw} and substituting into (17) yields an equation similar to the uncooled formulation of Equation (19):

$$\frac{q}{T_r - T_c} = \frac{h (T_r - T_w)}{T_r - T_c} - h \cdot \eta \quad (21)$$

The plotting of this slope-intercept form is seen in Figure 31, an example presented with this methodology. Adiabatic film-cooling effectiveness must be assumed to be constant, as this parameter is defined in an environment of steady flow and heat transfer. With this

presentation, it can be readily seen that adiabatic effectiveness is truly only a situation present with zero heat transfer. Again, the determination of the heat transfer coefficient (h) is taken from linear fitting of the slope of this line.

This technique has been employed recently in tests conducted at TRF on a fully-cooled metallic turbine vane ring (Polanka et al., 2008). To gain a curve-fitted line for an accurate calculation of h and η , it is necessary to gain these values in time windows through which the values of heat flux vary. However, this is difficult with the testing at TRF: Firstly, a thermally-steady state is reached and maintained only after flows normalize within the testing section, leaving only a brief time period of valid data for this time period. Secondly, because of the thin-walled structures of the tested airfoils, thermal penetration occurs (driving a steady heat flux and less-variant wall temperatures) very quickly, causing a very small distribution in the points for the Popp-style plotting.

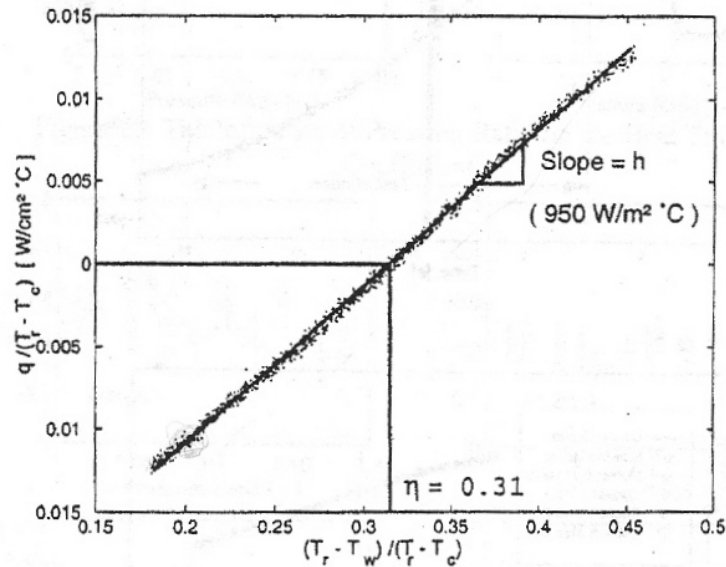


Figure 31: Graph of normalized heat flux and driving temperature difference (taken from Popp, et al., 2000)

4.3 Data Reduction: Time-Resolved

Data was processed both in two sections: as time-resolved sets (to gain an appreciation for characteristic unsteadiness) and time-averaged sets (to calculate parameters of performance in the environment). Data from time-averaged sets were taken from the full data traces of each run (the full 0.0-5.0 seconds of data collection), but parsed down to a 2000 Hz sampling frequency. Data for time-resolved sets was taken from the first 1.2 seconds of relatively steady flow (after shock passage/flow normalization—2.5 to 3.7 seconds) at 50 kHz. Sample data from the full runs was shown previously in Figure 19 and Figure 27. Sample data from the data for time-resolved analysis of Run 3 is seen in Figure 32, Figure 33, and Figure 34 for the pressure transducers, the vane heat flux, and the BOAS heat flux, respectively. All vane-mounted gauges are at 60 % span.

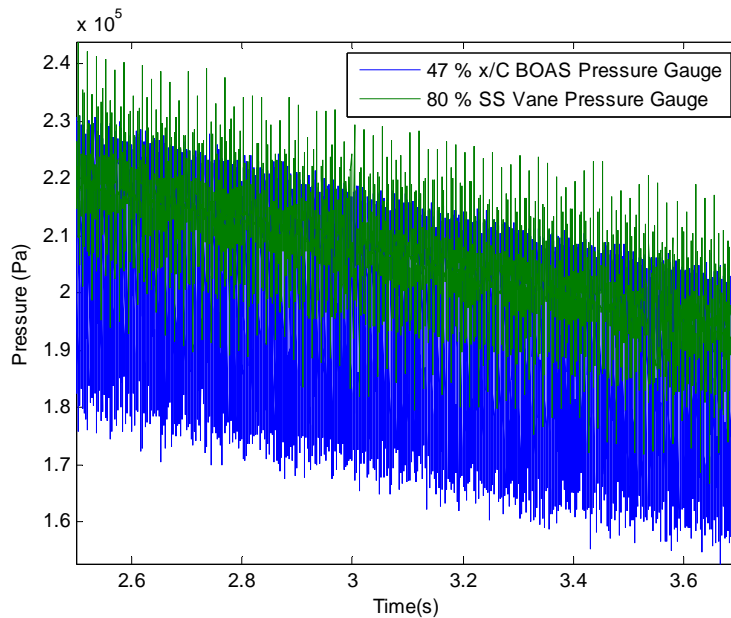


Figure 32: Sample time-resolved pressure gauge traces

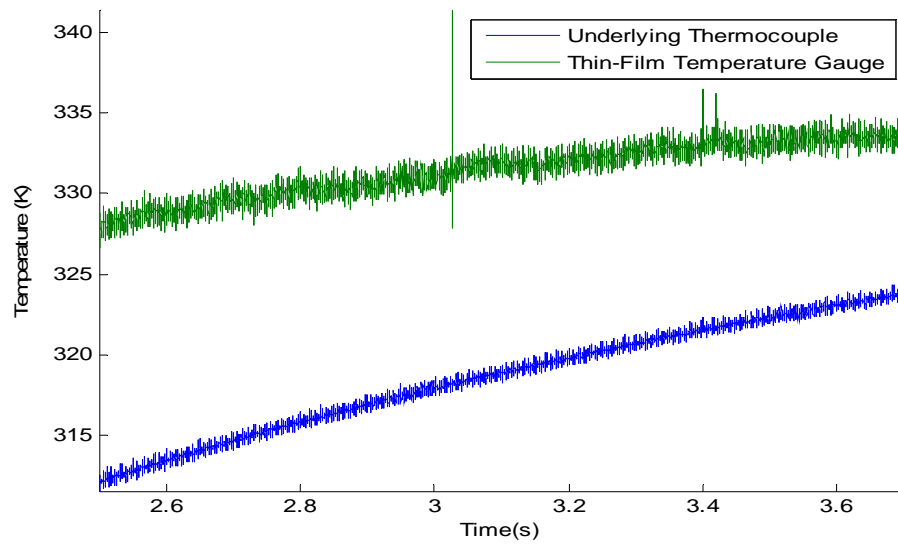


Figure 33: Sample time-resolved heat flux gauge traces: 74 % SS vane

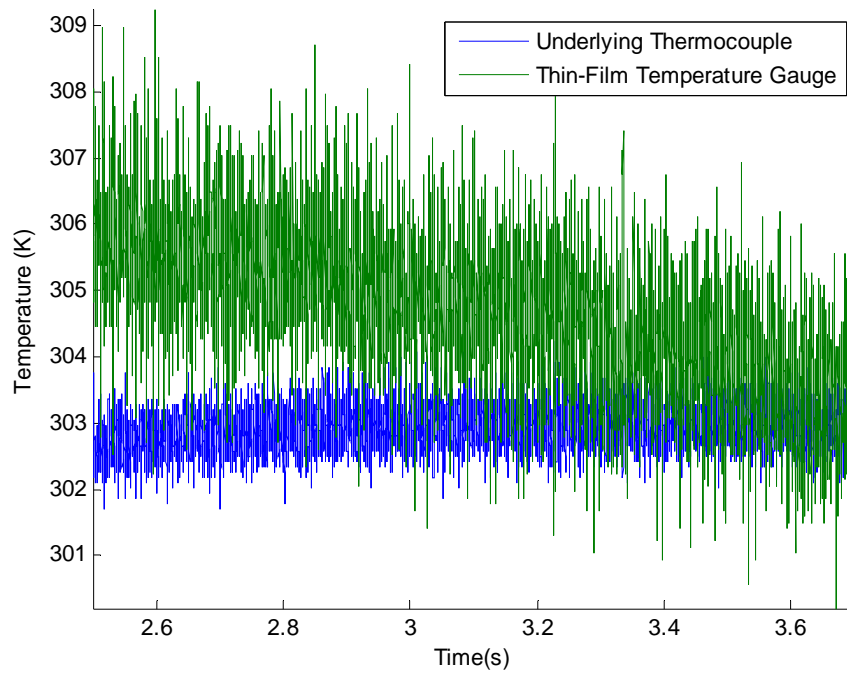


Figure 34: Sample time-resolved heat flux gauge traces: 47 % x/C BOAS

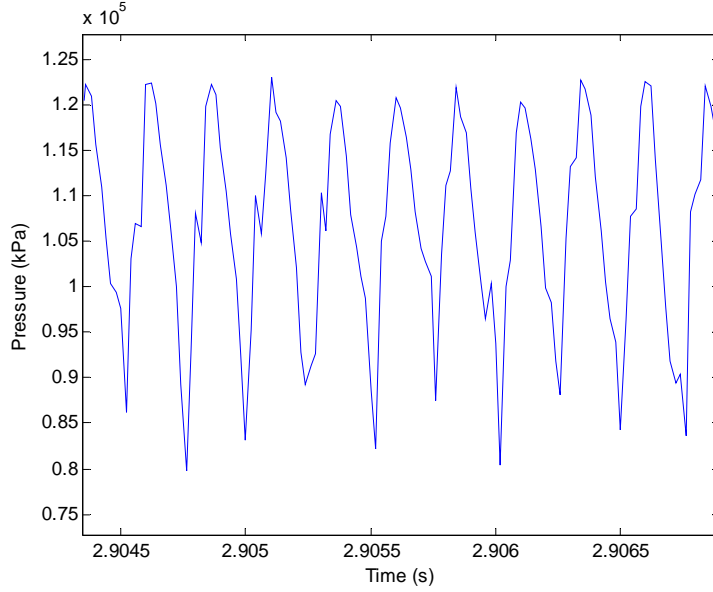


Figure 35: BOAS-mounted pressure gauge: sample trace

Data from a BOAS-mounted gauge is reproduced on a smaller scale in Figure 35 to gain a further appreciation for the cyclic shape of the unsteadiness. The inherent fluctuations seen (minus the randomized spike observed in the thin-film traces of Figure 33 at approximately 3.0 and 3.4 seconds, due most likely to a noise spike) are not due to noise or turbulence, but rather due to the effects of rotation of the rotor. This was confirmed by performing a fast fourier transform on the traces. This was done for a series of sample gauges, all which show a spike in the FFT at the blade-pass frequency, f_{BP} , (approximately 6.38 kHz for Run 3—at an average of 6600 RPM), calculated as:

$$f_{BP} = \frac{RPM}{60(\frac{sec}{min})} \cdot N_{Blades} \quad (22)$$

Where $N_{Blades} = 58$ (blades in the rotor stage). To gain the unsteady portion of each trace, the average value of each trace was subtracted from its value at each finite point in time, and the deviation from this was taken as an absolute value. The data was then

normalized again over the average value of the trace in the time window. This process is shown as:

$$|T_t - T_{ave}| / T_{upstream} \quad (23)$$

Where T_t represents the temperature at a finite point in time (replaceable with P for pressure traces). The data was sampled across 110 revolutions of the rotor, or nominally 1.0 seconds. A sample of this is seen in Figure 36.

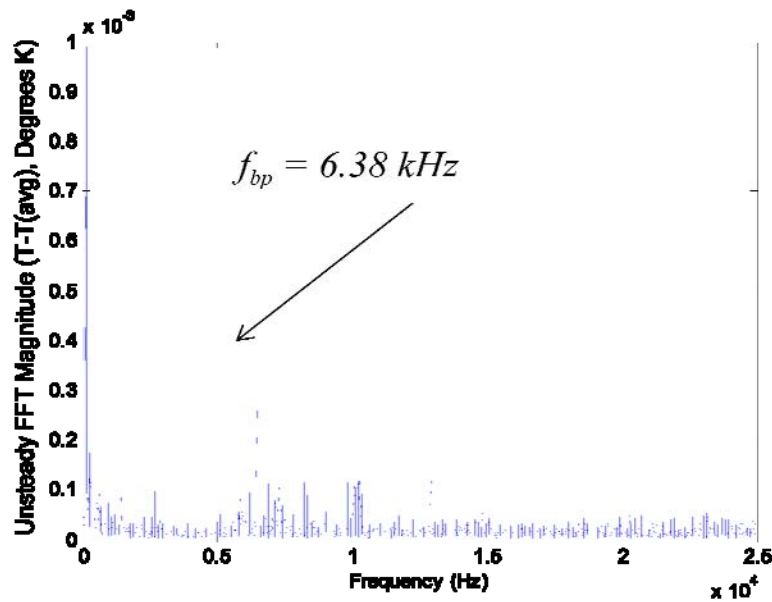


Figure 36: Sample FFT: 47 % x/C BOAS thin-film temperature gauge

A definite frequency of the unsteady behavior of the trace was observed. The repetition of the blade-pass frequency at twice and three times its base frequency (and the half-magnitudes at these locations) is characteristic of a standard FFT shape. The spike in unsteadiness is observed at approximately 6.38 kHz, as expected. To gain a further appreciation for the occurrences through rotor disc rotation, the frequencies across which the FFT was calculated were then normalized by the engine speed (6600 RPM, or 110 Rev/Sec, in this case) calculated as such:

$$\text{Engine Order} = f / (\text{Rev/sec}) \quad (24)$$

An example of this is seen in Figure 37 for the same gauge.

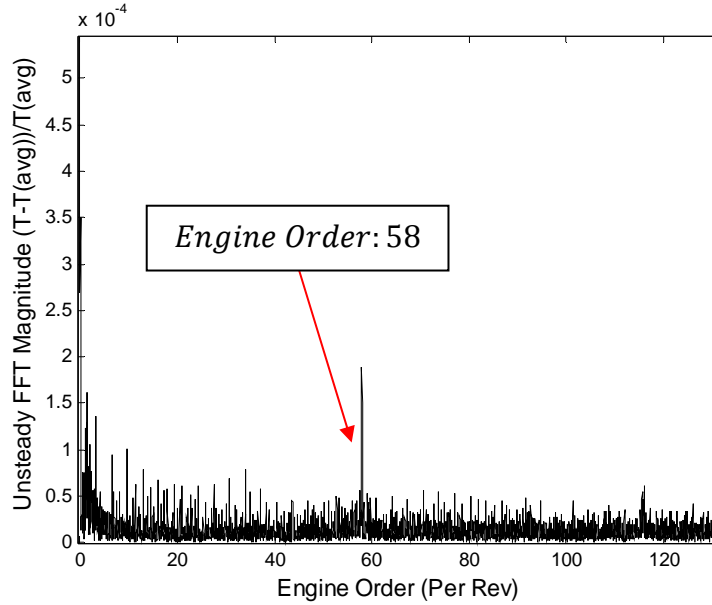


Figure 37: Sample FFT by engine order, 47 % x/C BOAS thin-film temperature gauge

Wider bands in surrounding the Engine Order of 58 can be attributed to variation in rotor speed through the time window, and higher spike at very low engine orders and frequencies (such as Engine Order = 1) may correspond to higher spikes occurring once per revolution. This is reproduced once again, with a view zoomed view at the lower engine orders. The presence of the lower engine orders (below 58 per revolution) is evidence of singular and several-event per revolution occurrences, characteristic of the variations in tip clearances and differences in blade tip configurations.

This unsteadiness, as stated previously in the review of current literature, is quite pronounced on the suction side of the vane trailing edges, as well as along the BOAS. This normalized, absolute, unsteady-only FFT analysis was performed for several of

these gauges for which unsteadiness was quite pronounced, as seen in the more of the figures that follow.

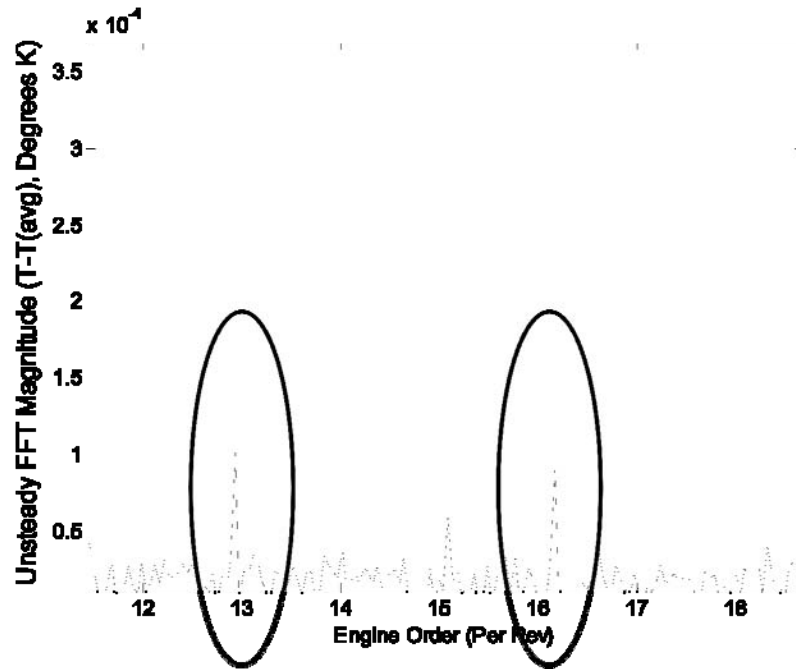


Figure 38: Area view of sample FFT, 47 % x/C BOAS temperature gauge

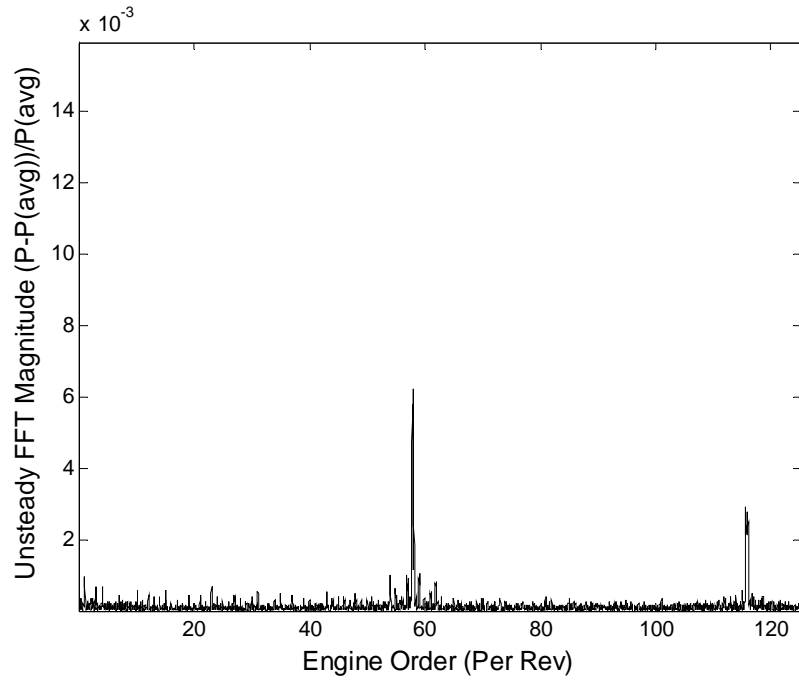


Figure 39: Sample engine order FFT, 47 % x/C BOAS pressure gauge

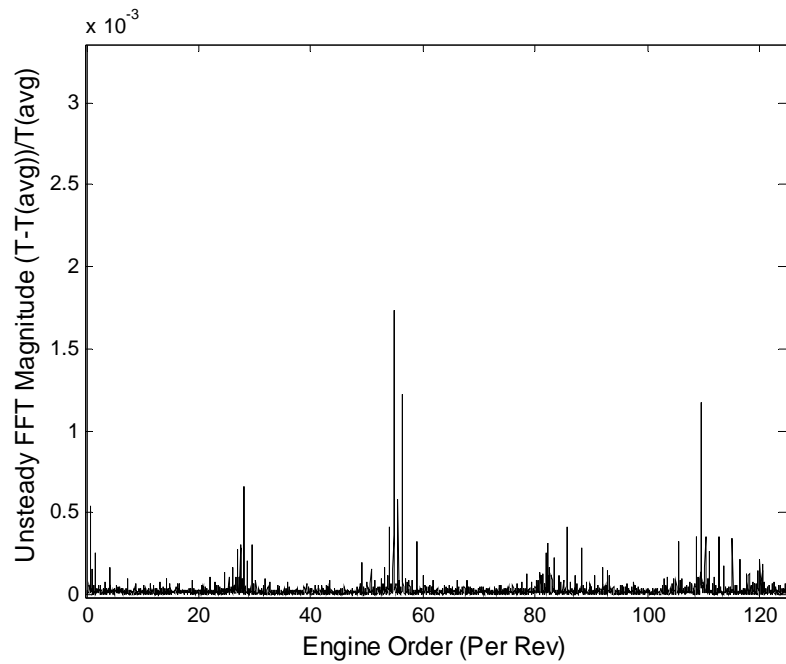


Figure 40: Sample engine-order FFT, 90 % SS vane embedded thermocouple temperature

Again, the second harmonics of this vane-passage frequency are also seen at an engine order or approximately 116, at half the magnitude of the principle order of 58, as would be expected in a FFT analysis. As seen in Figure 40 is the FFT for a vane's suction side embedded thermocouple. The presence of engine orders at twice the number of blades is not surprising; however, the fact that these also exist at approximately half and one-and-one half the number of blades may lend itself to provoking investigations surrounding the concept of thermal lag and heat flux as disturbances move through the thermal insulating layer. This will be touched on further when discussing results.

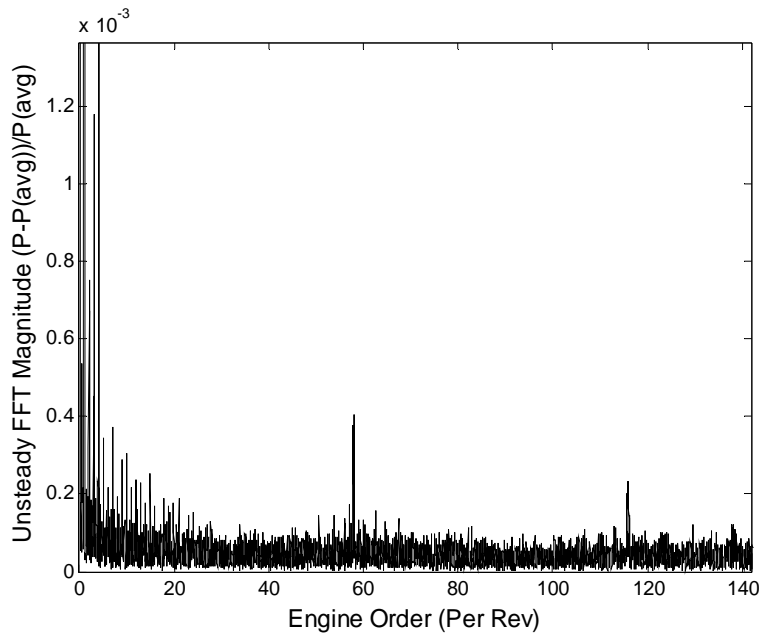


Figure 41: Sample engine-order FFT, 90 % PS vane pressure gauge

Seen in Figure 41 is the FFT for the pressure side of a vane pressure gauge. While fluctuations do not nearly approach the magnitude of those fluctuations on the BOAS (as would be expected), their presence at the Engine Order of 58 further proves the presence of unsteadiness driven by rotor rotation.

Though magnitudes of these FFT reductions have been used to describe and characterize the unsteadiness along the vanes and BOAS (Urbassik, 2003), their usage in the current study was simply to understand source of the unsteady variations. The FFT has helped us establish this.

4.4 Time-Averaged Data Reduction Methods

The process and reasoning used to validate the delivery of the film-cooling parameters (overall effectiveness, mean heat flux, adiabatic effectiveness, and heat transfer coefficient) from the time-resolved data has been discussed at length (Polanka, et al., 2008). For the purposes of gathering this preliminary/authenticating information, four sets of heat flux/temperature gauges were used, at 47 % and 86 % axial blade chord for the BOAS and 65 % PS and 90 % SS for the vane surface, whose results are expected to be representative of the spectrum of outcomes possible upon data processing.

4.4.1 Overall Effectiveness

With specific concern to TRF testing, determining the time windows from which to gather data for overall effectiveness (ϕ) becomes an issue. For the 47 % axial chord of the BOAS (in Figure 42) and 90 % SS of the vane (in Figure 43) in Run 1 of the experiment (representative of the timing and thermal activity for each), the temperatures used in calculating overall effectiveness and heat flux are plotted as time-traces through the experiment. These include the freestream (T_∞ —measured upstream of the test section), and coolant temperatures (T_c —measured shortly before delivery to the test article), the heat flux gauge’s thin-film surface temperature (T_w) and underlying thermocouple temperature (T_m)—intended to represent the temperature of the bulk metal

of the airfoil. Freestream total temperature is plotted against the right-hand side vertical axis labels, with the others plotted against the left-hand axis.

In both the BOAS and vane locations shown in the figures, coolant temperature rises dramatically shortly after the main valve opening (shortly before the two-second mark). This occurs due to the movement of the compression wave through the testing section of the facility, at which point in time the high-pressure freestream fluid actually forces itself back through the coolant holes and slots. This effectively makes coolant flow of no effect, as none is being ejected onto the surface of the airfoil until flow renormalizes. Therefore, any data before this re-normalization (which occurs at approximately 2.5 seconds) is not usable and shall be considered part of the transient effects of the shock passage in the transonic test section.

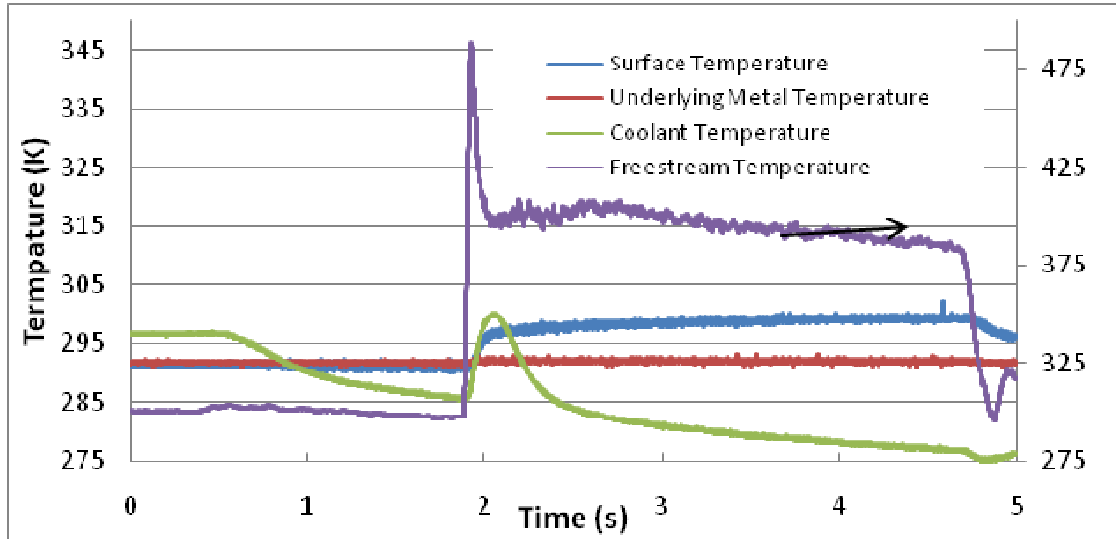


Figure 42: Overall effectiveness temperature histories--Run 1, 47 % x/C BOAS

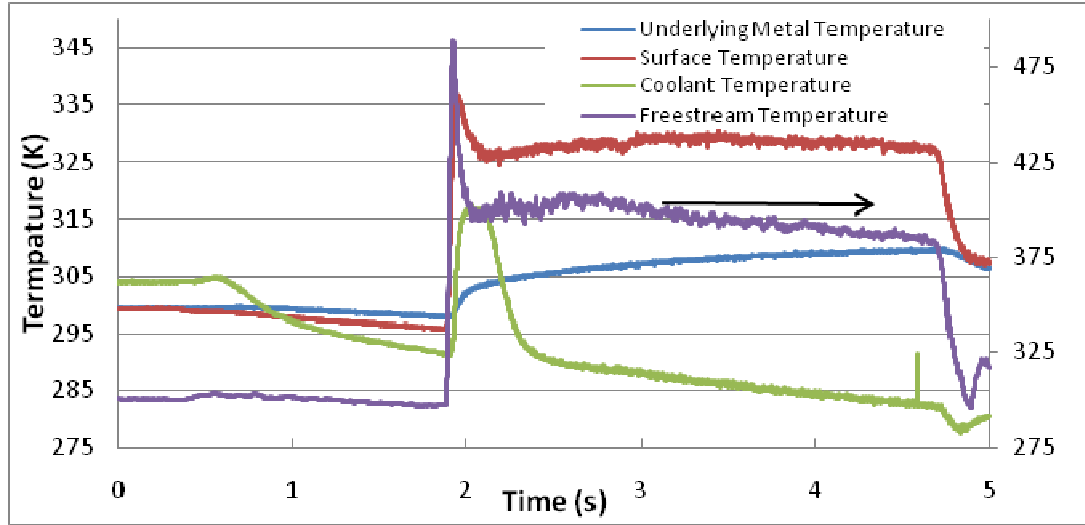


Figure 43: Overall effectiveness temperature histories--Run 1, 90 % SS vane, 60 % span

Also of importance is a close examination of the underlying metal temperature. Because the metallic airfoil and rotor shroud are not initially at a temperature representative of a ‘steady-state’ operating condition, it takes some time for the metal to heat and reach a steady temperature. This is an effect of both the thermal lag of the metal and the cooling at its given location. While the metal is still heating, heat flux is also unsteady. Though the freestream temperature and coolant temperature continue to decay through the experiment (until the closing of the isolation valve), the temperatures driving the calculation of the heat flux reach proportionately steady values during the blowdown (at approximately 3.5 seconds in these experiments). This corresponds to a relatively steady heat flux. Heat flux at these two gauges is seen in Figure 44 (unsteadiness is attributed to the rotating rotor disc in the stage). While heat flux still continues to decrease throughout due to the changing blowdown, the general trend remains constant after 3.5 seconds, evidence of a stable condition being established. This is further reflected in ϕ . Overall effectiveness is a normalized temperature that takes into account the changing values of the relevant temperatures. Values calculated at each point in time are seen in Figure 45.

For the purposes of the calculating ϕ in these experiments, the time window of 3.5 to 4.5 seconds will be used. During this time, the value of ϕ varies less than 10 percent for each of the representative gauges. A handful of locations still experience a slight decay in ϕ , suggestive that a full-steady condition has not been achieved. As such, the value obtained represents the maximum ϕ at each location.

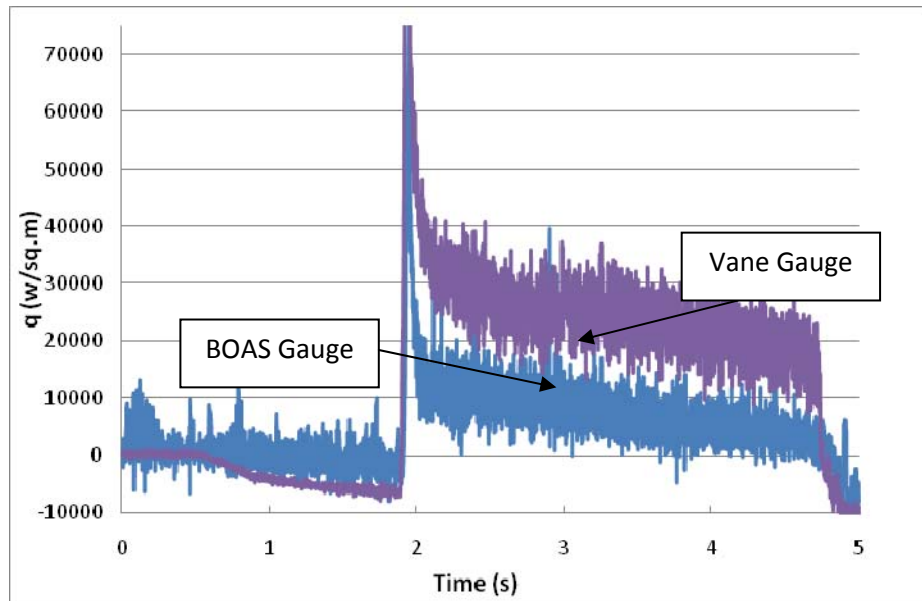


Figure 44: Heat flux histories—Run 1, 47 % x/C BOAS and 90 % SS vane, 60 % span

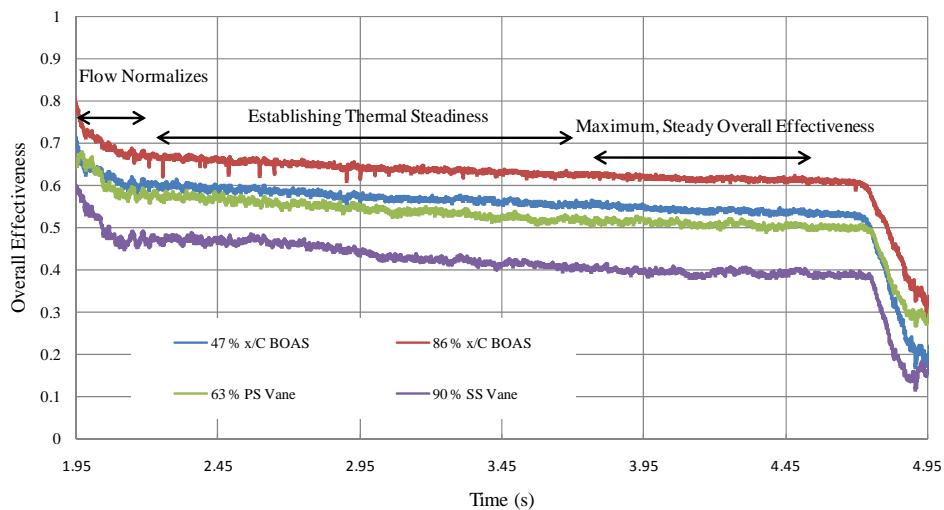


Figure 45: Overall effectiveness histories in time of interest--Run 1

4.4.2 Adiabatic Effectiveness and Heat Transfer Coefficient—Method of Popp

The Virginia Tech group developed a method presents a method from which the data from which the data collected in the TRF experiments can be used to calculate both adiabatic effectiveness (η) and film-cooled heat transfer coefficient (h_f). Their data, replicated previously in Figure 31, traverses from upper-right to lower-left, with a corresponding decay in heat transfer. The data presented in this previous experiment can be approximated as semi-infinite heat transfer because the thicker walls and larger scale of the airfoil do not allow the metallic airfoil to reach a steady-state temperature value, and thus a steady-state heat flux, through the experiment. Heat flux decreases as the wall warms; therefore, a steady thermal state is never reached, and the plotted points continue traveling along this line. As discussed previously, this temperature data taken for the experiments of current interest at TRF reaches a proportionately steady value after approximately 3.5 seconds, corresponding to a reasonably steady value of overall effectiveness.

In order to gain an appreciation for the use of the ‘Popp-style’ methodology for current testing, data from the same four gauges mentioned previously were explored. X- and Y-values, as dictated by the Popp-style plots, were found from values averaged over 50-millisecond windows throughout the main run (however, only from main valve opening through the closing of the main valve).

Data from Figure 42 is presented again in Figure 46, with a focus on the initial part of the blowdown. This allows for a greater understanding of each section into which the Popp-style plots are broken.

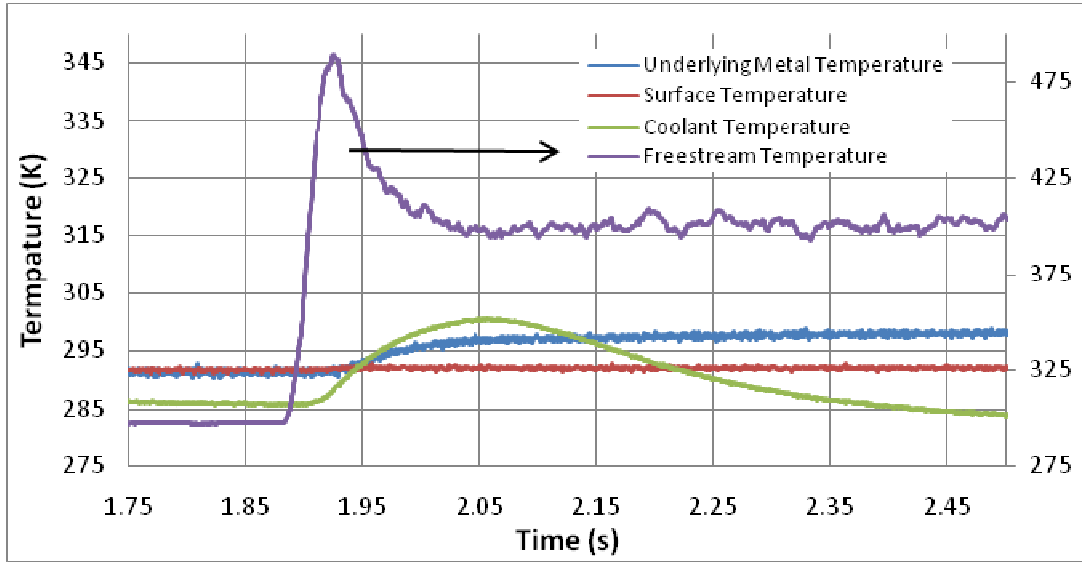


Figure 46: Temperature histories--Run 1, 47 % x/C BOAS gauge

The four gauges are plotted and broken down into time windows: (1) A recognizable transient period, from the main valve opening through the passage of the transient compression wave and renormalization of the coolant flow, as identified by the flattening of its temperature trace--approximately 1.87 s to 2.5 s, (2) a period of heat flux decay, from 2.5 to 3.5 s, (3) an initial section of thermally-steady points, from 3.5 to 4.0 s, and (4) a final section of thermally-steady points, from 4.0 to 4.5 s. The Popp-style plots are seen below in Figure 47, Figure 48, Figure 49, and Figure 50.

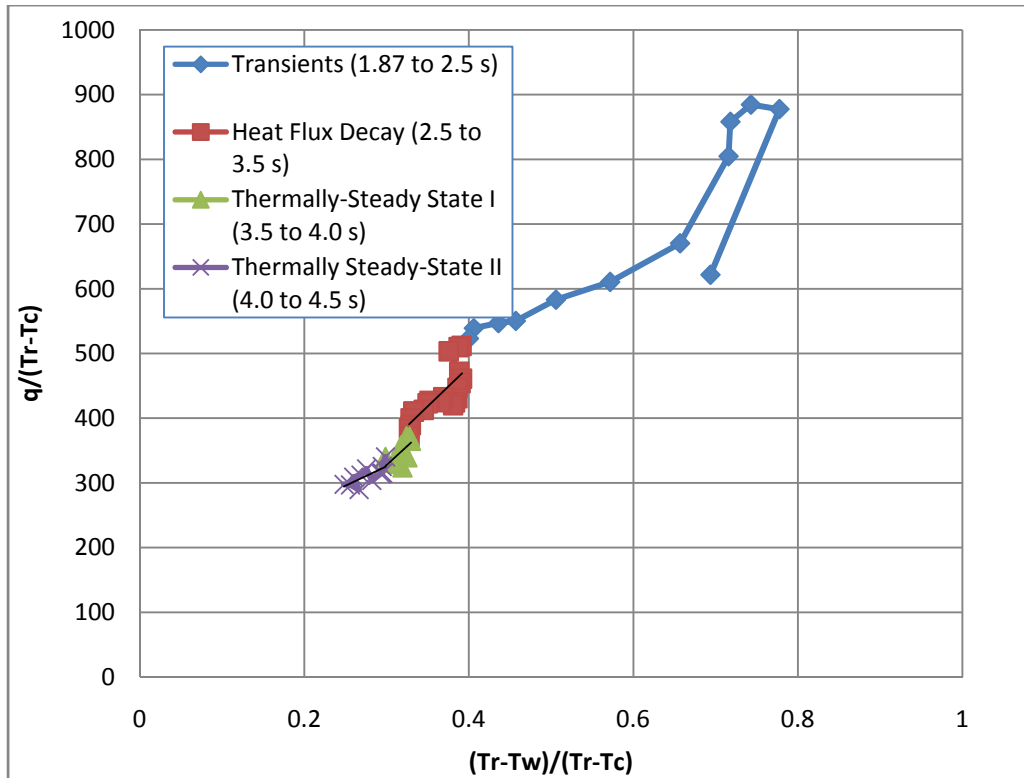


Figure 47: Popp-style plot--Run 1, 47 % x/C BOAS gauge

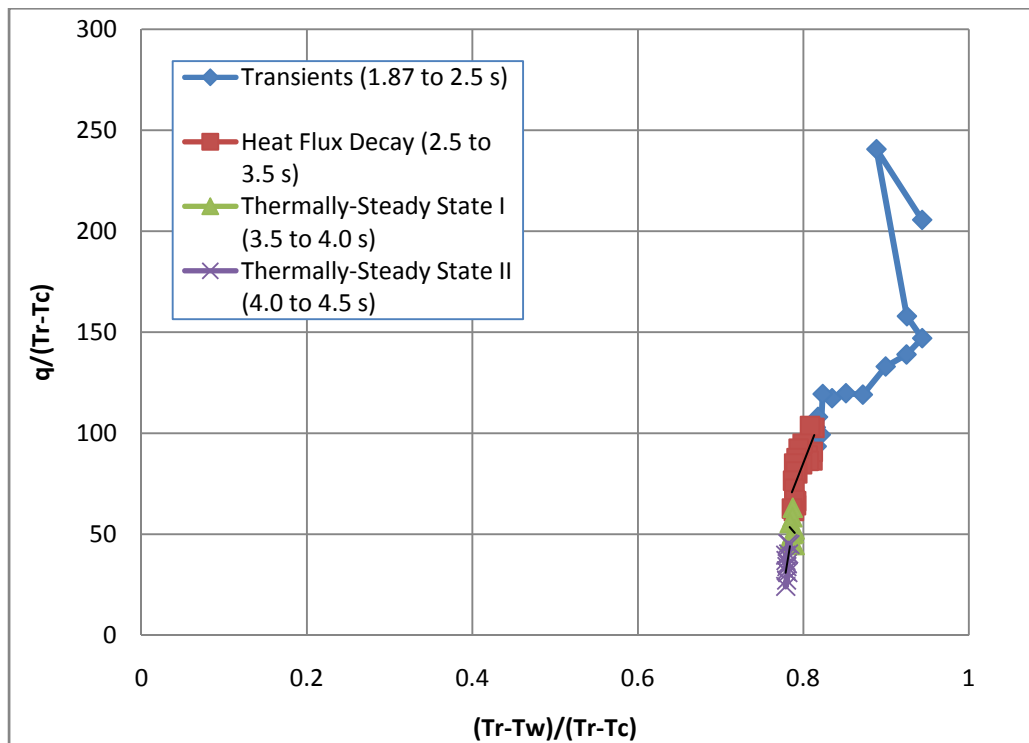


Figure 48: Popp-style plot--Run 1, 86 % x/C BOAS gauge

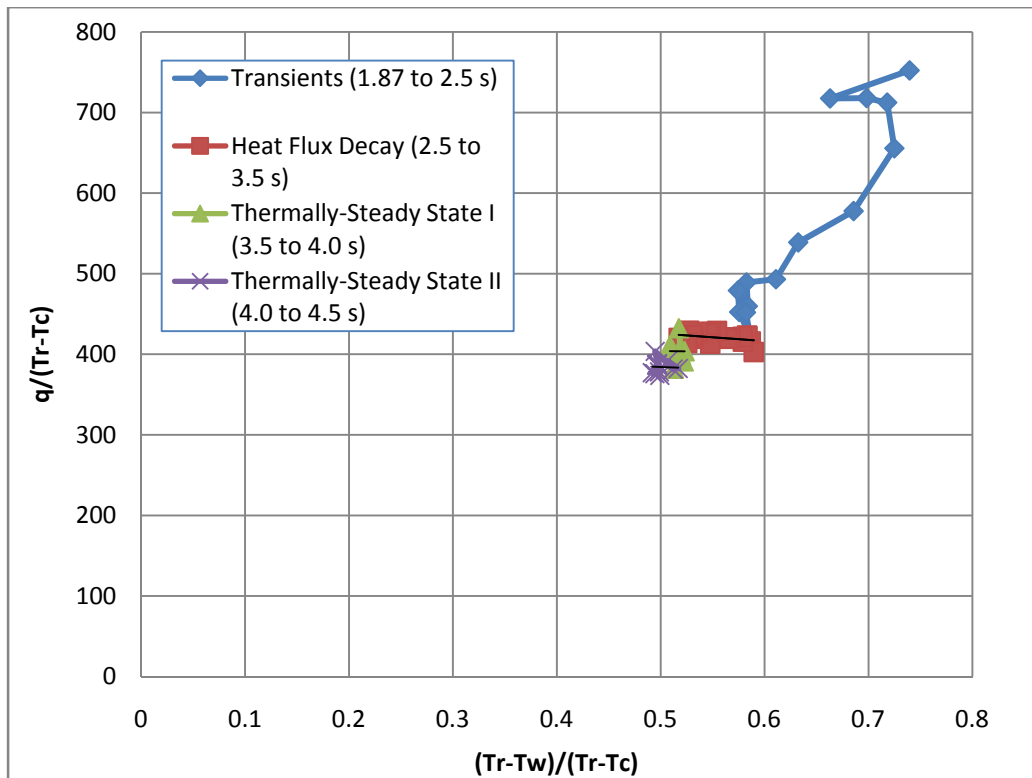


Figure 49: Popp-style plot--Run 1, 63 % PS vane gauge, 60 % span

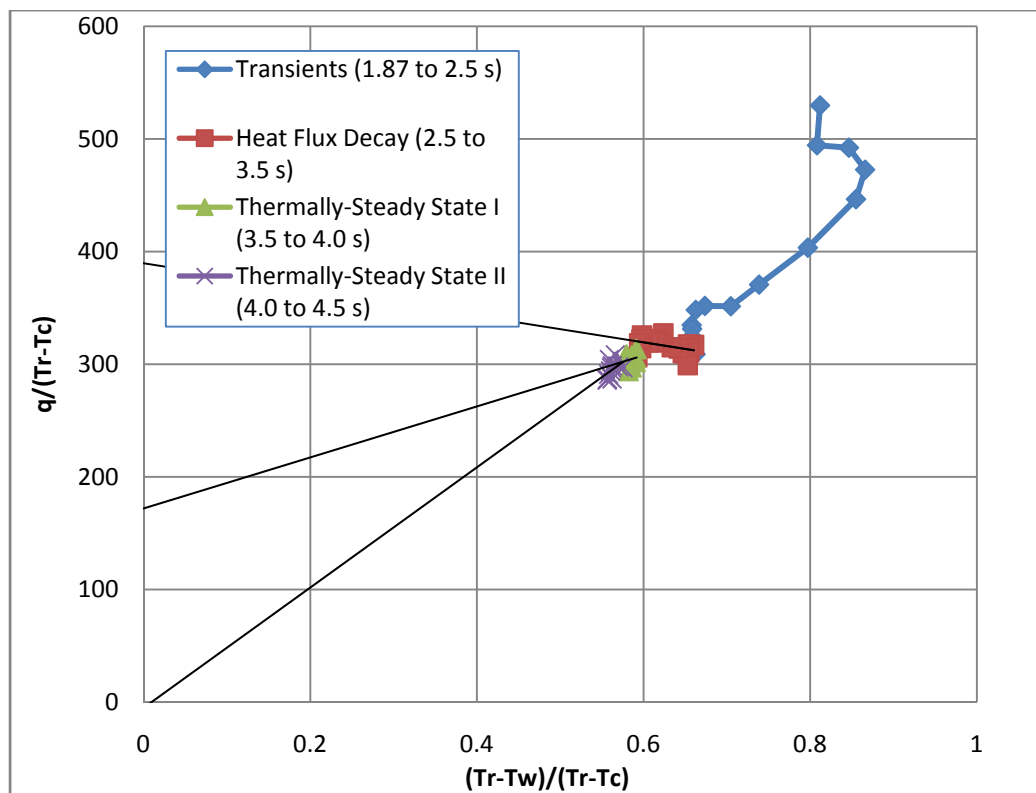


Figure 50: Popp-style plot—Run 1, 90 % SS vane gauge, 60 % span

It should be noted, with regards to each timing window, that: (1) the transient conditions move along the x- and y-axis greatly, as would be expected in a transient region, (2) heat flux decay in the second region produces a line-style movement as was seen in the data produced with the semi-infinite conditions as in Figure 31, and (3 & 4) the thermally-steady state produces a grouping of points in very close vicinity, as would be expected. The values seen collected from time windows (1) and (2) are not desirable, as the thermal condition has not been established.

Also plotted for the 90 % SS vane gauge location from each of the last three windows are the curve-fitted slope-intercept forms of the lines produced a Popp-style extrapolation. Because this is not consistent with each grouping, it becomes of vital importance to assure that the condition is thermally steady when finding this extrapolation (otherwise any number of results could be found for values of adiabatic effectiveness and heat transfer coefficient). This will be discussed further later.

4.5 Time-Resolved Data Reduction Methods

As mentioned previously (in section 4.3), time-resolved data was proven to have frequency content most pronounced at the blade-pass frequency. In order to gain an appreciation for the characteristics of this unsteadiness, ensemble averaging techniques were used. These were applied to pressure, temperature, and heat flux traces for each area of interest. The ensemble-averaged results were then applied to find further results, including ‘phase-locked’ blade passages and unsteady envelopes. The end goal of the ensemble-averaging technique in this experiment is to gain a true representation of single blade passage events across a vane wake or at a point along the rotor stage’s shroud. This

was employed successfully in previous data analysis of pressure variations due to unsteady effects at TRF (Urbassik 2003). A basic representation of the ensemble-average for the purposes this data reduction is:

$$Q_N = \frac{1}{N} \sum q_n \quad (25)$$

Where Q , heat flux, for a point along a rotor passage is defined as the average of N heat fluxes (q) which occur at points n . The data reduction process is used to effectively gain an ensemble-averaged depiction of blade passage events based upon several successive blade passages. During a run, data for temperature, pressure, and angular position of the rotor disc is gathered at high frequency. With data collected at operating speeds of the engine, each rotation of the rotor disc, containing 58 blades, is represented by approximately 420 data points, varying with engine speed. The time indices for angular positioning are aligned with those of the temperature and pressure data, and each point of aerothermodynamic data is allocated to its respective point in angular positioning.

To more easily allow for ‘phase-locking’ of each data signal, each ensemble average was represented by 580 data points (approximately 10 points per blade passage). While this represents an imaginary ‘up-sampling’ of the data, erroneously-formed data points were not incurred, as this was done by linear interpolation among the collected data points. All rotations are normalized to have this number of data points (580) across one revolution, equally spaced along angular position (from 0 to 2π , or approximately 6.28 radians). An average of temperature and pressure data across several rotations may then be taken at any distinct angular displacement of the rotor. The average of many of these rotations is thus taken to be representative of the aerothermodynamics occurrences

at a distinct radial position throughout a standard rotation of the rotor disc. In Figure 51, a sample of the ensemble-average of a trace overlays three of the revolutions from which it was averaged. While this is not the entire revolution (rather that shown from the angular displacement of the rotor disc from approximately 1.1 to 3 radians), it shows the result of the ensemble-average process. The data was taken from a shroud-mounted pressure transducer during Run 1, and is representative of the general shapes and effect seen by the ensemble-averaging of any of the unsteadiness-affected data signals. The full results of the ensemble-averaging of this pressure transducer are presented in Figure 52.

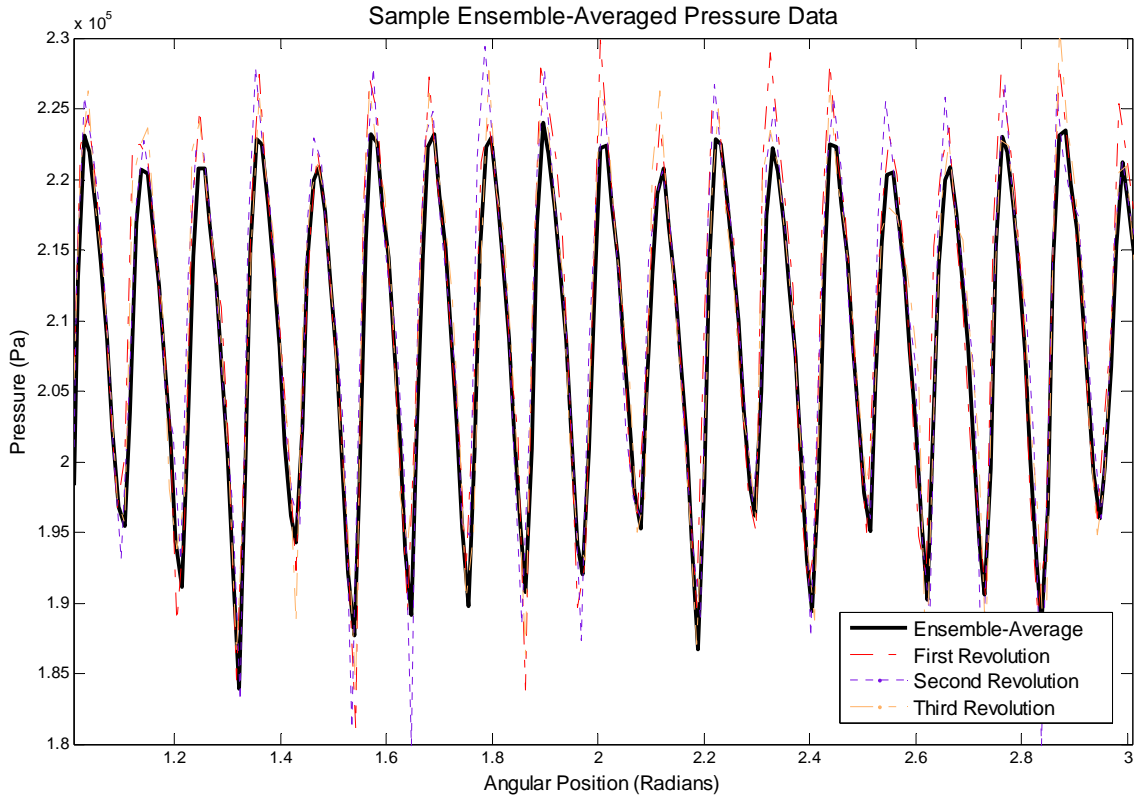


Figure 51: Sample ensemble-averaged pressure data, 47 % x/C BOAS pressure gauge

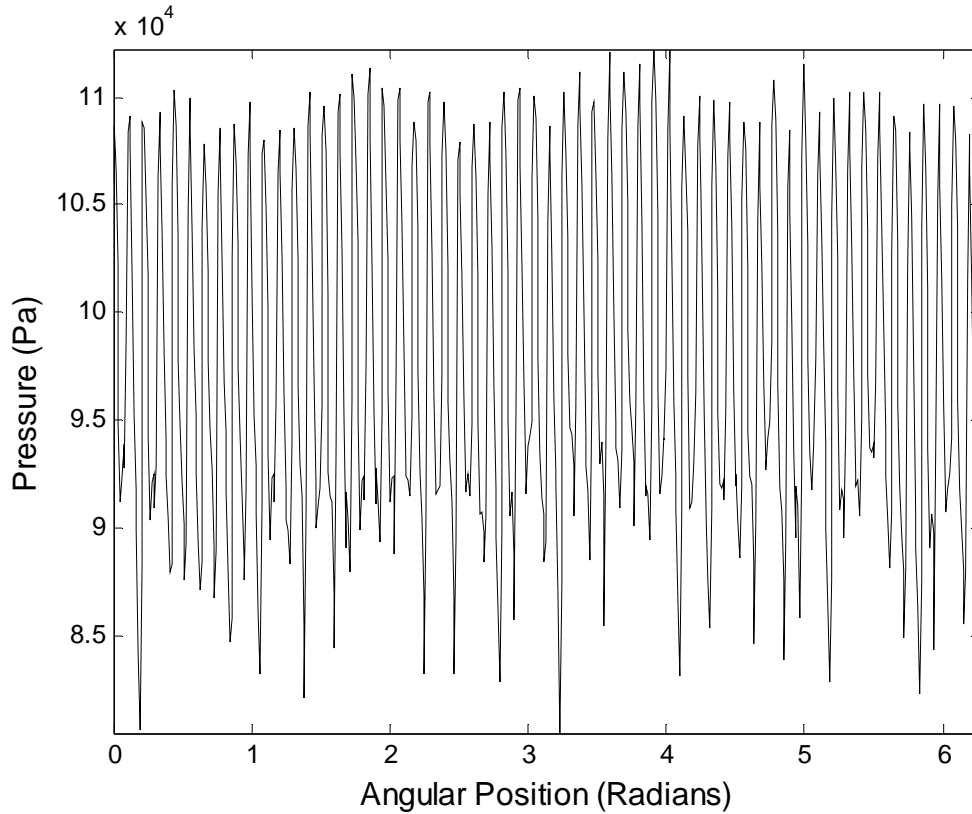


Figure 52: Sample ensemble average, 47 % x/C BOAS pressure gauge

As would be expected, 58 blade-passage events are observed during the course of a full rotation of the rotor disc, with a peak in pressure corresponding to the passage of a blade itself, and the troughs to the inter-blade gaps. In order to gain more perspective on the inherent unsteadiness in pressures, temperatures, and heat fluxes, several other variations of this ensemble-averaging were performed, as seen in Figure 53 (normalized by the radially-corresponding freestream pressure upstream of the vane stage), and in Figure 54 (first with unsteady-only values taken by subtracting the mean local pressure, and then normalized by the freestream). Not all variations of this process were used for all gauges or presentations of the data.

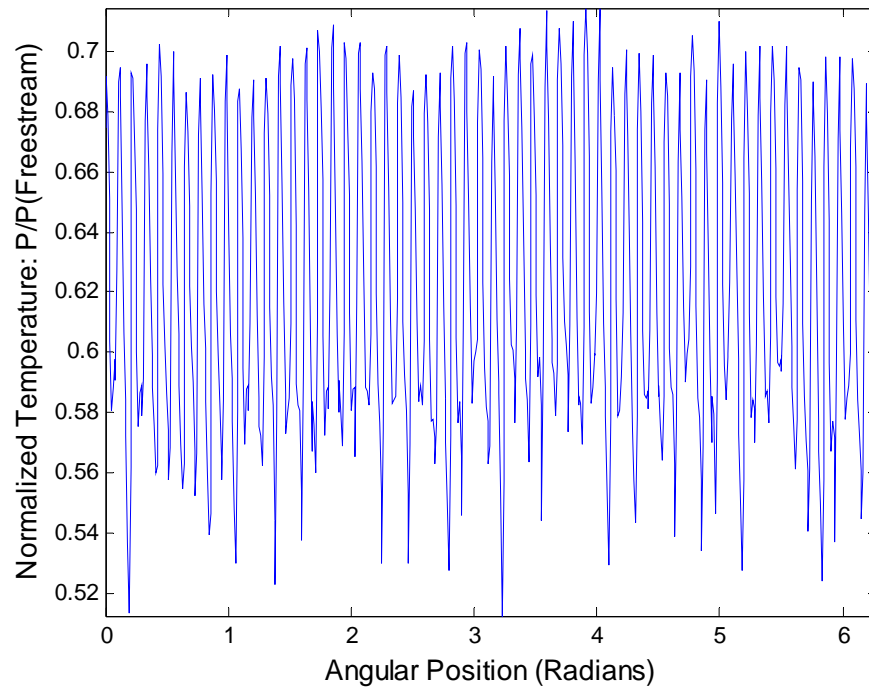


Figure 53: Sample freestream-normalized ensemble average, 47 % x/C BOAS pressure gauge

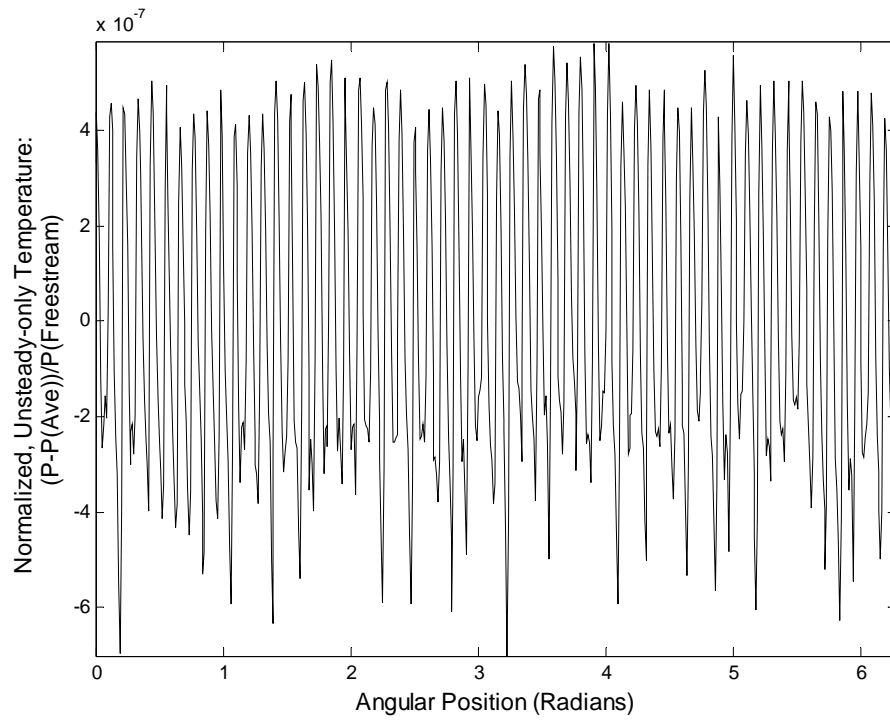


Figure 54: Sample freestream-normalized, unsteady-only ensemble average, 47 % x/C BOAS pressure gauge

While this allows for an appreciation of the characteristics of a full rotor passage, it was desired to gain an appreciation of each blade passage event and the nuances of its effects on the local pressures, temperatures, and heat flux. To achieve the ‘signature’ (pressure, heat flux, or temperature along the shroud or vane) of an individual blade passage, data at each circumferentially-varying transducer/thermocouple locations was ‘phase-locked’ by shifting its ensemble-average by its angular displacement along the radius of the stator vane. This phase-locking allows for a view of any stationary point (whether along the BOAS or an upstream vane) to be viewed as the rotor passes through it, according to ‘blade phase,’ with the convention seen in Figure 55. Blade phase of 50 % is recognized as the direct passage of a blade’s mean chord over the point.

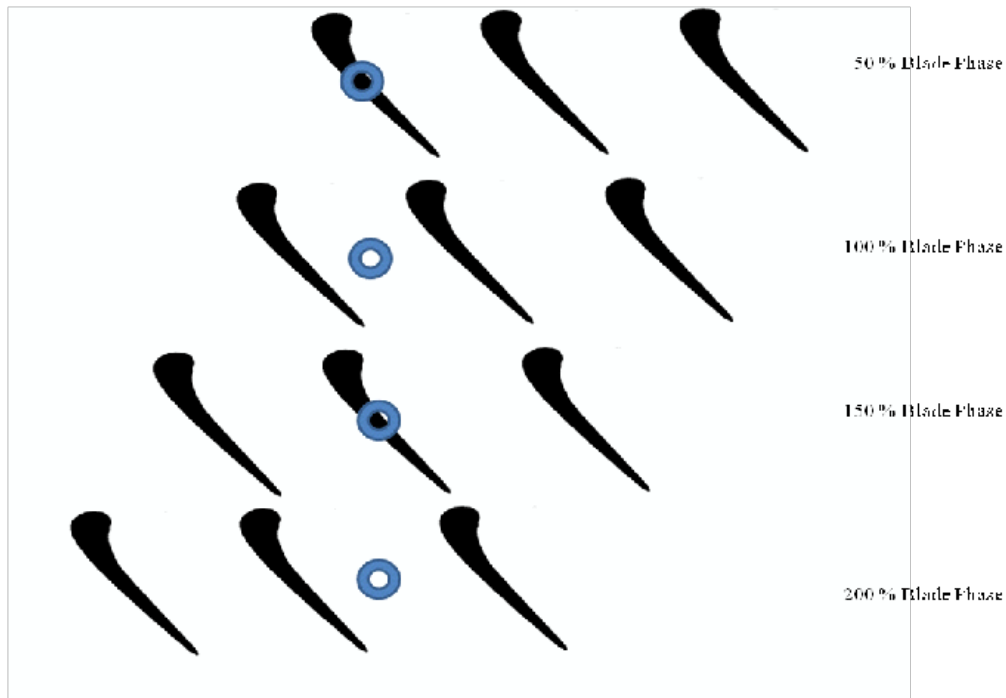


Figure 55: Blade phase convention

In order to gain this ‘phase-locking,’ nearly-identical blades were identified for the purpose of gaining the signatures of each. These were blades of similar tip clearances and tip cooling schemes. For the purposes of the phase-locking, data from all 58

passages was averaged to gain an average shape of a typical blade passage event. While this allowed the typical shape to be seen, it was also desired to compare blades. A layout of the differing blades and their passages is seen for the 47 % axial chord BOAS-mounted gauge in Figure 56.

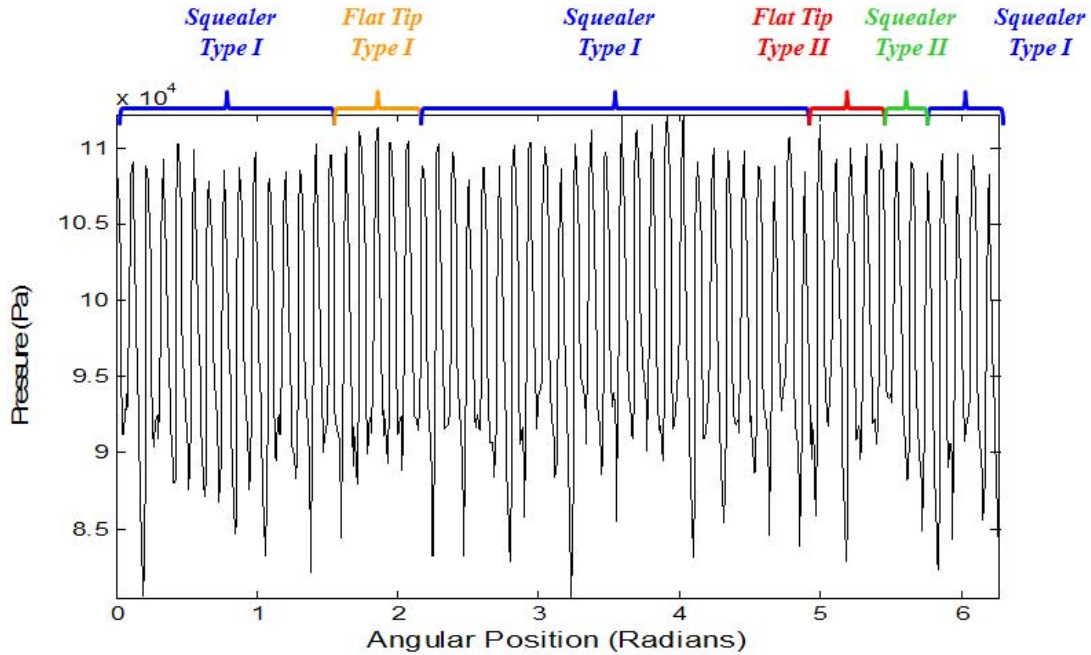


Figure 56: 47 % x/C BOAS-mounted pressure gauge: tip layouts

When gaining the looking at different rotor blades, data from two or three consecutive like blade passages were gathered and averaged over each 100 % blade phase period. This averaged data was repeated to represent a singular blade-passage event, as pictured in Figure 58. The passages of the suction and pressure sides of the gauges are denoted, as is found with current understanding of a blade passage event as described previously in the review of literature.

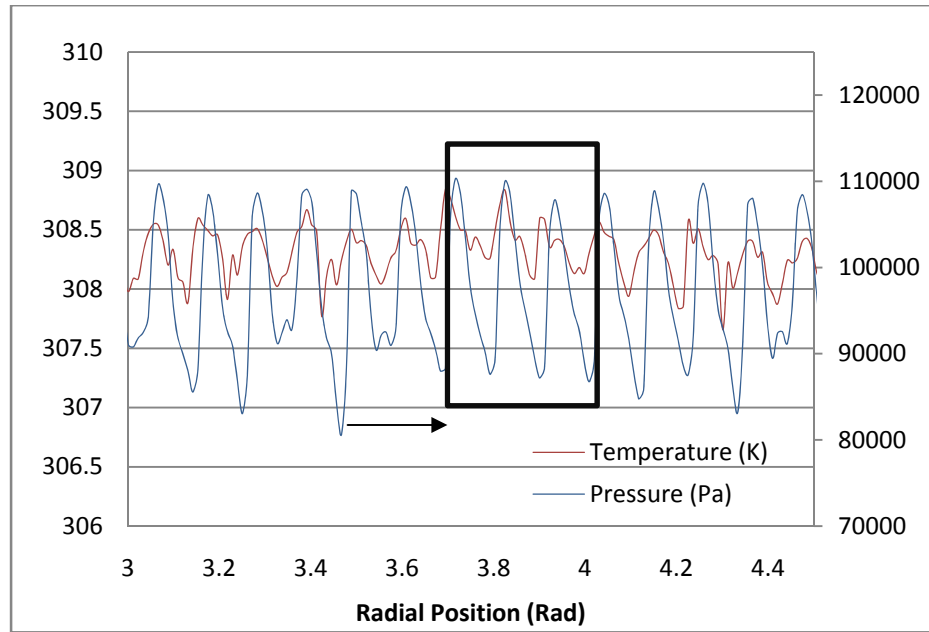


Figure 57: Sample phase-locking data gathering: 47 % x/C BOAS thin-film temperature and pressure gauges

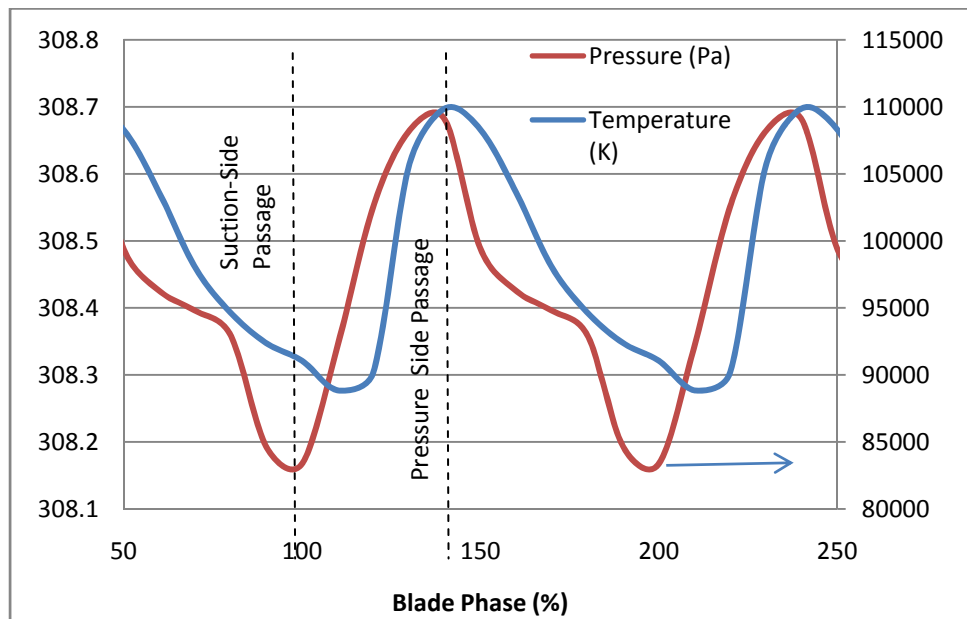


Figure 58: Sample ensemble-averaged phase-locked blade passages: 47 % x/C BOAS thin-film temperature and pressure gauges

Knowing that fluctuations do occur within the temperatures, pressures, and along the vane and BOAS with the passages of rotor blades, it was also desired to find the

unsteady envelopes through which these values pass during a given run. When high-cycle fatigue is used as a design factor, this unsteadiness must become a major consideration. In order to do gain this ‘envelope’ of unsteadiness, ensemble-averaging techniques were once again employed, with data being taken from 3.5 to 3.7 seconds. Two examples of this are seen in Figure 59 and Figure 60, a 60 % span vane heat flux gauge and a BOAS-mounted gauge. To gain the unsteady envelope of heat flux through which the metal must pass, the 58 troughs and peaks were averaged to gain an average high and low heat flux for each location. These are seen as lines through each plot. It should be noted that the heat flux for the BOAS has moved to a value centered near zero, because of the decay of the freestream value through the rotor stage. The average heat flux through the vane gauge is 17515 W/m^2 , and through the BOAS gauge 589 W/m^2 . The unsteady envelope of the vane gauge varies between 8878 and 25839 W/m^2 and for the BOAS gauge between -23457 and 25547 W/m^2 . Similar techniques were employed for the gathering of pressures and temperatures, for Runs 1-3.

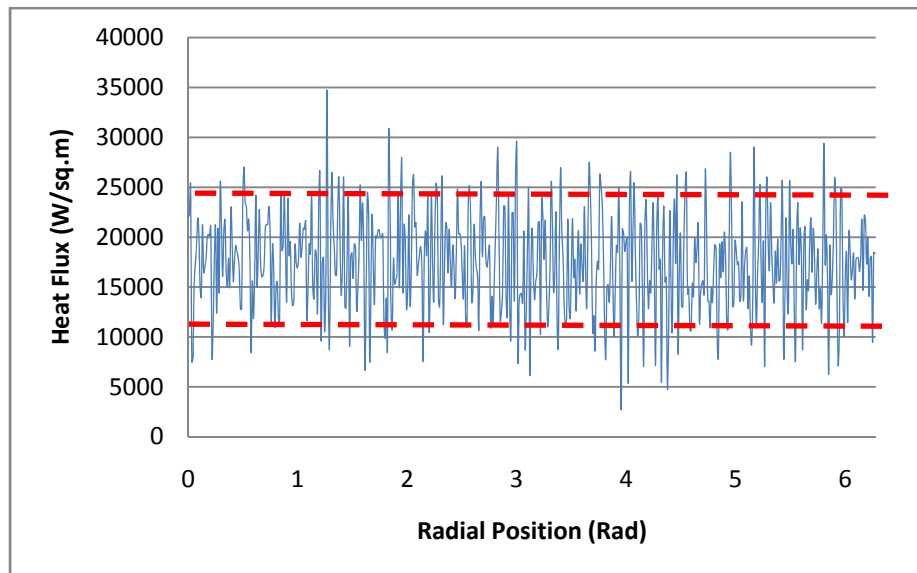


Figure 59: Ensemble-averaged heat flux, 45 % SS vane, 60 % span

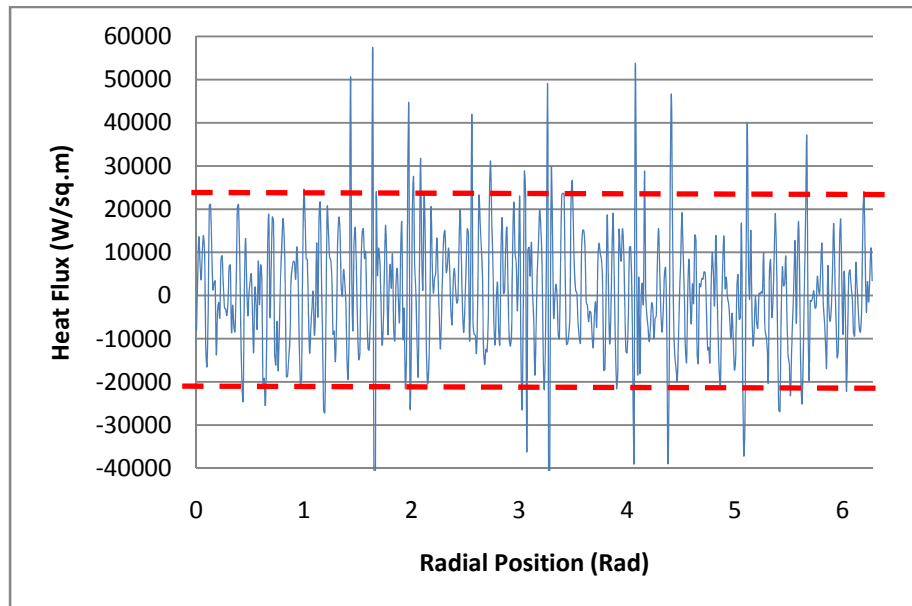


Figure 60: Ensemble-averaged heat flux, 47 % x/C BOAS gauge

5. Results and Analysis—Vane Stage

As mentioned previously, results were processed in two sections: both time-resolved, for analysis of high-frequency unsteadiness, and time-averaged, to gather cooling parameters. Presented first are the time-resolved results and analysis of data gathered from instrumentation along the vane stage, followed by the time-averaged results from the vane.

5.1 Time-Resolved Results

It was first desired to understand the impact of a single blade passing an instrumented vane. To accomplish this, phase-locking ensemble-averaging was used across the surface of the vane. This was performed for Run 3, chosen for the higher engine speeds (with a blade-pass frequency of approximately 6.38 kHz). Ensemble-averaged data was taken from the first 12 revolutions during the steady-state heat flux window of the test, approximately 3.5 to 3.7 seconds. The phase-locked data was taken from the average of all 58 ensemble-averaged blade passages. Pressure disturbances are seen in Figure 61, and temperature disturbances in Figure 62. Pressure disturbances are normalized by the upstream total temperature. The average local static-to-total pressure ratio ($P_{\text{static}}/P_{\text{upstream, total}}$) is tabulated, as well as the normalized magnitude of the disturbances at each location ($(P_{\text{max}} - P_{\text{min}})/P_{\text{upstream, total}}$). Temperature disturbances are shown as raw temperatures.

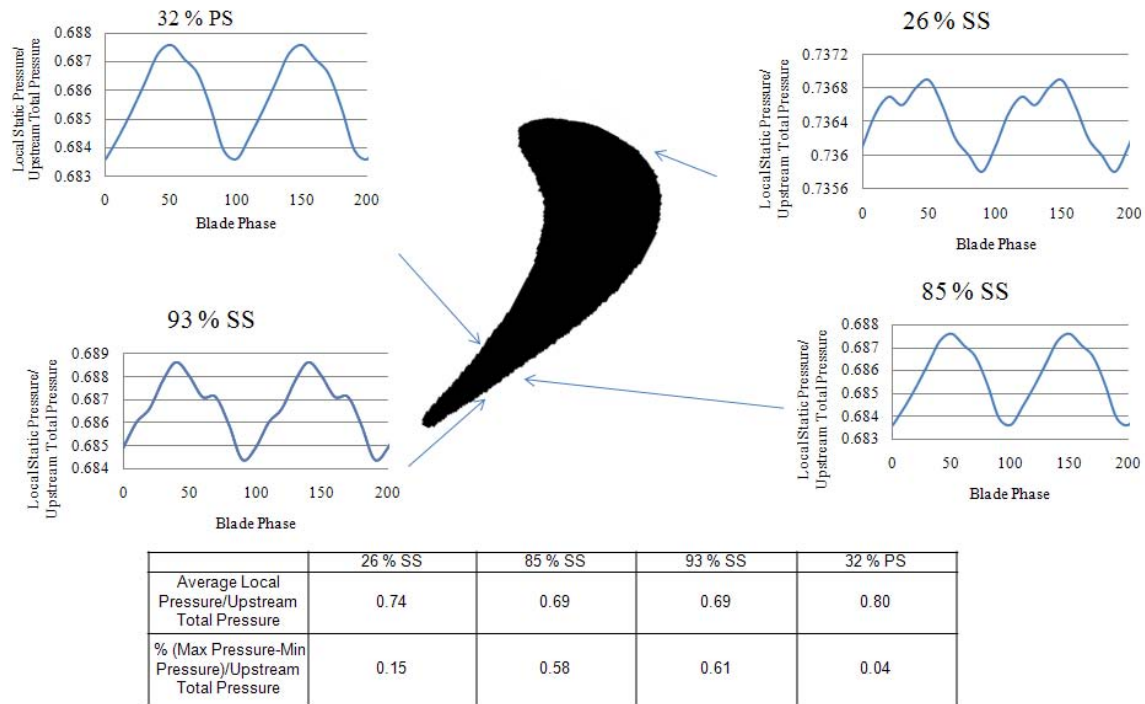


Figure 61: Pressure disturbance along vane surface, 60 % span, Run 3, 3.5-3.7 sec

The results of the pressure disturbances coincide with expected trends. Firstly, highest average local pressures are seen along the pressure side. These average static pressures grow smaller along the suction side. Also, the highest disturbances are seen along the suction side, near the trailing edge of the vane. Disturbances at 93 and 85 % surface length along the SS total 0.61 and 0.58 % of the total upstream pressure, respectively. These are approximately four times the magnitude of the disturbance seen upstream of the vane throats. The severe decay at this point (26 % SS) is coherent with the stage being choked. Finally, the PS disturbance magnitudes are nearly 1/15 of those seen along the TE, SS of the vane.

The peaks of the pressure disturbances are seen at approximately 50 % blade phase, the point at which a trailing blade will pass directly behind a vane. This becomes of concern when evaluating the local disturbances. In this study, the exact natures of the

vane shock and wake reflections have not been fully investigated. The angles at which these phenomena both impinge upon the rotor and are reflected back upon the vane surface must be determined as a function of rotor position in order to gain a further appreciation for the shock and wake occurrences.

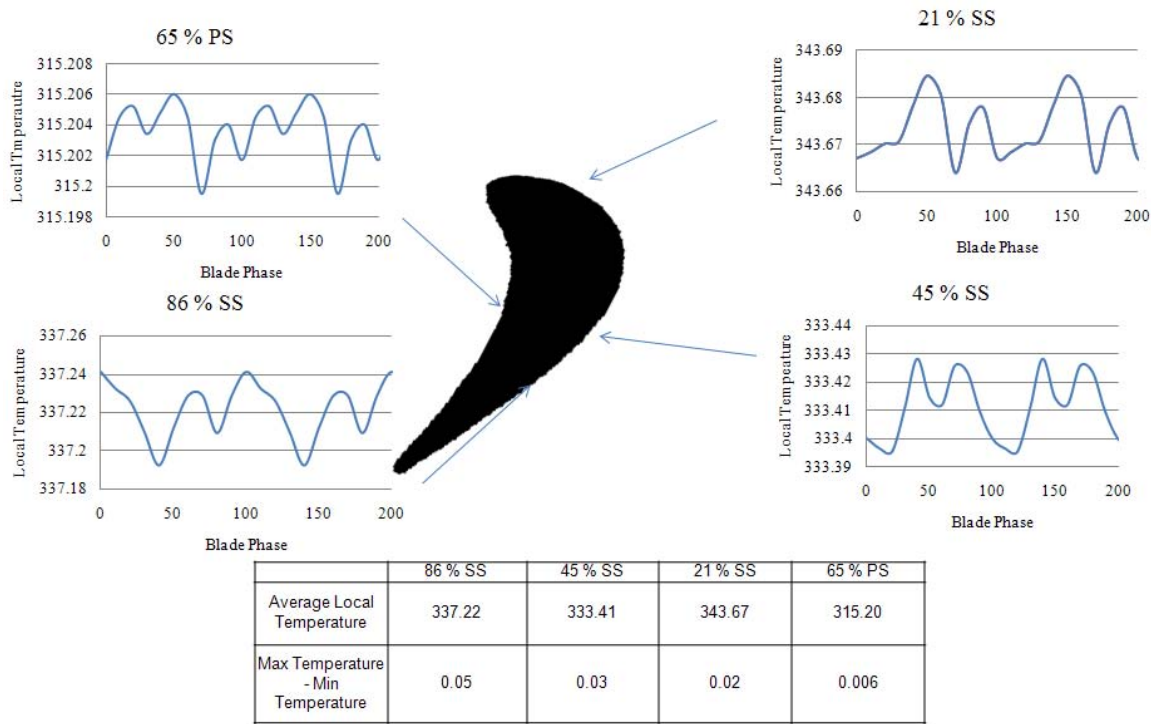


Figure 62: Temperature disturbance (thin-film gauge) along vane, 60 % span, Run 3, 3.5-3.7 sec

Temperatures along the suction side are higher than along the pressure side. This would be expected, as the suction side of the vanes incorporates less cooling, and a higher SS velocity causes higher heat flux coefficients (surface temperatures do not respond to the same phenomena as the pressure, so will not trend in the same way). These surface temperatures are a function of freestream and coolant temperatures, both affected by local velocities. Further analysis of the local flow and cooling schemes must be investigated to gain an appreciation for this temperature distribution; however, this is not of prime concern in the current study. As with the pressure data, results of the vane's

phase-locked temperature disturbances agree with trends expected. Disturbances of $0.05\text{--}0.03\text{ }^{\circ}\text{K}$ are seen at 45 and 86 % SS, between 1.5 and 2.5 times that seen fore of the vane throat, at 21 % SS ($0.02\text{ }^{\circ}\text{K}$). Again, unsteadiness along the pressure side was minimal.

When not phase-locked as above, the temperature disturbance's propagation upstream is seen. This is shown in Figure 63. This same propagation was seen in the studies by Urbassik (2003), but in the pressure disturbances, shown in Figure 4.

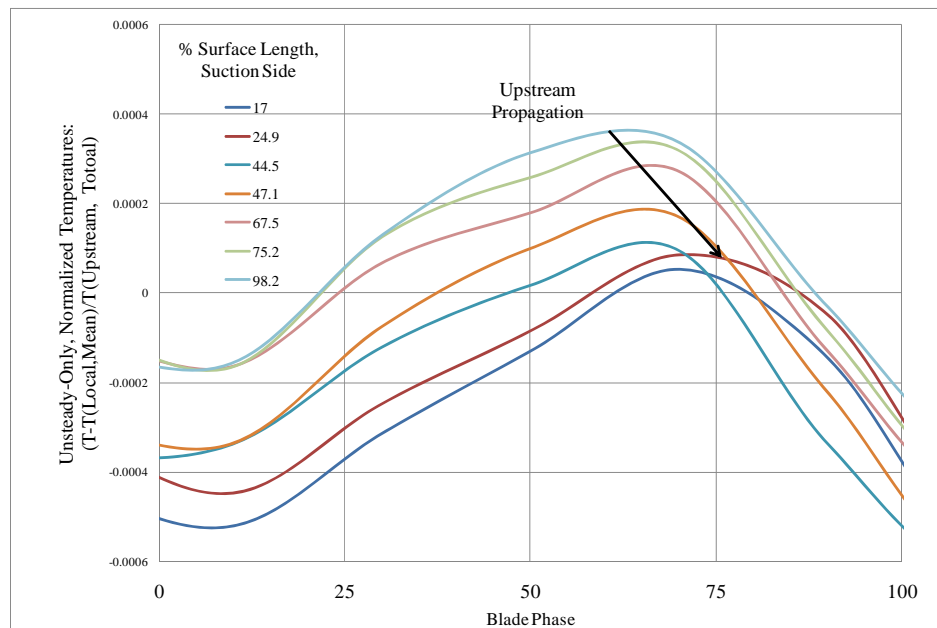


Figure 63: Normalized temperature disturbances along vane suction side, 60 % span

Referring back to Figure 62, it is seen that the suction-side temperature disturbances appear not as a simple rise and fall in temperature (as was the case with pressure disturbances), but resemble a double-humped peak centered on 50 % blade phase. Substantiation of this doubled perturbation is seen in the FFT of the vane's 90 % SS, TE FFT in Figure 40. The exact reasoning for this observance is not fully understood; however, two possible explanations are seen from the phenomenon discussed

within current literature. As mentioned previously, two effects stem from the movement of a downstream rotor: shock reflection; and potential unsteadiness, in the form of inter-stage compression. It is possible that these two events occur at difference phases of the blade's passage, causing two modulations in the temperatures seen by the vane's suction side. Another possible explanation lies within the movement of the reflected shock on the vane's surface. As the shock impinges upon any given location on the vane's surface, a disturbance in temperature will be seen, as the local coolant film will be disrupted. Also, as the shock moves further upstream, it will impinge upon the cooling jet which feeds this film, causing a modulation in the jet itself. The interruption in coolant feed will be then seen as the flow of the coolant film moves along the vane surface, causing a secondary disturbance in the surface temperature. Again, the exact nature, geometry, and velocity of this shock's reflection must be further investigated in order to more fully understand this 'dual-hump' shape.

The results just shown for Run 3 demonstrate that fluctuations do occur in pressures and temperatures along the vane's surface, and begin to demonstrate the nature and behavior of this unsteadiness. It was next desired to find the outcome of this unsteadiness in the form of an 'unsteady envelope'—that is, the range of temperatures and pressures through which a given location would pass. As shown previously, this unsteady envelope was gained by averaging the 58 troughs and 58 peaks from the ensemble-averages of each vane instrumentation location. Results of the unsteady envelope are presented as normalized variations along the surface of a vane (at 60 % Span) are seen in Figure 64 and Figure 65. The difference between the mean high and

mean low was taken as the fluctuation of pressure or temperature, P (Fluctuation) or T (Fluctuation), then normalized by the upstream total pressure.

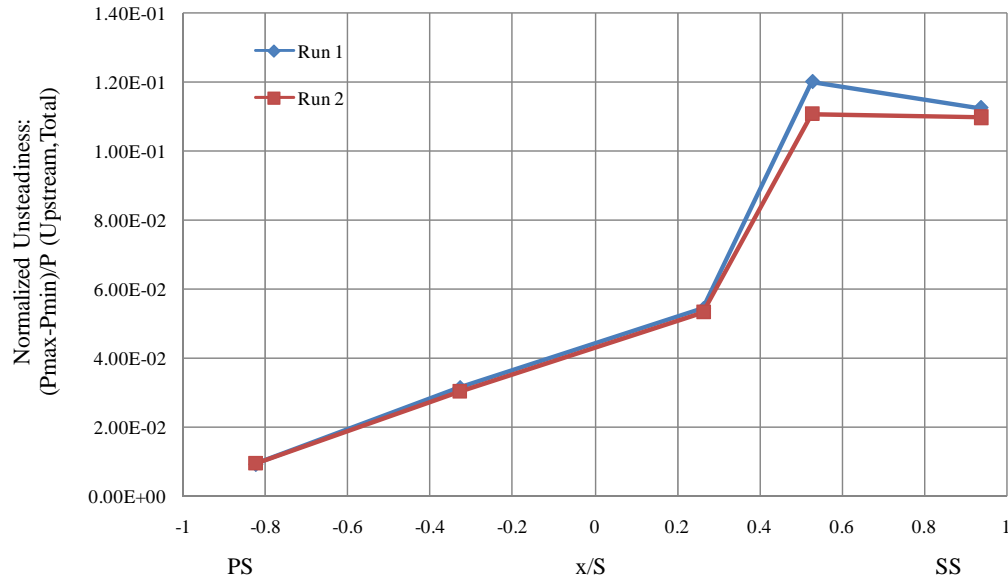


Figure 64: Unsteady pressure variations on vane, 60 % span

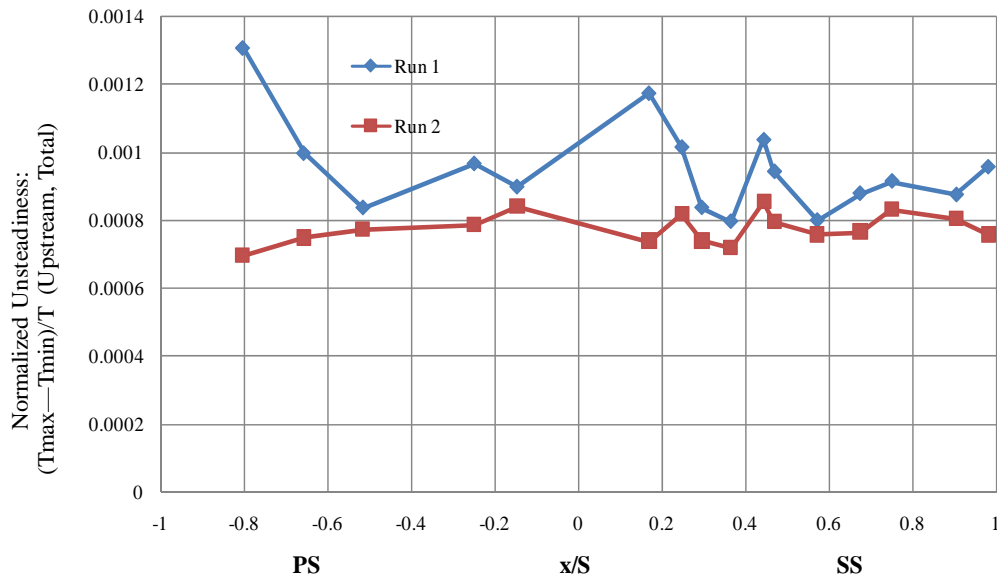


Figure 65: Unsteady temperature variations on vane, 60 % span

As expected, the most marked unsteadiness in pressure is seen toward the trailing edge along the suction side of the vane, totaling between 11 and 12 percent of the total

upstream temperature during Runs 1 and 2. This was five to six times the average unsteadiness seen along the pressure side. However, the same trend was not seen in temperature along the surfaces of the vane: the pressure side and suction side both experienced fluctuations between 0.08 and 0.1 % of the total upstream temperature (in contrast to the values seen earlier in Figure 65: Unsteady temperature variations on vane, 60 % span. The fact that unsteadiness in temperature did not distinctly rise along the TE, SS of the vane suggests that the film coolant is highly effective in guarding against rotor-induced temperature oscillations. This also is a manifestation of the difference in the nature of the temperature and pressure disturbances: while pressure disturbances propagate back upstream and pass very quickly, temperature disturbances lag in their convection through their medium.

To gain a further appreciation for the meaning and consequences of this variation, heat flux variations were taken for Runs 1 through 3 at two points along the vane—both at 45 % SS and 80 % PS. These results are seen in Table 5, with unsteadiness normalized by the average heat flux at each point. Larger variations were seen along the suction side (133.8 % and 182.8 % fluctuations) versus the pressure side (55 and 39.6 % fluctuations). Because unsteadiness in surface temperature is not more pronounced on the TE, SS, it must be assumed that the greater fluctuations in heat flux are due to more than simply variations in surface temperature. To understand this, further research on the shock reflection and rotor-stator interaction in a film-cooled environment must take place.

Table 5: Heat flux variation at 60 % span

		80 % PS	45.5 % SS
<u>Run 1</u>	<i>Average</i>	18088.4	33353.8
	<i>High</i>	23190.3	56358.6
	<i>Low</i>	13248.6	11740.2
	<i>Fluctuation</i>	9941.8	44618.4
	<i>% Fluctuation</i>	55.0	133.8
<u>Run 2</u>	<i>Average</i>	25369.3	N/A
	<i>High</i>	30800.9	N/A
	<i>Low</i>	20763.7	N/A
	<i>Fluctuation</i>	10037.2	N/A
	<i>% Fluctuation</i>	39.6	N/A
<u>Run 3</u>	<i>Average</i>	N/A	17515.3
	<i>High</i>	N/A	34746.9
	<i>Low</i>	N/A	2723.3
	<i>Fluctuation</i>	N/A	32023.7
	<i>% Fluctuation</i>	N/A	182.8

5.2 Time-Averaged Results & Film Cooling Parameters

Time-averaged results were processed as previously described, with results processed from the data in the 3.5-4.5 second window, representing what is recognized as a thermally steady state. Data is presented for Runs A-J. In each graph, calculated data points are represented by markers at each point, with lines connecting the points between.

Mean heat fluxes were calculated across the same 3.5-4.5 second ‘steady-state’ window, as shown in Figure 66 for 60 % span across the surface length vanes with a cooling scheme comprised of compound shaped holes. Run J had the lowest coolant-to-freestream pressure ratios in both the inner and outer diameters, corresponding to a lower blowing ratio. This run generally exhibited the highest mean heat fluxes, as would be expected with less coolant flow along the vane surface.

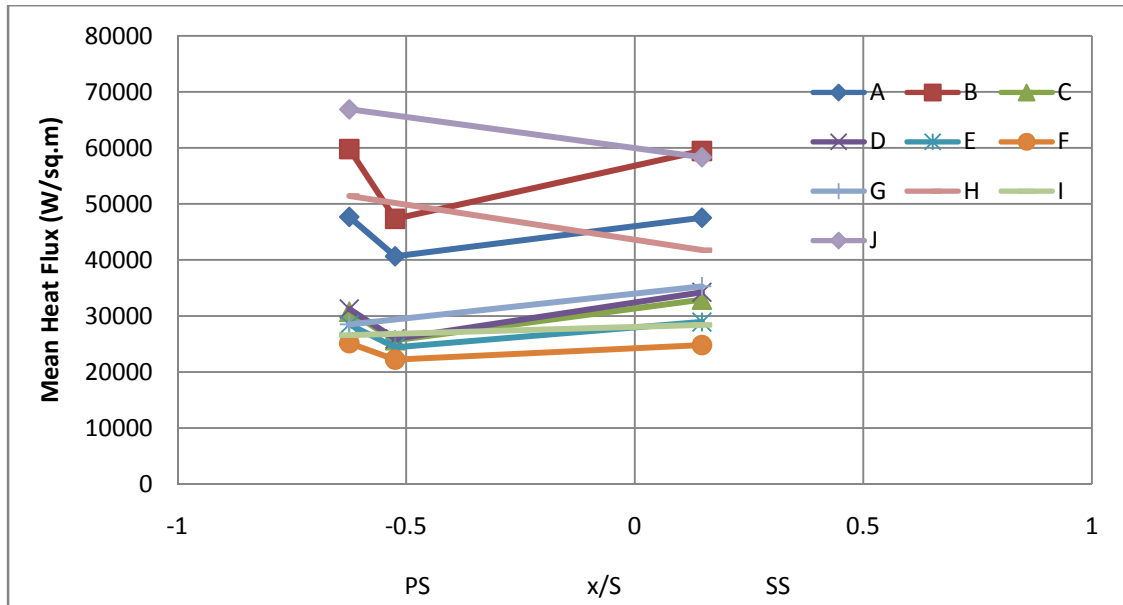


Figure 66: Mean heat flux across vane surface, 60 % span

In calculating the adiabatic film-cooling effectiveness and film-cooled heat transfer coefficient (h_f and η), Popp-style plots were produced to probe and validate the usage of this method, as seen in Figure 67 and Figure 68. Shown within these plots are four points representative of the 3.5-4.5 second window, as well as the line extrapolated from all X, Y pairs within this time window (a total of 2,000 data points, taken at the sampling frequency of 2 kHz). Presented after this are the four X, Y pairs, in Table 6. Chosen for this were the vane-mounted gauges at 14 % SS and 62 % PS.

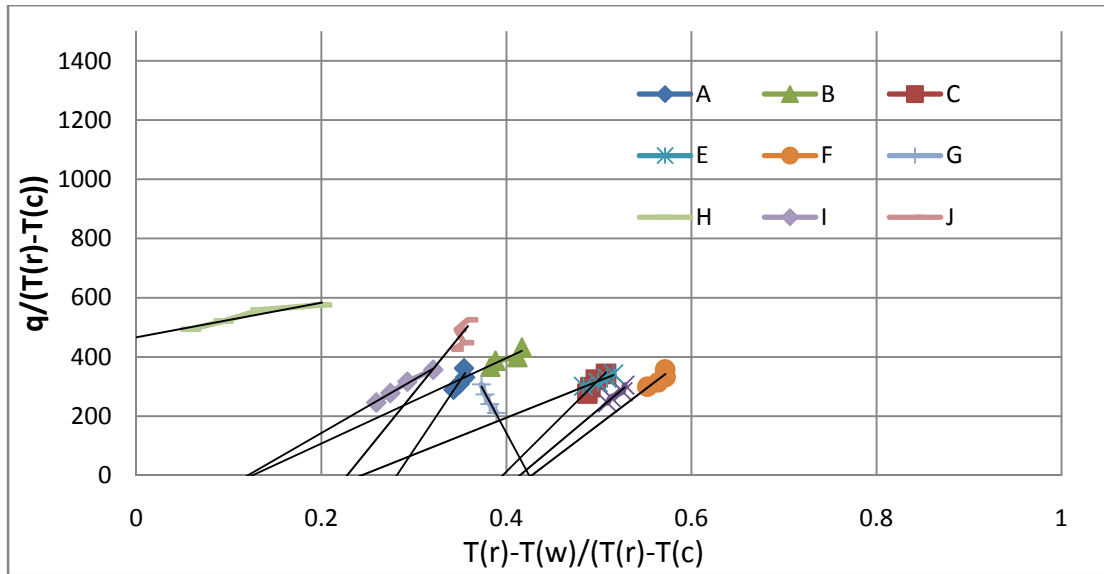


Figure 67: Popp-style plot for 14 % SS vane gauge, 60 % span

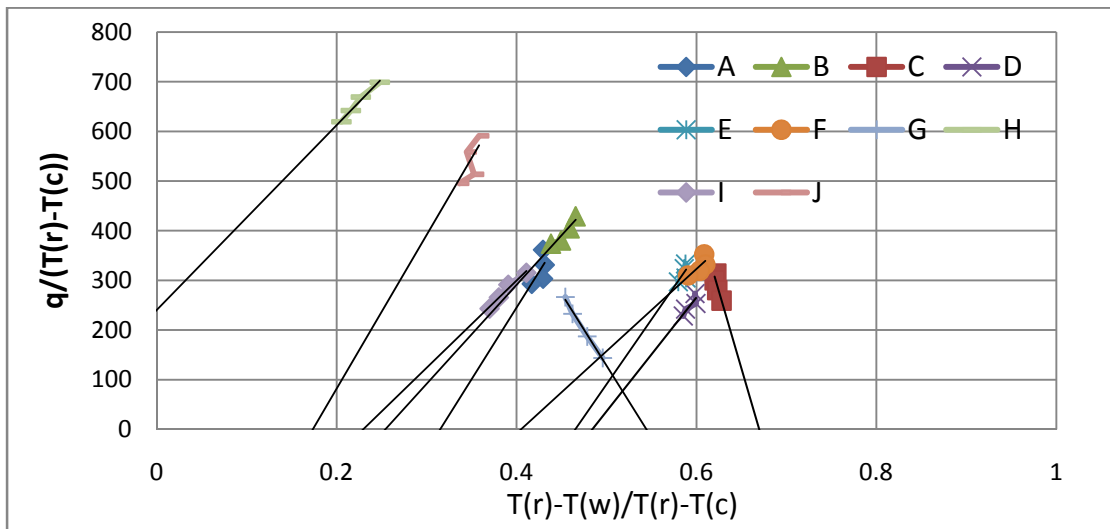


Figure 68: Popp-style plot for 62 % PS vane gauge, 60 % span

Table 6: X, Y pairs for Popp plotting

62 % PS				14 % SS			
Run	Time	x	y	Run	Time	x	y
A	3.5-3.75	0.43	361.35	A	3.5-3.75	0.35	362.01
	3.75-4.0	0.43	330.99		3.75-4.0	0.36	331.44
	4.0-4.25	0.43	303.05		4.0-4.25	0.35	309.12
	4.25-4.5	0.42	292.77		4.25-4.5	0.34	289.53
B	3.5-3.75	0.47	429.19	B	3.5-3.75	0.42	431.57
	3.75-4.0	0.46	404.78		3.75-4.0	0.41	399.65
	4.0-4.25	0.45	380.34		4.0-4.25	0.39	387.36
	4.25-4.5	0.44	373.87		4.25-4.5	0.38	367.25
C	3.5-3.75	0.62	313.61	C	3.5-3.75	0.51	342.90
	3.75-4.0	0.62	300.04		3.75-4.0	0.50	323.77
	4.0-4.25	0.62	280.21		4.0-4.25	0.49	298.16
	4.25-4.5	0.63	258.97		4.25-4.5	0.49	276.73
D	3.5-3.75	0.60	273.26	D	3.5-3.75	0.53	304.96
	3.75-4.0	0.60	253.34		3.75-4.0	0.53	282.50
	4.0-4.25	0.59	241.97		4.0-4.25	0.51	264.09
	4.25-4.5	0.59	228.22		4.25-4.5	0.51	245.00
E	3.5-3.75	0.59	333.15	E	3.5-3.75	0.52	342.83
	3.75-4.0	0.59	323.65		3.75-4.0	0.51	328.55
	4.0-4.25	0.59	304.81		4.0-4.25	0.50	314.00
	4.25-4.5	0.58	296.99		4.25-4.5	0.48	301.35
F	3.5-3.75	0.61	352.35	F	3.5-3.75	0.57	358.22
	3.75-4.0	0.61	331.75		3.75-4.0	0.57	332.18
	4.0-4.25	0.60	318.98		4.0-4.25	0.56	314.18
	4.25-4.5	0.59	309.85		4.25-4.5	0.55	299.60
G	3.5-3.75	0.45	266.33	G	3.5-3.75	0.37	307.25
	3.75-4.0	0.46	232.50		3.75-4.0	0.38	273.37
	4.0-4.25	0.48	186.97		4.0-4.25	0.38	240.92
	4.25-4.5	0.50	143.64		4.25-4.5	0.39	211.08
H	3.5-3.75	0.25	698.89	H	3.5-3.75	0.20	575.86
	3.75-4.0	0.23	669.23		3.75-4.0	0.13	559.19
	4.0-4.25	0.22	641.98		4.0-4.25	0.09	521.64
	4.25-4.5	0.21	619.55		4.25-4.5	0.06	493.96
I	3.5-3.75	0.41	315.16	I	3.5-3.75	0.32	357.44
	3.75-4.0	0.39	291.11		3.75-4.0	0.29	316.73
	4.0-4.25	0.38	265.59		4.0-4.25	0.27	278.51
	4.25-4.5	0.37	243.06		4.25-4.5	0.26	246.41
J	3.5-3.75	0.36	591.08	J	3.5-3.75	0.36	525.57
	3.75-4.0	0.34	558.59		3.75-4.0	0.35	491.92
	4.0-4.25	0.35	513.54		4.0-4.25	0.35	448.15
	4.25-4.5	0.34	495.30		4.25-4.5	0.34	426.14

Variations in adiabatic film-cooling effectiveness and heat flux coefficient (the X-intercepts and slopes of the extrapolated lines, respectively) were seen. These variations were observed when the Popp method was employed in determining cooling parameters from data collected from TRF testing of this vane-only section (Polanka et al., 2008: 11). Deviations and differences should be expected, as the parameters h_f and η are dependent upon conditions which varied throughout Runs A-J; however, several trials exhibit anomalies that merit further investigation: Firstly, Run H shows the extrapolation of a negative η for both the 62 % PS and 14 % SS gauges. Secondly, Run G shows a negative h_f for both gauge locations, and Run C shows a negative h_f for the 62 % PS gauge.

In attempting to understand the reasoning for these problematic results, the original data from which the Popp-style plots are generated was gathered. This data (temperatures and heat fluxes within the four time periods between 3.5 and 4.5 seconds) is presented in Table 7. This is presented for Runs B, G, and H. Run B exhibits behavior that produced rational results. In examining the temperatures of the underlying metal (T_m), as shown in Table 7, it is observed that T_m during Run B varies by 0.4 and 0.5 ° K for the two locations; however, Runs G and H exhibit variations in T_m between 2.0 and 6.2 ° K. Runs A, B, D, E, F, I, and J exhibit metal temperature variations of less than 1.0 ° K. This large variation is evident of a film-cooled location that has not yet reached a thermally-steady state. While it was expected that the airfoils would have reached a thermally-steady state by 3.5 seconds, this is not apparently the case for Runs G and H at the given locations, and for Run C along the pressure side. The realization of thermal steadiness, as discussed before, is dependent upon the normalization of flow across the airfoil surface followed by an adjustment of the underlying metal surface's temperature,

resulting in a stable state of convective heat transfer on the surface, and conductive heat transfer through the metallic wall. Thermal stability is also a function of location, as driving temperatures and wall thickness vary along the airfoil surface.

Table 7: Values for Popp plotting

62 % PS								
Run	Time	Tr	Tw	Tc	Tm	Tr-Tw	Tr-Tc	q
B	3.5-3.75	434.6	362.4	269.5	321.6	72.2	165.1	66557.4
	3.75-4.0	431.2	360.5	267.1	321.4	70.7	164.0	62351.4
	4.0-4.25	422.7	356.4	265.2	321.2	66.3	91.2	56103.1
	4.25-4.5	418.6	355.0	263.5	321.1	63.6	91.5	54265.5
G	3.5-3.75	391.2	328.3	242.8	300.4	62.9	85.6	36874.7
	3.75-4.0	388.8	324.7	240.1	299.4	64.1	84.6	32245.2
	4.0-4.25	384.7	319.4	238.1	298.2	65.4	81.2	25541.7
	4.25-4.5	380.9	314.1	236.1	297.1	66.8	78.0	19367.9
H	3.5-3.75	371.9	352.2	292.3	321.1	19.7	79.6	55627.1
	3.75-4.0	369.6	351.8	291.2	321.8	17.8	78.4	52487.8
	4.0-4.25	368.3	351.5	290.5	322.6	16.8	77.8	49964.9
	4.25-4.5	366.7	350.9	289.8	323.1	15.8	76.8	47598.4

14 % SS								
Run	Time	Tr	Tw	Tc	Tm	Tr-Tw	Tr-Tc	q
B	3.5-3.75	433.9	369.6	269.5	329.2	64.4	100.1	66637.2
	3.75-4.0	430.5	367.4	267.1	329.5	63.2	100.2	61294.9
	4.0-4.25	422.0	365.0	265.2	329.6	57.0	99.8	56887.6
	4.25-4.5	418.0	362.7	263.5	329.6	55.3	99.2	53067.8
G	3.5-3.75	390.6	339.2	242.8	312.2	51.4	96.4	42357.9
	3.75-4.0	388.2	336.2	240.1	311.6	52.0	96.1	37752.5
	4.0-4.25	384.1	332.2	238.1	310.7	51.9	94.1	32772.1
	4.25-4.5	380.3	328.1	236.1	309.9	52.3	92.0	28340.2
H	3.5-3.75	371.3	355.5	292.3	332.6	15.9	79.0	45513.7
	3.75-4.0	369.1	358.6	291.2	335.1	10.5	77.9	43547.7
	4.0-4.25	367.8	360.5	290.5	337.0	7.3	77.3	40311.2
	4.25-4.5	366.1	361.6	289.8	338.8	4.5	76.3	37679.7

It was determined for this data reduction that metal temperatures varying by more than 1.0 ° K were evident of a test in which conditions made a thermally steady state unachievable for the test apparatus by the 3.5-second point. These test points were not used in calculating the adiabatic effectiveness and heat transfer coefficient for the vanes.

The tests remaining (Runs A, B, D, E, F, I, and J) are presented again in Figure 69 for the 60 % span, 62 % PS gauge. Variations in η are outlined, and variations in h_f are seen in the changing slopes of the extrapolated lines. The outcomes of these results are seen in Figure 70 and Figure 71 for the vane-mounted gauges. Results processed from data collected from the vane-only test section of this apparatus (Polanka et al., 2008) are plotted alongside. These points represent average values from ten tests run at similar conditions to the full-stage program, but only with the vane section of the test apparatus. Values of heat flux coefficient and adiabatic effectiveness for the vane in this full stage testing fall within reasonable agreement with those seen from the vane-only test section.

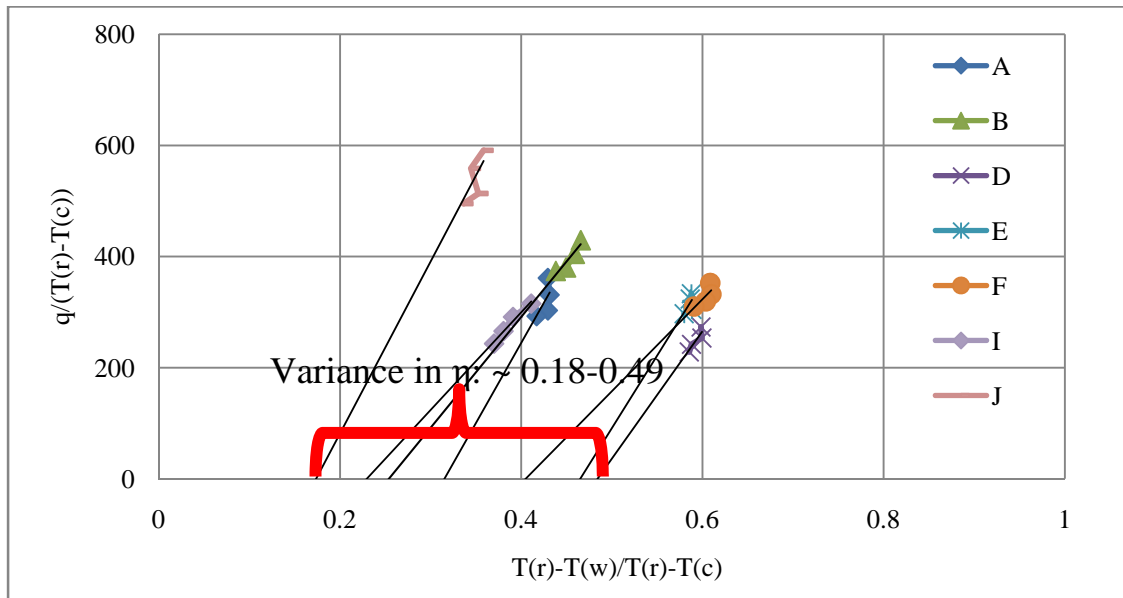


Figure 69: Popp-style plot for vane: 60 % span, 62 % PS

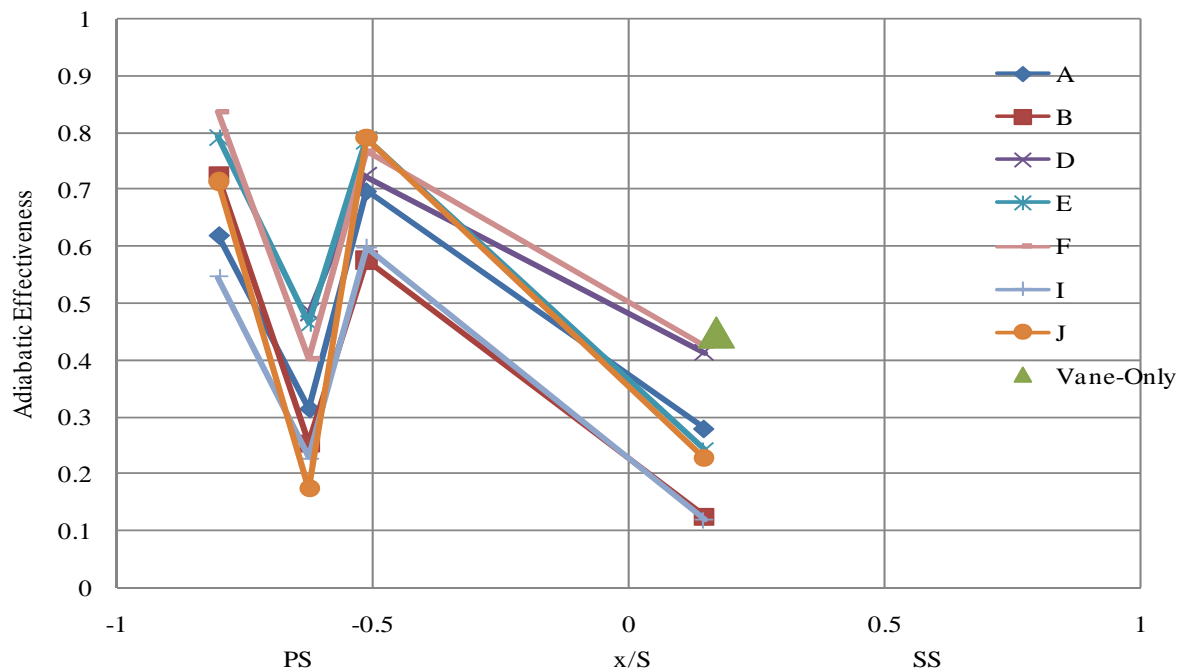


Figure 70: Adiabatic film-cooled effectiveness along vane surface, 60 % span

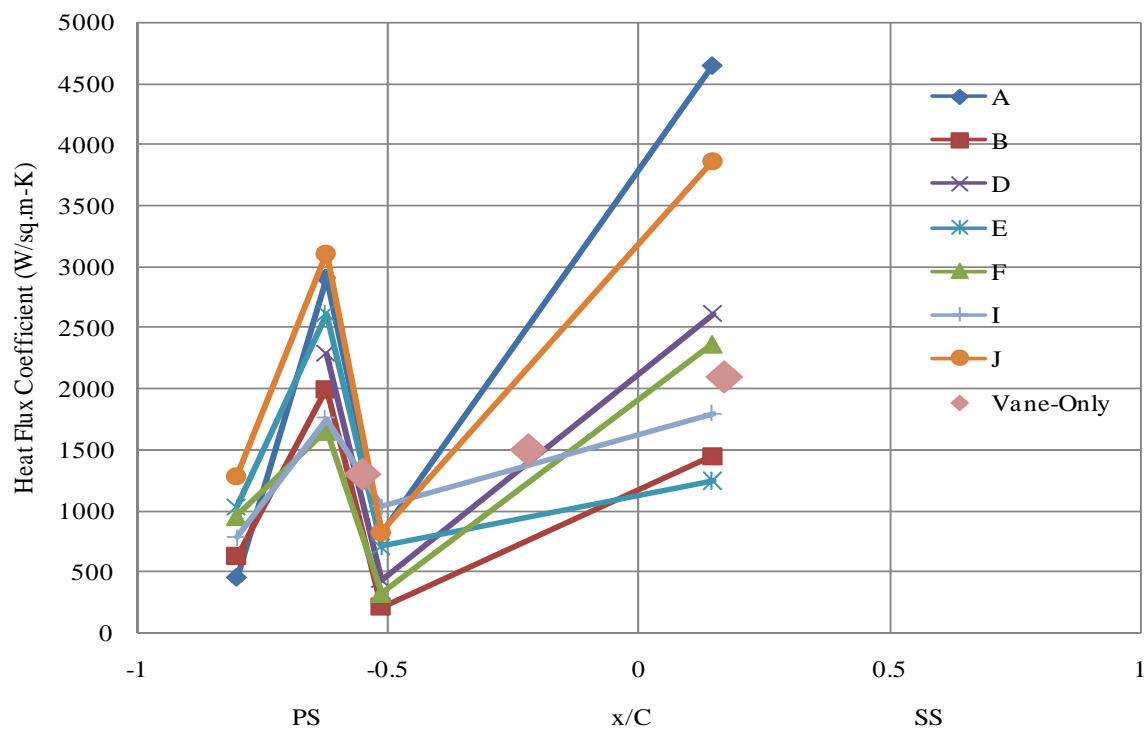


Figure 71: Heat flux coefficient along vane surface, 60 % span

At 51 % PS, a spike in adiabatic effectiveness with a corresponding drop in heat flux coefficient. The heat flux coefficient drop with rising adiabatic effectiveness (also seen at approximately 80 % PS) is not concurrent with literature on the topic (rather, the opposite correlation is usually prevalent). While definite conclusions regarding this behavior cannot be drawn, it must be remembered that both h_f and η are calculated from extrapolations of closely-grouped data points, and the Popp method must be interpreted with an understanding of uncertainty. Further analysis of these results and additional vane locations (Polanka et al., 2008) must be performed in order to fully understand whether these data points may or may not be useful. Also, these are marked shifts in values are from those seen near the leading edge on the suction side. Because of the presence of a showerhead configuration of holes near the vane LE, it would be expected that adiabatic effectiveness would be higher close to the LE rows of holes. Again, data from the Popp method must be confirmed as of use. Furthermore, it must be realized that these two locations are feed from different coolant holes. Therefore, blowing ratios and temperature ratios of the coolant, which differ between the OD and ID feeds (that is, for the TE and LE gauge locations, respectively), may result in the trends seen in the heat flux coefficients and adiabatic effectiveness. Also, this result must be understood with respect to the location of the coolant ejection jets along the entire surface. Because of the oddity of these results, these values are questionable.

Overall effectiveness was calculated along the span of two vanes, both with like cooling schemes—the compound, shaped holes. The overall effectiveness at 60 % span is seen in Figure 72 and Figure 73, and at 90 % span as seen in Figure 74 . Overall effectiveness, as calculated for this test vane ring (Umholtz, 2007: 41), is plotted at 60 %

span, as well. These points represent an average of the data collected during four tests conducted at similar test conditions to the current (vane and rotor) test section. In comparing the overall effectiveness values of the vane-only test section to those of the full stage, approximate values generally agree. A demarcation distinct enough to draw any definite conclusions from this comparison is not seen, but a drop in the overall effectiveness along the trailing edge of the suction side of the vane would be expected with the addition of the rotor stage downstream. Nominally lower values are seen along the TE, SS of the vane in full-stage testing. A further comparison of tests must be conducted in order to more fully understand the effect that a downstream rotor stage has on the parameter of overall effectiveness along a vane surface.

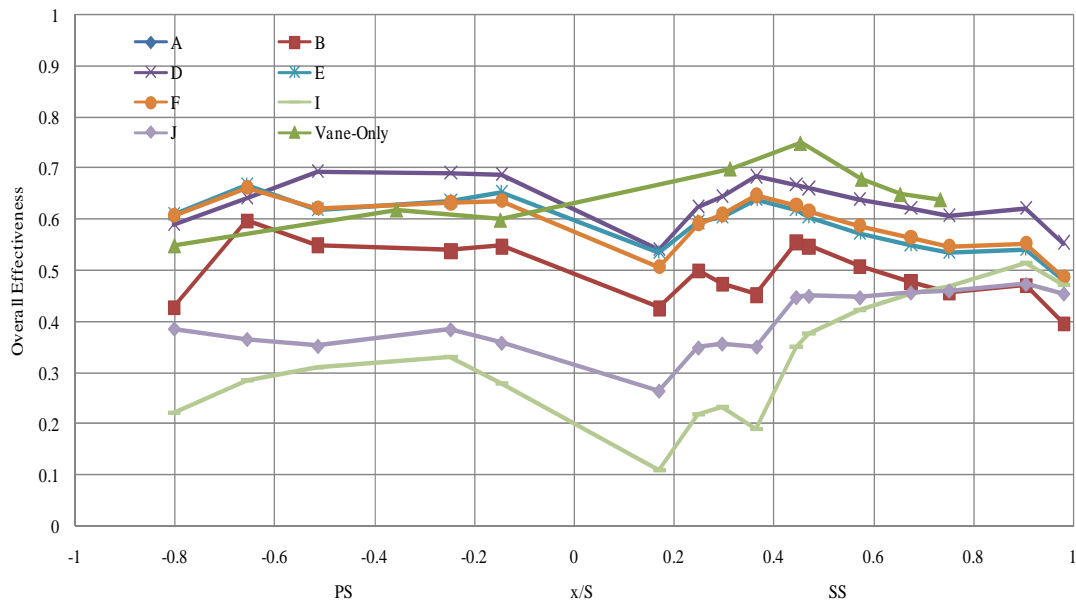


Figure 72: Compound shaped holes, overall effectiveness, 60 % span

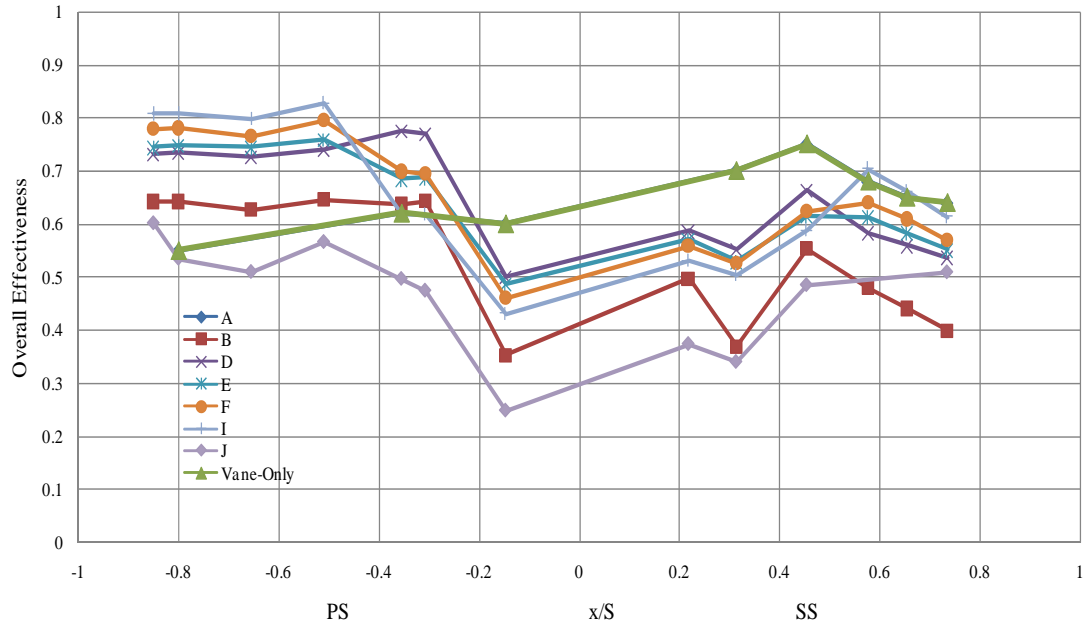


Figure 73: Compound shaped holes (second airfoil), overall effectiveness, 60 % span

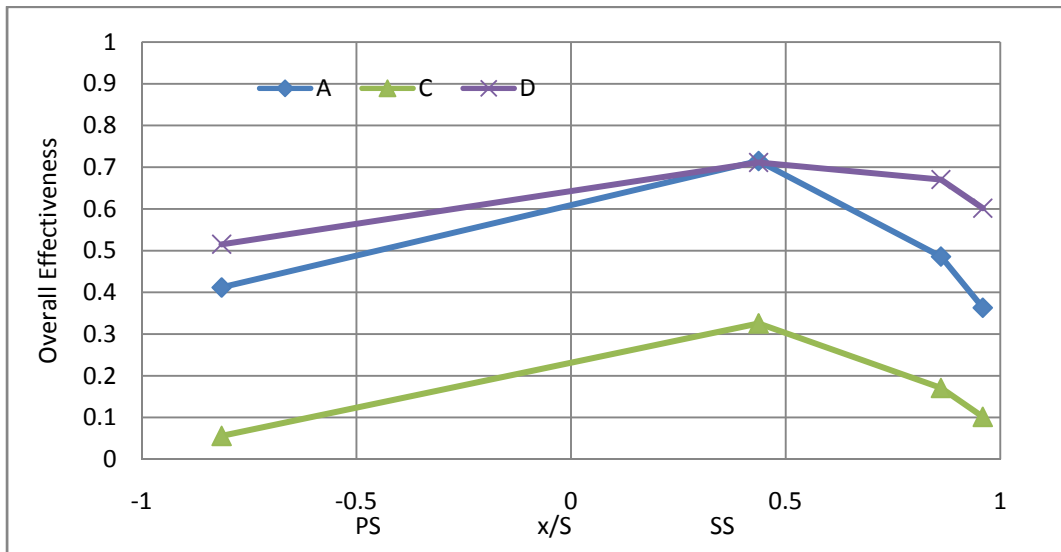


Figure 74: Compound shaped holes, overall effectiveness, 90 % Span

6. Results and Analysis—BOAS

Results from data from BOAS-mounted gauges were processed in two sections, as well: time-resolved and time-averaged. As with the vane stage, time-resolved results and analysis are presented first, followed by time-averaged results.

6.1 Time-Resolved Results

In attempting to understand the results from a single blade tip passage along the BOAS, a standard shape of pressure and temperature disturbances was gathered as described previously for the vane stage: Ensemble-averaged data was taken during the first 12 revolutions during the thermally steady window of 3.5-3.7 seconds for Run 3. Phase-locked data was taken from the average of all 58 blade tips. . Tip cooling schemes varied, and tip clearances varied by approximately 0.2 millimeters; however, the use of all 58 blades in this data reduction allows one to obtain the results of a typical blade pass phenomenon. Tip cooling was ejected through approximately the first 31 % of the axial chord of the rotor blade tips. Also of importance is the usage of the term ‘phase-locked’ for the shroud-mounted gauges. For each BOAS gauge, 50 % blade phase corresponds to the passage of the mean-camber line of the airfoil tip itself. Therefore, pressure and suction side passages (corresponding to the trough and peaks of the cyclic shapes, respectively) appear as centered about 50 % blade phase. The results for phase-locked temperature and pressure disturbances are seen in Figure 75 and Figure 76, with values tabulated below the figures. As would be expected, average static pressure decays with movement downstream, as enthalpy is extracted from the working fluid with movement

through the rotor stage. Largest disturbances were seen at 65 % axial chord (x/C), and smallest at 8 % axial chord.

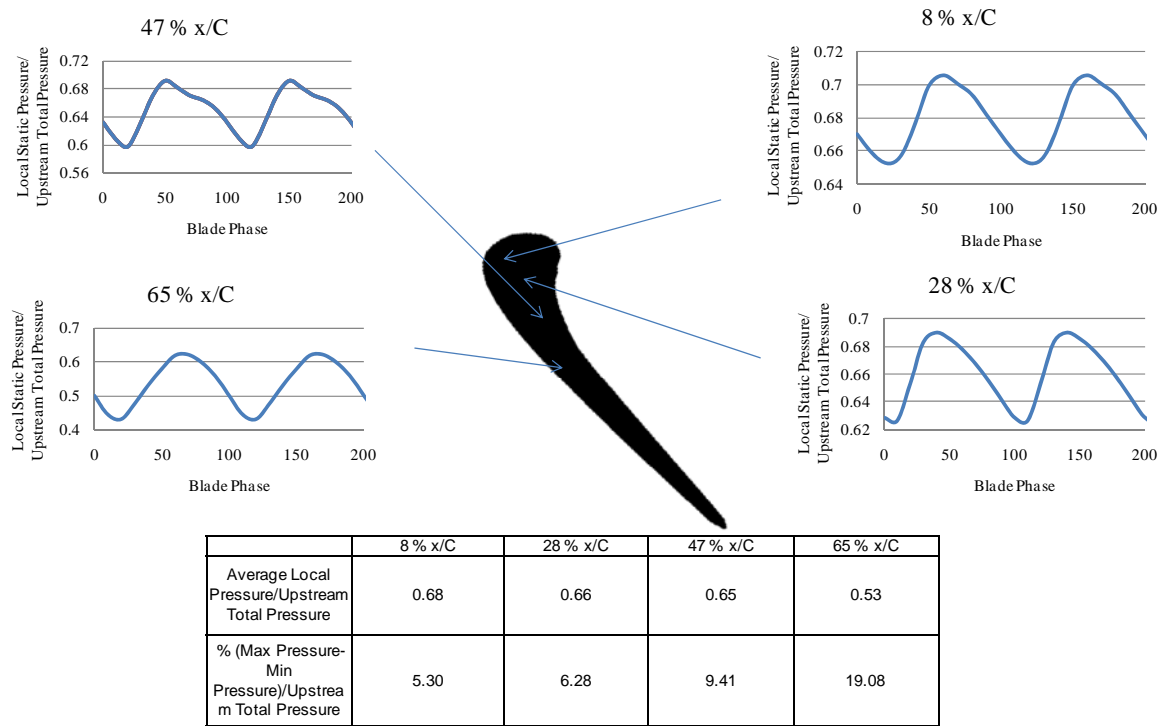


Figure 75: Pressure disturbances along BOAS, Run 3, 3.5-3.7 sec

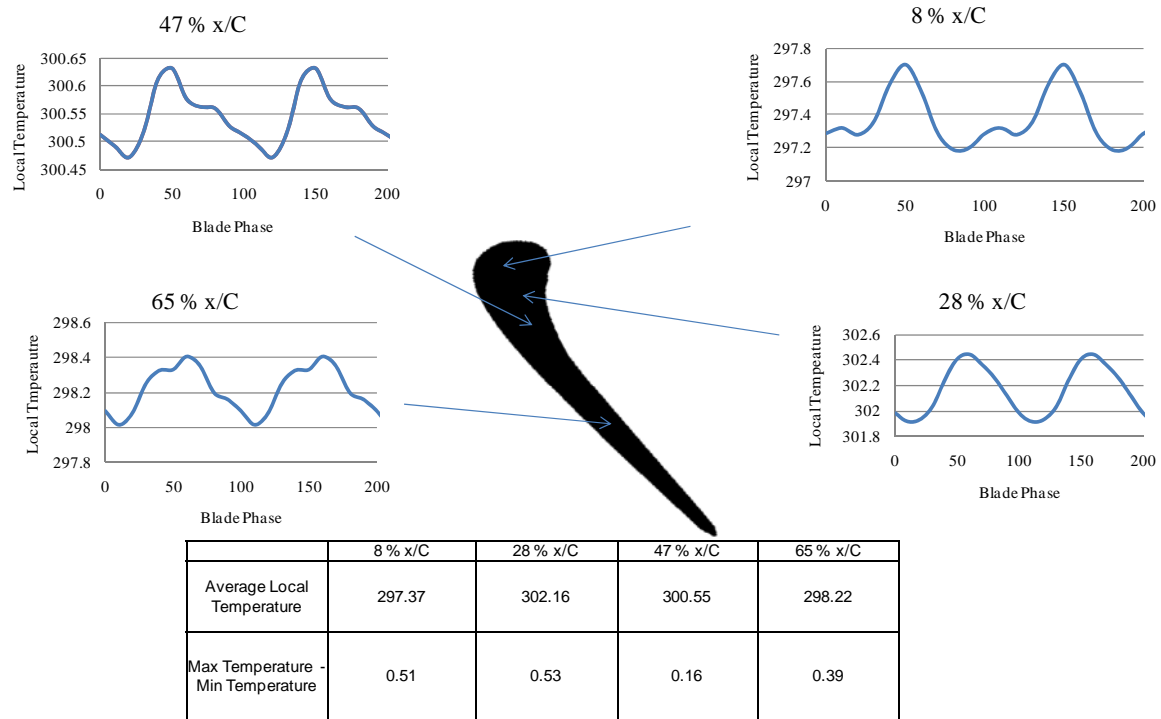


Figure 76: Temperature disturbances along BOAS, Run 3, 3.5-3.7 sec

In contrast to the pressure disturbances, highest temperature disturbances were seen at 8 % and 28 % axial chord. This would be expected, as tip cooling was ejected along these locations. It may be explained by considering the combined effects of high freestream massflows with the coolant flow: As the coolant flow is ejected, its path may be turned downstream quite rapidly by the high-speed mainstream flow, causing its flow to reach the shroud walls further downstream. Further investigation must take place in order to confirm this. It also can be seen that the temperature disturbances see a dip in their cyclic shapes at the 8, 47, and 65 % axial chord location. The pressure disturbances do not see this shape, evidence that these mid-passage dips are results of the tip coolant impinging upon the surface of the shroud at these points.

It was also desired to see the effect of the different tip-cooling methods employed in the rotor stage of the test section. To do this, two to three consecutive like blade passage events were averaged together with the ‘phase-locking’ techniques to gain a typical blade passage event of that blade tip type in particular. This is seen in Figure 77. Definite deviations from a purely cyclical shape are seen in both the flat tip (with coolant ejection ports on a flat tip of the blade’s end) and squealer (with tip depressions for coolant ejection) type coolant schemes. More research can delve into the effectiveness of individual schemes.

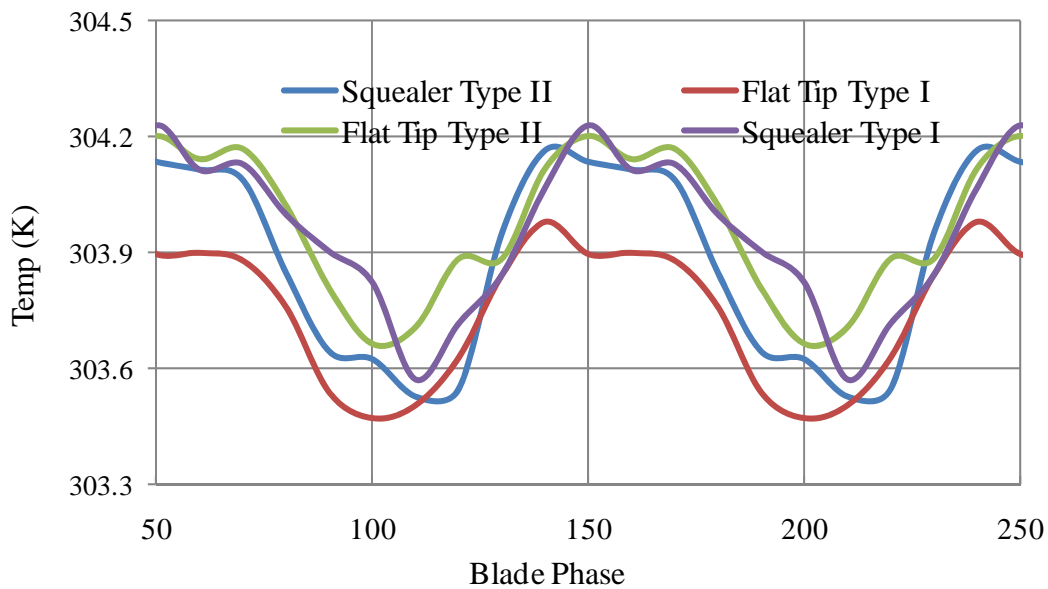


Figure 77: Comparison of tip cooling schemes, 28 % axial chord

As with time-resolved results along the vane, an ‘unsteady envelope’ of pressure and temperature variations was calculated from the average high and average low values (peaks and troughs) of the ensemble-averaged data for each BOAS-mounted gauge. Pressure disturbances are normalized by upstream total pressures, and temperature disturbances are shown as raw fluctuations. This is shown for the BOAS in Figure 78

and Figure 79 for Runs 1 and 2. Results from the uncooled apparatus (Clark et al., 2000) are shown with the pressure disturbances for a baseline of comparison, and see general agreement. Again, largest pressure disturbances were seen along the latter portion of the blade tip's axial chord. Run 1 saw considerably larger variations in temperature (common to the vane results for unsteadiness in temperature), evidence of the higher Reynolds number during this trial.

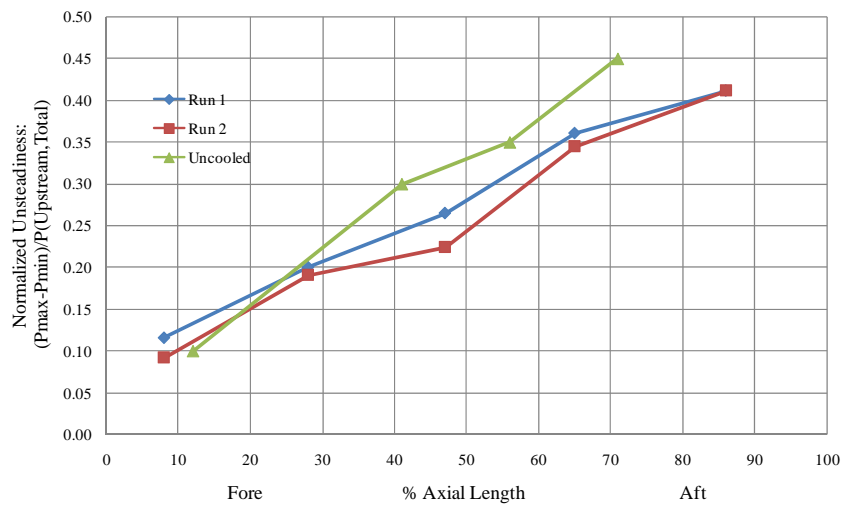


Figure 78: Unsteady pressure variations on BOAS

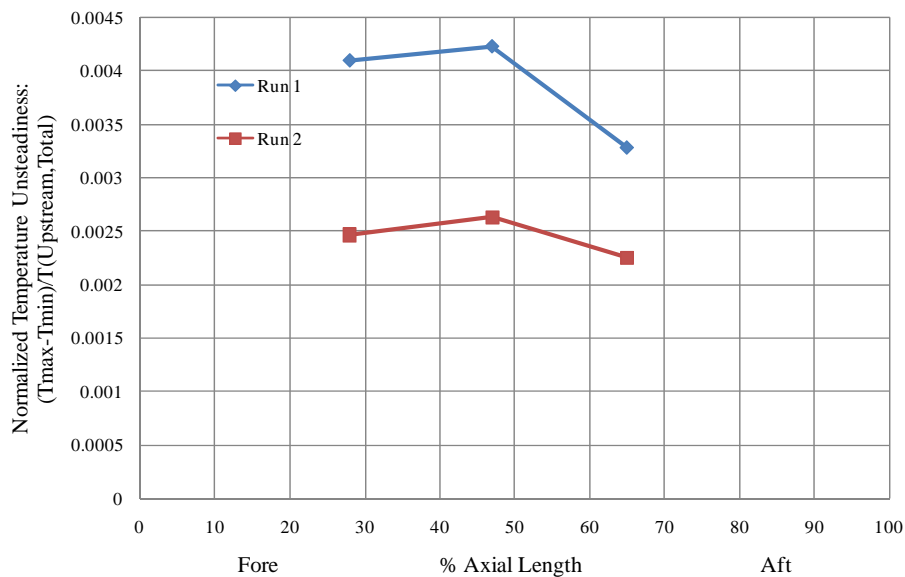


Figure 79: Unsteady temperature variations on BOAS

6.2 Time-Averaged Results

Time-averaged results for the BOAS are presented for the 3.5-4.5 second thermally-steady window of the experimental trials. Runs B and F-J were recognized as having reached a thermally steady state by this time. Because of the very small coolant massflow along the rotor shroud, it has been proposed that driving temperatures along the BOAS surface are not influenced greatly by coolant flow. It was thus desired to attempt to calculate the heat flux coefficient along the BOAS through extrapolation of the convective heat transfer equations for an uncooled case. The result of this is shown in for the 47 % axial chord BOAS Gauge in Figure 80. The calculated heat flux coefficients are shown in Figure 81. Looking at Figure 80 raises some valid and useful points of discussion. It should be noted that, for Runs I and G, time-averaged heat flux actually becomes negative. These negative values are evidence of the decay in temperature through the rotor stage actually bringing average driving recovery temperatures below the metallic temperature, forcing negative heat flux at this wall location. The presence of negative heat flux was observed previously in the uncooled testing of this test section. It shows the need to account for enthalpy extraction in the rotor section and recovery temperature calculation in choosing operating parameters in blowdown tests such as at TRF.

Two observations of the results are of use in looking at the effect of tip cooling on the shroud: In an uncooled experiment on the BOAS (Polanka et al., 2002), generally higher Nusselt numbers and mean heat fluxes were observed on the forward portion of the shroud's axial chord; in cooled experimentation, higher heat flux coefficients were seen along the aft portion of the airfoil during Runs F, G, and H, and were nearly flat for

Runs B, I, and J. Because of the complex flowfield at this location, the exact fallout of tip cooling on heat flux coefficients cannot be readily seen with these data points alone. The high variability in the slopes (h) found for the BOAS also direct attention at the accuracy of the usage of this curve-fitting method for finding the heat flux coefficients and adiabatic effectiveness: with such close groupings of data points within the short test window, it becomes difficult to verify the precision of the curve fit. Therefore, this data must be read with a certain degree of uncertainty assumed.

Despite the fact that that BOAS is not recognized as a coolant-affected area, overall effectiveness was still calculated along the rotor shroud, shown in Figure 82 (0 % axial chord corresponds to the blade LE, and 100 % to the TE). It is noticed that a generally flat shape is observed along the entire chord of the BOAS: no marked rise in overall effectiveness is seen in the locations where coolant was ejected (approximately 5 to 31 % axial chord). This is support for the supposition that BOAS temperatures were not primarily coolant driven.

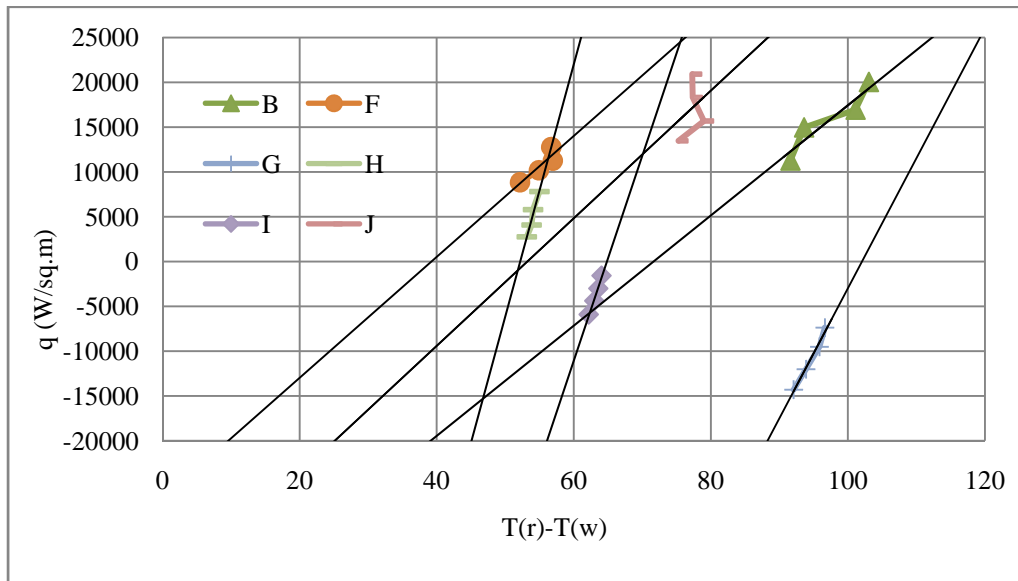


Figure 80: Popp-style uncooled plot for BOAS

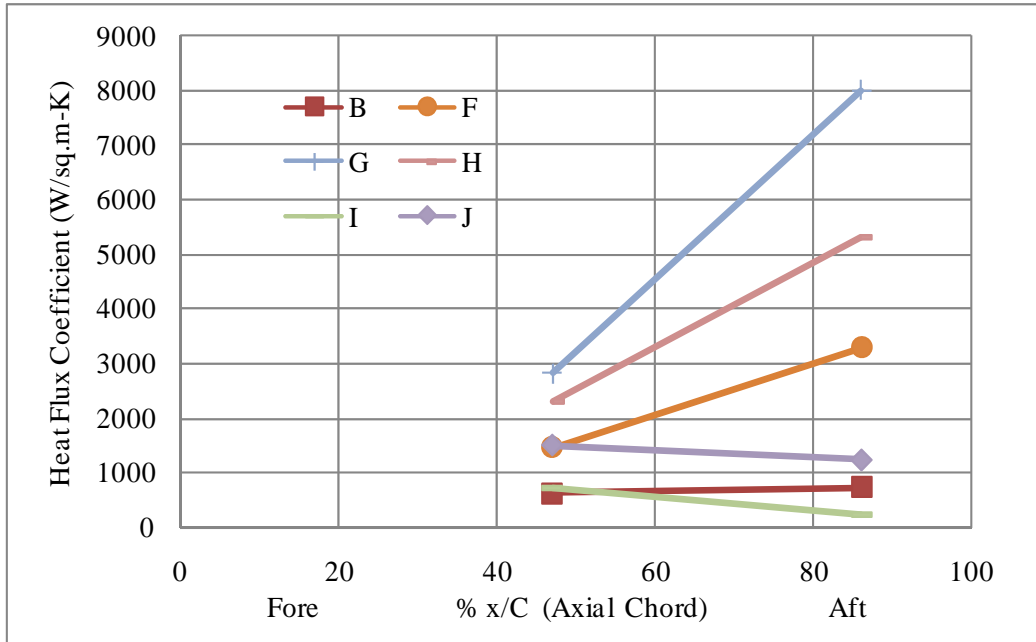


Figure 81: Heat flux coefficients along BOAS

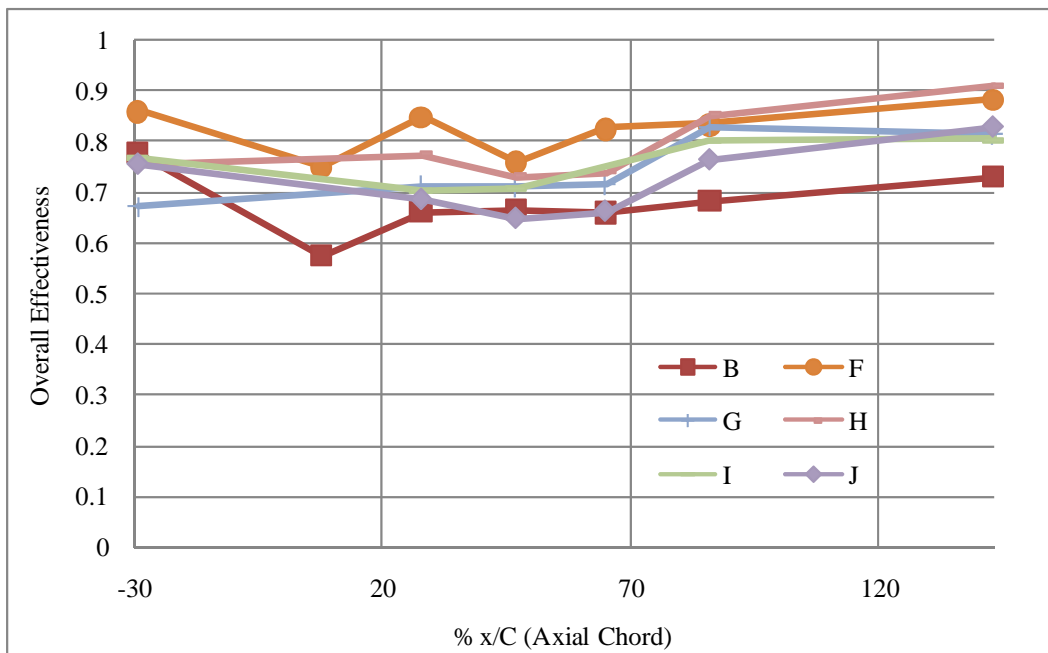


Figure 82: Overall effectiveness along BOAS

7. Conclusions and Recommendations

7.1 Research Conclusions

Current testing has allowed for the first reduction and analysis of a set of data taken within a high-speed, full-scale, fully-cooled turbine vane and rotor stage representative of a modern gas turbine engine. Data collection of temperatures, pressures, and heat fluxes allowed probing of the phenomenon of rotor-induced unsteadiness in a film-cooled environment.

Firstly, unsteadiness induced on the vane's surface by downstream rotor blade interactions was observed. Two studies conducted with uncooled testing apparatus observed temperature, pressure, and heat flux variations along the vane's suction side with downstream rotor blade passage. Compared to the rest of the airfoil surface, the highest disturbances in these values were most manifest along the suction side near the trailing edge of the vanes, as predicted by the work of Didier, Denos and Arts (2002: 6). Also, the propagation of the vane's reflected wake back upstream was seen as a pressure disturbance by Urbassik (2003), weakening with its movement backward. The propagation was replicated here as a temperature disturbance. This study has shown the repeated observation of the unsteady phenomenon with film-cooled airfoils. With the current testing, unsteadiness in pressure was seen as 11-12 % of the total upstream pressure near the trailing edge of the vane at 60 % span. This was five to six times the unsteadiness seen on the pressure side. However, temperature unsteadiness had no marked rise along the suction side's trailing edge. Along the entire surface, unsteadiness in temperature was approximately 0.08-0.1 % of the total upstream temperature. A lack

of markedly higher unsteadiness on the TE, SS indicates that the film cooling scheme (shaped, angled holes) did effectively keep the vane's surface cool, even with the rotor-induced unsteadiness. This lack of raised unsteadiness along the TE, SS is also evidence of the time it takes downstream temperature disturbances to propagate back upstream.

Along the rotor shroud (BOAS), high unsteadiness was seen along the latter part of the airfoil. Pressure unsteadiness totaled 40 % of the total upstream pressure at 86 % axial chord of the rotor, and temperature unsteadiness ranged from 0.41 to 0.26 % of the total upstream temperature at 47 % of the axial chord of the blades. The pressure data was compared to the studies of Polanka et al. (2002), conducted on the same test section, but without integrated cooling. General agreement between the cooled and uncooled cases was seen. Higher overall thermal unsteadiness was seen at a higher Reynolds number in both temperature and pressure along both the vane and the BOAS.

Time-averaged cooling parameter results were taken in comparison to the results taken on this same vane test section from Polanka et al. (2008), which was conducted without a downstream rotor. Values of overall effectiveness, adiabatic effectiveness, and film-cooled heat transfer coefficient were nearly consistent with those of the vane-only test section (Umholtz, 2007).

Also, it was seen that the 'Popp method' of determining cooling parameters (h and η) could be useful at TRF (Popp et al., 2000). This derives cooling parameters from a relationship between heat flux and driving temperatures, highly useful in a blowdown facility such as TRF. The need to gain these parameters from a fully-established thermal state was seen, however. In using this method, it was realized that both h and η could not

be determined when metallic temperatures of the airfoil showed high amounts of variance (~ greater than 0.5 °K). This was evident of a non-established steady state of heat transfer, rendering the Popp method of no use.

7.2 Significance of Research

Most importantly, this research sets the groundwork for engine design around the lastly-mentioned ‘unsteady envelopes’ of heat flux, temperature, and pressure that a turbine engine environment must endure. It also allows for further evaluation of the testing programs at TRF, showing that the testing programs must include blowdown tests that run for as long a period as possible to allow for a steady thermal state to be reached.

7.3 Recommendations for Future Research

Further research would be most beneficial if it leads to an appreciation for the unsteady envelopes of heat flux through which the metallic components of an engine will pass, with specific focus on operating parameters of the cooling schemes (such as massflow ratios, temperature ratios, and the like). Also, if cooling parameters are to be gained from testing at TRF, these tests must be carefully conducted with proper parameters. Several high-frequency blade-pass phenomena were seen along both the rotor shroud and vane stage, further investigations with a more intent focus on these specific occurrences will allow greater understanding of their exact nature.

Appendix: Determination of the True Driving Temperature

In the methods described by Popp for determination of film cooling parameters, a most important piece of data is the recovery temperature, defined as a function of the freestream velocity and recovery factor (Popp et al., 2000: 4). To calculate this value, a series of preliminary steps were performed:

Firstly, profiles of flow at the inlet to the vane stage were found. To do this, values of the inlet total pressure and temperature (fore of the vane stage) were averaged for a single run (Run 1) over the ‘stable’ portion of the trial (3.5-4.5 seconds). This was intended to be representative of the inlet profiles common through the testing. The profile of the normalized vane inlet total pressure (as normalized by the average value over the span of the section, Z/S) is seen in Figure 83. The profile of the normalized vane inlet total temperatures (again, as normalized by the averaged value over the entire span) is seen in Figure 84.

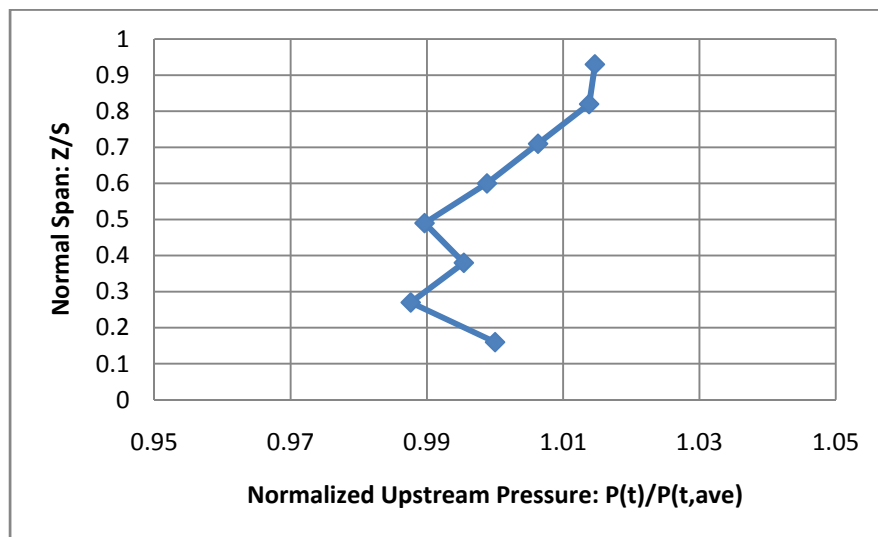


Figure 83: Normalized total pressure profile, vane inlet

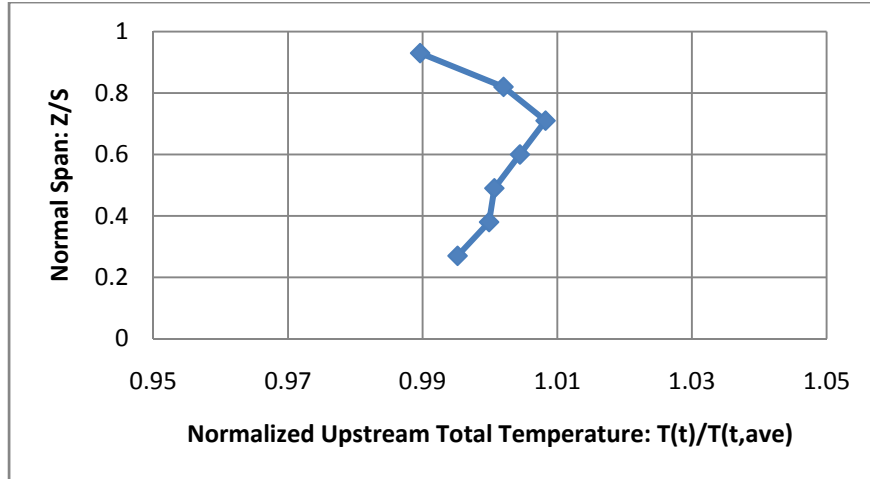


Figure 84: Normalized total temperature profile, vane inlet

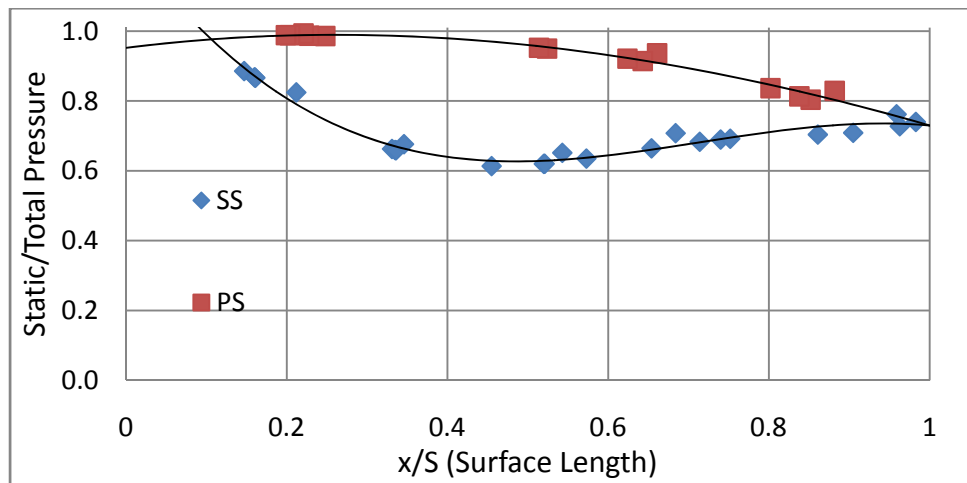


Figure 85: CFD-predicted local pressure ratio across vane surface

Next, pressure ratios were plotted and curve-fitted (static versus total pressures). For the vane, as seen in Figure 85, these values were calculated via CFD predictions at finite locations across the surface of the vane. The curve-fitted pressure ratios found in Figure 85 were applied to the isentropic relationship:

$$\left(\frac{P_s}{P_t}\right) = \left(1 + \frac{\gamma - 1}{\gamma} M^2\right)^{\frac{-\gamma}{\gamma - 1}} = \left(\frac{T_s}{T_t}\right)^{\frac{\gamma - 1}{\gamma}} \quad (26)$$

to find local Mach numbers. These sample local Mach numbers are seen in Figure 86.

Because flow was choked aft of the experimental section of the testing equipment, these locally-determined Mach numbers are constant through each run.

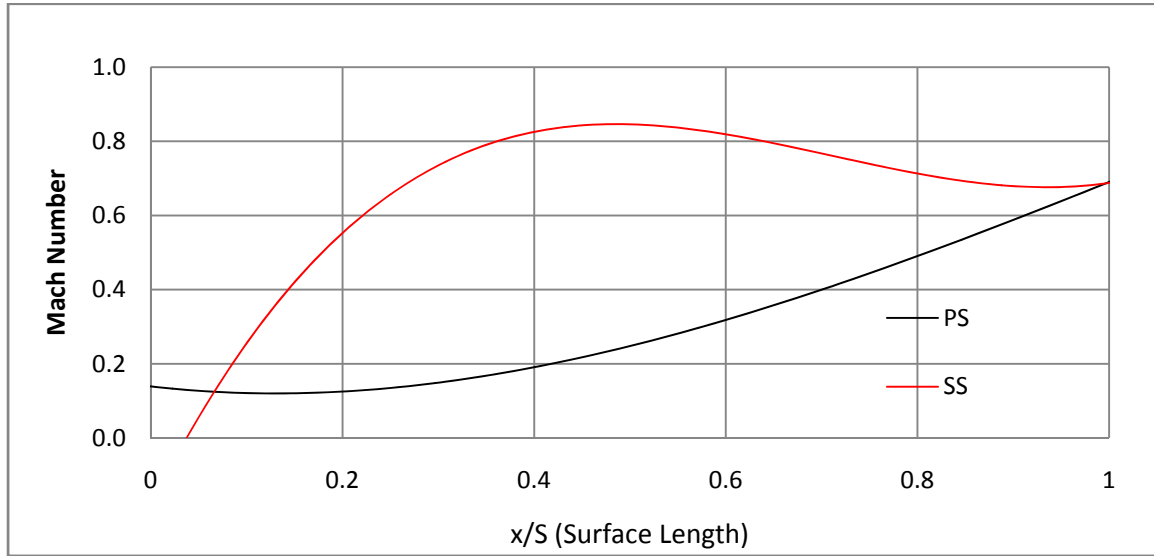


Figure 86: Vane local Mach numbers

The aforementioned isentropic relationship was used to find the inlet Reynolds numbers to each section. Local static temperatures and pressures for inlet pressure ratios and temperature ratios were found using the foremost gauges for the vane, from which these Reynolds numbers were determined, according to:

$$Re = \frac{\rho v l}{\mu} \quad (27)$$

where:

$$v = M \sqrt{\gamma R T} \quad (28)$$

The characteristic length used for the vane sections was the axial chord of the vane itself.

These Reynolds numbers are seen in Table 3.

From the sample local mach numbers and temperatures, local velocities were calculated. Gas specific heat (C_p) and Prandtl number (Pr) were gathered during the 3.5-4.5 second window. This allowed for calculation of a recovery factor, r , for turbulent flow defined as:

$$r = Pr^{1/3} \quad (29)$$

This is then used to calculate the recovery temperature from:

$$T_t - T_r = (1 - r) \frac{v^2}{2C_p} \quad (30)$$

The previous curve-fit temperatures and velocities were used to calculate sample recovery temperatures for the vane are plotted across the axial chord, as seen in Figure 87.

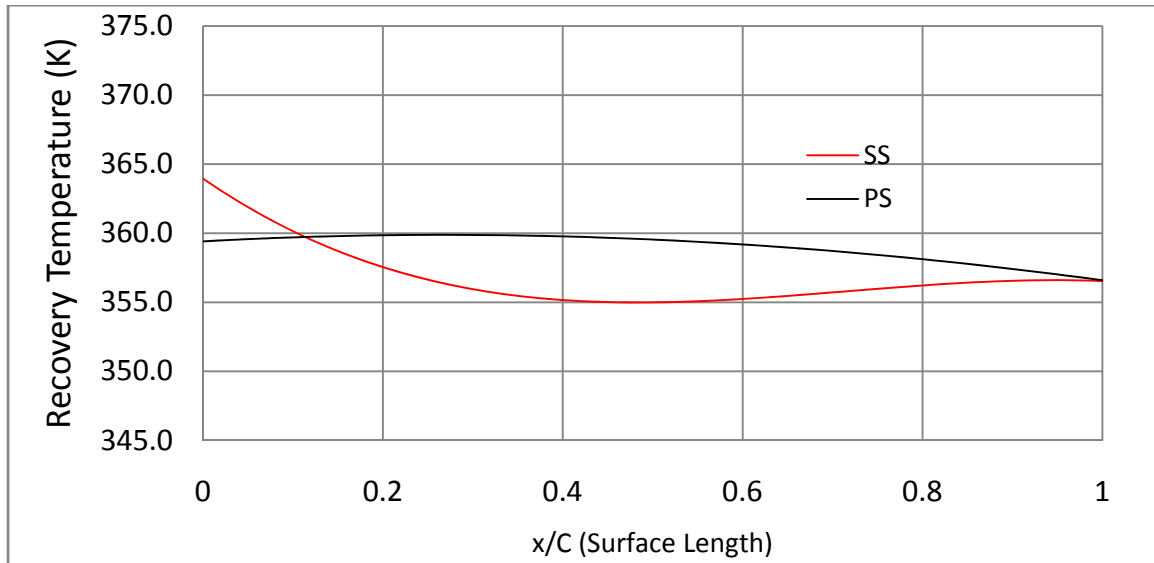


Figure 87: Sample vane local recovery temperatures

Before entering the rotor stage, as mentioned previously, minimal losses occur through the inlet guide vanes (Barringer et al., 2007), and seen in Figure 12. A nominal value of a 3.90-percent loss in total qualities (both total pressure and total temperature) was applied to closely find the total temperature at the inlet of the rotor stage (inter-, pre-, and post-stage losses were assumed to be zero, as the freestream flow moves unimpeded in these short axial distances). This was applied to the profiles of Figure 83 and Figure 84 to gain the rotor inlet total pressures.

Also, it must be realized that enthalpy is extracted as work is done by the fluid across the rotor (resulting in a lower driving temperature in the aft portions of the blade airfoils, as well as the aft of the rotor itself). This drop in enthalpy, corresponding to a drop in total qualities of the pressure and temperature across the rotor stage, was approximated as nearly linear. Thus, rotor's inlet and exit total pressures and temperatures (as averaged across the 3.5-4.5 second window) were used to form a linear relationship of these qualities along the BOAS. The profile of the normalized exit total pressure (as normalized by the average value over the span of the test section) exit is seen in Figure 88. The same was done for the temperature profiles, as seen in Figure 89.

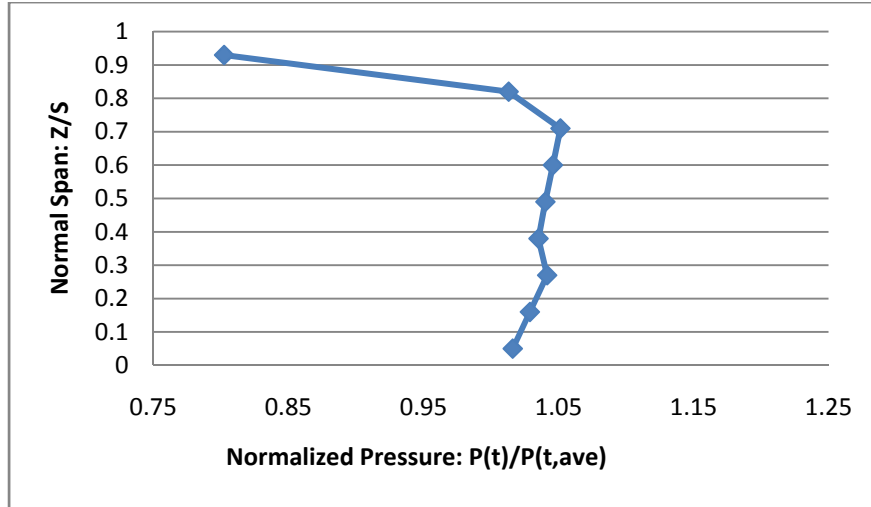


Figure 88: Normalized exit total pressure profile, rotor exit

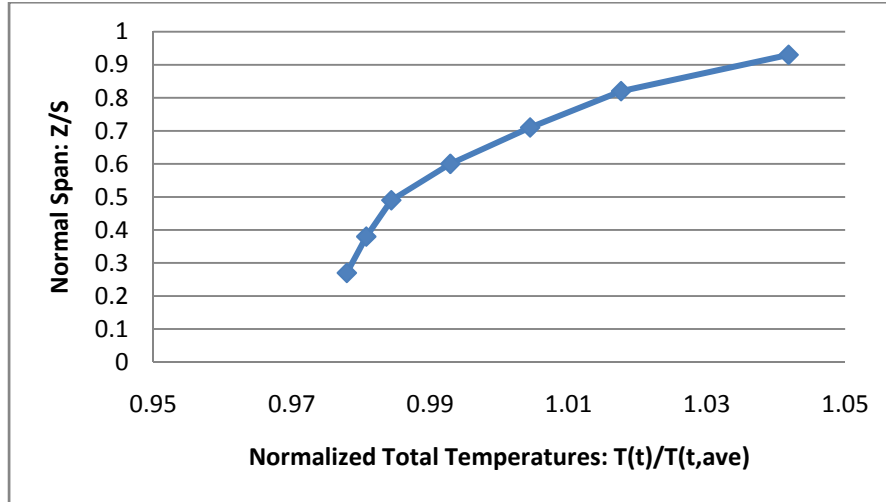


Figure 89: Normalized exit total temperature profile, rotor exit

The total losses through the rotor section were then normalized by their span-corresponding upstream total pressures and temperatures to gain a total pressure and temperature loss profile through the entire test section (as it leaves the rotor exit), as seen in Figure 90 and Figure 91.

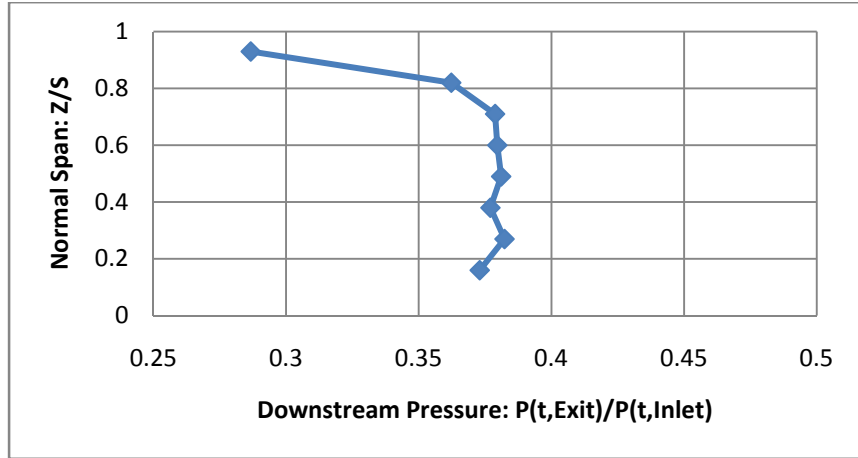


Figure 90: Total pressure loss profile through test section

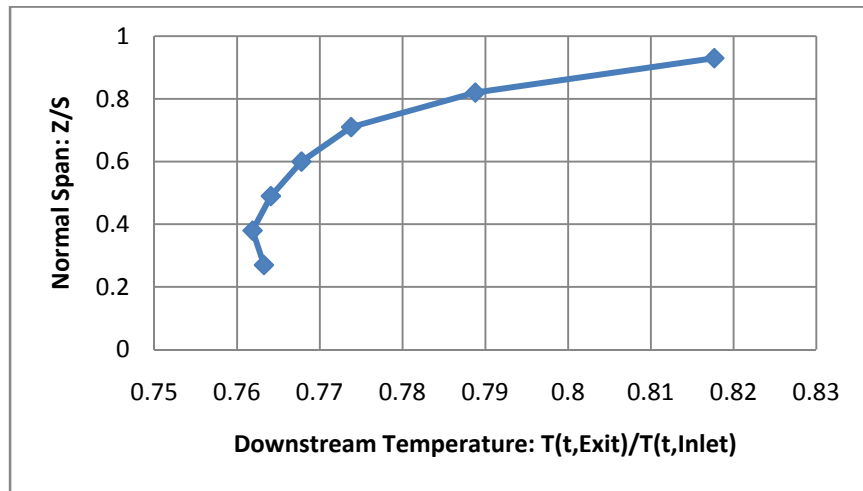


Figure 91: Total temperature loss profile through test section

These total values were plotted (assuming the linear losses through the rotor) to gain a ratio of total qualities (using isentropic relations to gain temperature ratios) to inlet total qualities as seen in Figure 92.

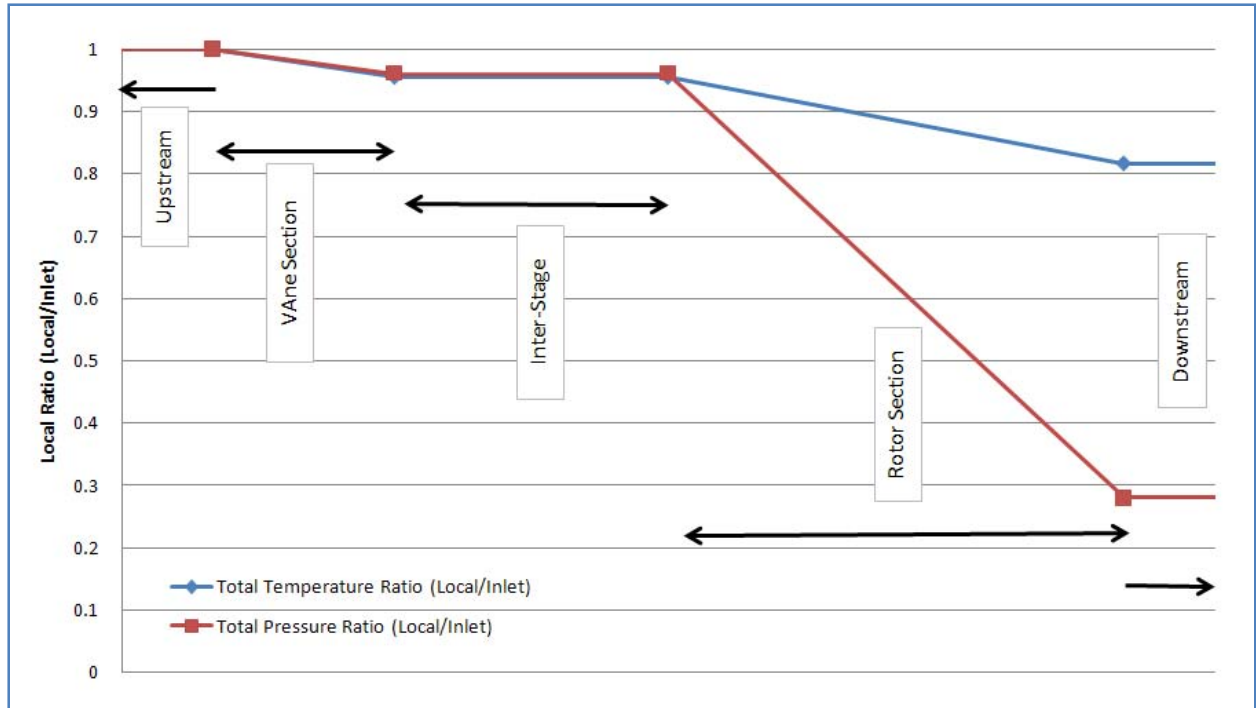


Figure 92: Temperature and pressure ratios across test section

This gave an appreciation for the local total temperatures and pressures at each point along the BOAS, most importantly. This allowed calculation of local Mach numbers in the rotor section.

For locations along the blade's outer air seal (BOAS), CFD predictions were not available. To gather pressure ratios at each of these locations, sample experimental data was applied. Values of the local static pressure (at each axial location of the BOAS) were averaged for a single run (Run 1) over the 'stable' portion of the trial (3.5-4.5 seconds). These values, divided by the local total pressures, as found in the linear relationship in Figure 92, were used to find the pressure ratios. These are plotted as finite points across the BOAS, to which a third-order polynomial curve-fitting was applied, as seen in Figure 93.

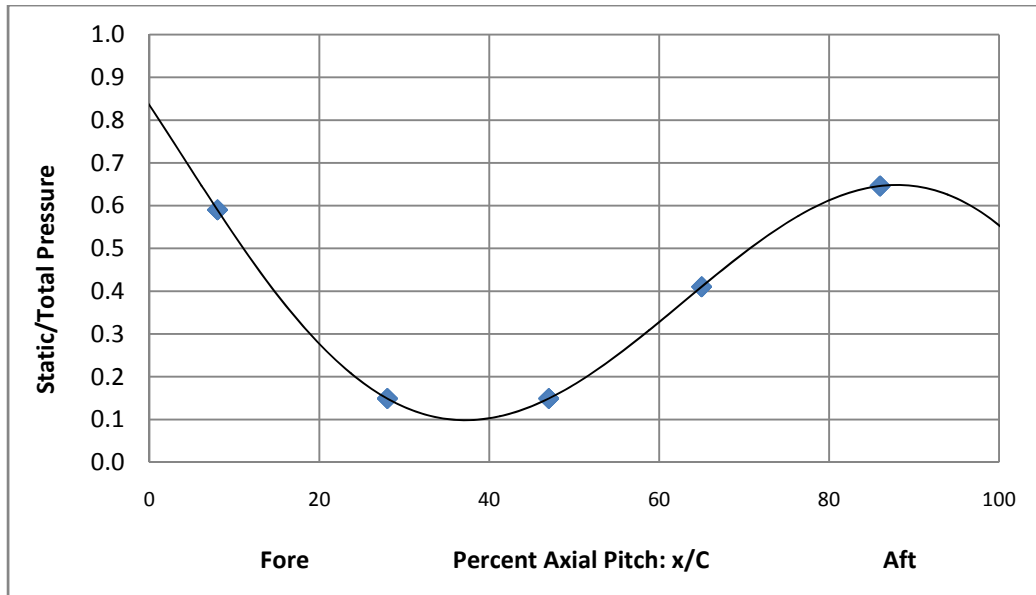


Figure 93: Experimentally-gathered local pressure ratios across BOAS

With these local pressure ratios, local time-averaged Mach numbers were determined, as seen in Figure 94. Local recovery temperatures were found through the relationships in Equations (29) and (30). These are shown in Figure 95: Sample BOAS local recovery temperatures. Finally, the BOAS-inlet Reynolds number was determined with data from the fore-most gauges for the section, as described previously in Equations (27) and (28). For the BOAS, the hydraulic diameter (used for the characteristic length in this flow) was taken to be half of the average rotor tip clearance.

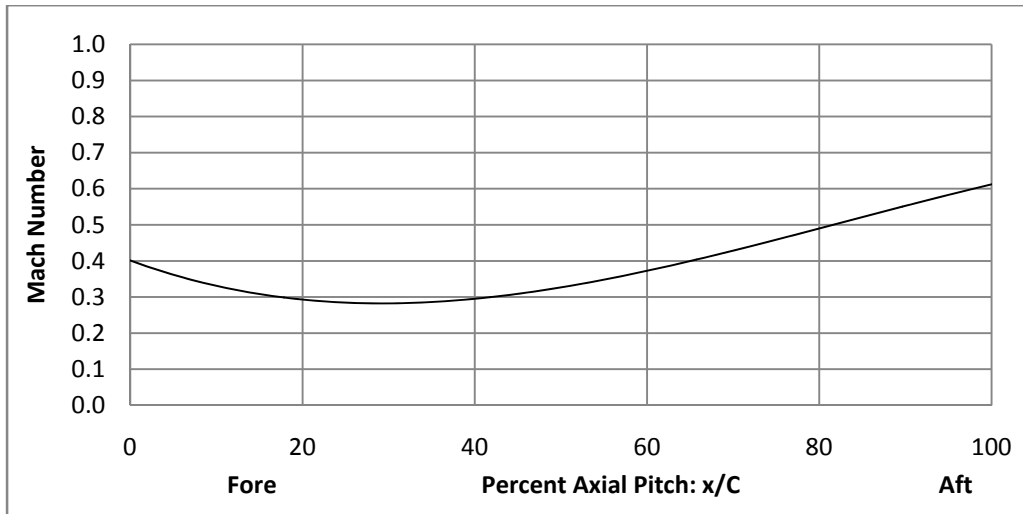


Figure 94: BOAS local Mach numbers

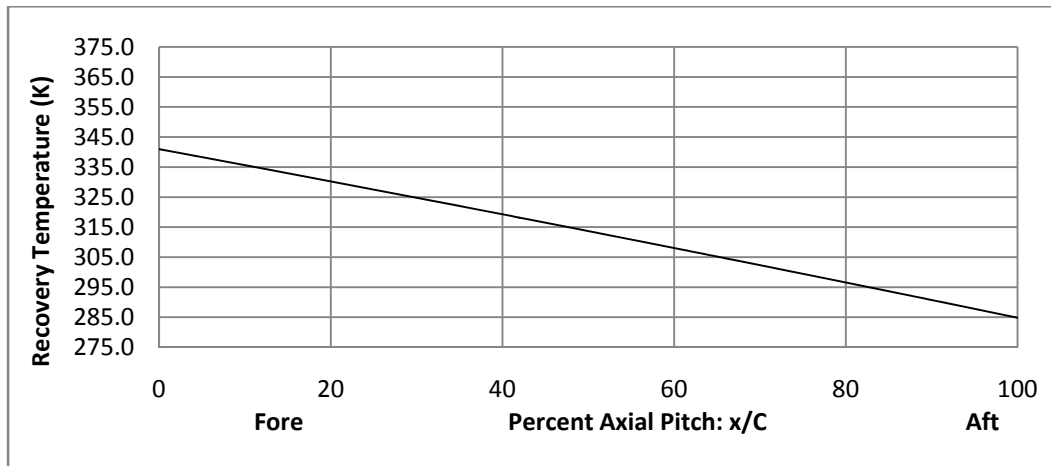


Figure 95: Sample BOAS local recovery temperatures

Bibliography

- Atkins, N.R., S.J. Thorpe, and R.W. Ainsworth, "Unsteady Effects on Transonic Turbine Blade-Tip Heat Transfer," *Proceedings of the ASME Turbo Expo 2008*. Berlin, Germany: June 2008.
- Barringer, M.D., K.A. Thole, And M.D. Polanka. "Experimental Evaluation of an Inlet Profile Generator for High-Pressure Turbine Tests," *Proceedings of the ASME Turbo Expo 2006*. Barcelona, Spain: 2006.
- Barringer, M.D., K.A. Thole, M.D. Polanka, J.P. Clark, and P.J. Koch. "Migration of Combustor Exit Profiles Through High-Pressure Turbine Vanes," *Proceedings of the ASME Turbo Expo 2007*. Montreal, Canada: 2007.
- Bogard, D.B., Thole, K.A. "Gas Turbine Film Cooling," *Journal of Propulsion and Power*, 22: 259-270 (March 2006).
- Bunker, R.S., "The Effects of Manufacturing Tolerances on Gas Turbine Cooling," *Proceedings of the ASME Turbo Expo 2008*. Berlin, Germany: June 2008.
- Chana, K.S., and T.V. Jones, "An Investigation on Turbine Tip and Shroud Heat Transfer," *Journal of Turbomachinery*, 125: 513-520 (July 2003).
- Clark., J.P., M.D. Polanka, M. Meininger, and T.J. Praisner. "Validation of Heat-Flux Predictions on the Outer Air Seal of a Transonic Turbine Blade," *Journal of Turbomachinery*, 128: 589-595 (July 2006).
- Clark, J.P., G.M. Stetson, S.S. Magge, R.H. Ni, C.W. Haldemann, Jr., and M.G. Dunn. "The Effect of Airfoil Scaling on the Predicted Unsteady Loading on the Blade of a 1-and-1/2 Stage Transonic Turbine and a Comparison with Experimental Results," *Proceedings of the International Gas Turbine & Aeroengine Congress & Exhibition*. Munich, Germany: May 2000.
- Dider, F, R. Denow, and T. Arts, "Unsteady Rotor Heat Transfer in a Transonic Trubine Stage," *Proceedings of the ASME Turbo Expo 2002*. Amsterdam, The Netherlands: June 2002.
- Doorly, J.E., Oldfield, M.L.G., "The Theory of Advanced Multi-Layer Thin Film Heat Transfer Gauges," *International Journal of Heat and Mass Transfer*, 30: 1159-1167 (Number 6, 1986).
- Ekkad, Srinath V., Shichuan Ou and Richard B. Rivir. "A Transient Infrared Thermography Method for Simultaneous Film Cooling Effectiveness and Heat Transfer Coefficient Measurements from a Single Test," *Proceedings of the ASME Turbo Expo 2004*. Vienna, Austria: June 2004.

- Guo, S.M., C.C. Lai, T.V. Jones, M.L.G. Oldfield, G.D. Lock, and A.J. Rawlinson. "The Application of Thin-Film Technology to Measure Turbine-Vane Heat Transfer and Effectiveness in a Film-cooled, Engine-Simulated Environment," *Journal of Heat and Fluid Flow*, 19: 594-600 (May 1998).
- Haldeman, C.W., Dunn, M.G., MacArthur, C.D., and Murawshi, C.B. "The USAF Advanced Turbine Aerothermal Research Rig." *NATO AGARD Propulsion and Energetics Panel Conference Proceedings*. Antalya, Turkey: 1992.
- Johnson, J.J., J.P. Clark, and M.J. Flanagan. "RANS Simulations of Turbine Vane Heat Transfer in Short Duration, Shock-Tunnel Cascade Experiments," *Collection of Technical Papers--Proceedings of the 43rd AIAA/ASME/SAE/ASEE Joint Propulsion Conference and Exhibit*. Cincinnati OH: July 2007.
- Johnston, R.T., Reireisen, J.M., and Fleeter S. "Measured Rotor Wake and Potential Forcing Functions, Including Blade Row Interactions," *Journal of Propulsion and Power*, 14 (Number 2, 1998).
- Mailach, Ronald, and Vogeler, Konrad. "Aerodynamic Blade Row Interactions in an Axial Compressor, Part I: Unsteady Boundary Layer Development," *Proceedings of the ASME Turbo Expo 2003*. Atlanta GA: June 2003.
- Mailach, Ronald, and Vogeler, Konrad. "Aerodynamic Blade Row Interactions in an Axial Compressor, Part II: Unsteady Profile Pressure Distribution and Blade Forces," *Proceedings of the ASME Turbo Expo 2003*. Atlanta GA: June 2003.
- Miller, R.J., Moss, R.W., Ainsworth, R.W., and Harvey, N.W., 2003. "Wake, Shock, and Potential Field Interactions in a 1.5-Stage Turbine, Part I: Vane-Rotor and Rotor-Vane Interaction," *Journal of Heat and Fluid Flow*, 26: 694-708 (October 2005).
- Oldfield, M.L.G. "Impulse Response Processing of Transient Heat Transfer Gauge Signals," *Proceedings of the ASME Turbo Expo 2006*. Barcelona, Spain: 2006.
- Papalia, J. P.B. Lawless, and S. Fleeter. "Off-Design Transonic Rotor-IGV Unsteady Aerodynamic Interactions," *Collection of Technical Papers--Proceedings of the 38th AIAA/ASME/SAE/ASEE Joint Propulsion Conference and Exhibit*. Indianapolis IN: July 2002.
- Polanka, M.D., R.J. Anthony, David G. Bogard, and Mark F. Reeder. "Determination of Cooling Parameters for a High Speed, True Scale, Metallic Turbine Vane Ring," *Proceedings of the ASME Turbo Expo 2008*. Berlin, Germany: June 2008.

- Polanka, M.D., T. Gillaugh, R.J. Anthony, M.J. Umholtz, and M.F. Reeder.
 “Comparisons of Three Cooling Techniques in a High Speed, True Scale, Fully Cooled Turbine Vane Ring,” *Collection of Technical Papers--Proceedings of the 43rd AIAA/ASME/SAE/ASEE Joint Propulsion Conference and Exhibit*. Cincinnati OH: July 2007.
- Polanka, M.D., D. A. Hoying, M. Meininger, C. D. MacArthur. “Turbine Tip and Shroud Heat Transfer and Loading, Part A: Parameter Effects Including Reynolds Number, Pressure Ratio, and Gas-to-Metal Temperature Ratio,” *Proceedings of the ASME Turbo Expo 2002*. Amsterdam, The Netherlands: June 2002.
- Polanka, M.D., J.P. Clark, A.L. White, M. Meininger, and T.J. Praisner. “Turbine Tip and Shroud Heat Transfer and Loading, Part B: Comparisons between Predictions and Experiment Including Unsteady Effects,” *Proceedings of the ASME Turbo Expo 2003, Volume 5A: Heat Transfer*. Atlanta GA: June 2003.
- Popp, O., Smith, D.E., J.V. Bubb, H. Grabowski III, T.E. Diller, J.A. Schetz, W.F. Ng. “Investigation of Heat Transfer in a Film Cooled Transonic Turbine Cascade, Part II: Unsteady Heat Transfer,” *Proceedings of the International Gas Turbine & Aeroengine Congress & Exhibition*. Munich, Germany: May 2000.
- Sieverding, C.J., R. Hugues, and J-M Dese. “Turbine Blade Trailing Edge Flow Characteristics and High Subsonic Outlet Mach Number,” *Journal of Turbomachinery*, 125: 298-309 (April 2003).
- Simon, T.W., and J.D. Piggush, “Turbine Endwall Aerodynamics and Heat Transfer,” *Journal of Propulsion and Power*, 22: 301-310 (March 2006).
- Smith, D.E., J.V. Bubb, O. Popp, H. Grabowski III, T.E. Diller, J.A. Schetz, W.F. Ng. “An Investigation of Heat Transfer in a Film Cooled Transonic Turbine Cascade, Part I: Steady Heat Transfer,” *Proceedings of the International Gas Turbine & Aeroengine Congress & Exhibition*. Munich, Germany: May 2000.
- Srinivasan, V., and R.J. Goldstein. “Effect of Endwall Motion on Blade Tip heat Transfer,” *Journal of Turbomachinery*, 125: 267-273 (April 2003).
- Sweeney, P.C., and J.F. Rhodes, “An Infrared Technique for Evaluating Turbine Airfoil Cooling Designs,” *Journal of Turbomachinery*, 122: 170-177 (January 2000).
- Umholtz, M.J. *A Comparison of Film Cooling Techniques in a High-Speed, True Scale, Fully-Cooled Turbine Vane Ring*. MS Thesis, AFIT/GAE/ENY/07-J21. Graduate School of Engineering and Management, Air Force Institute of Technology (AU), Wright-Patterson AFB OH, September 2007.
- Urbassik., Ryan M. *Vane/Rotor Unsteady Aerodynamics of a Single-Stage High-Pressure Turbine*. MS Thesis. Wright State University, Dayton OH, 2003.

Wade, P.C., P.I. King, and E.J. Jumper. "Pressure Disturbances from Compressor Vanes Forced by Vortex Shedding from Downstream Cylinders," *Collection of Technical Papers--Proceedings of the 38th AIAA/ASME/SAE/ASEE Joint Propulsion Conference and Exhibit*. Indianapolis IN: July 2002.

Vita

Jonathan Mason is a graduate of the U.S. Naval Academy. After AFIT, he will enter primary flight training for the U.S. Navy.

REPORT DOCUMENTATION PAGE			Form Approved OMB No. 0704-0188		
<p>The public reporting burden for this collection of information is estimated to average 1 hour per response, including the time for reviewing instructions, searching existing data sources, gathering and maintaining the data needed, and completing and reviewing the collection of information. Send comments regarding this burden estimate or any other aspect of this collection of information, including suggestions for reducing this burden to Department of Defense, Washington Headquarters Services, Directorate for Information Operations and Reports (0704-0188), 1215 Jefferson Davis Highway, Suite 1204, Arlington, VA 22202-4302. Respondents should be aware that notwithstanding any other provision of law, no person shall be subject to any penalty for failing to comply with a collection of information if it does not display a currently valid OMB control number. PLEASE DO NOT RETURN YOUR FORM TO THE ABOVE ADDRESS.</p>					
1. REPORT DATE (DD-MM-YYYY) 19-06-2008		2. REPORT TYPE Master's Thesis		3. DATES COVERED (From — To) 15 JUNE 2007- 19 JUNE 2008	
4. TITLE AND SUBTITLE Heat Transfer due to Unsteady Effects as Investigated in a High-Speed, Full-scale, Fully-cooled Turbine Vane and Rotor Stage			5a. CONTRACT NUMBER		
			5b. GRANT NUMBER		
			5c. PROGRAM ELEMENT NUMBER		
6. AUTHOR(S) Mason, Jonathan R.			5d. PROJECT NUMBER		
			5e. TASK NUMBER		
			5f. WORK UNIT NUMBER		
7. PERFORMING ORGANIZATION NAME(S) AND ADDRESS(ES) Air Force Institute of Technology Graduate School of Engineering and Management (AFIT/EN) 2950 Hobson Way WPAFB OH 45433-7765			8. PERFORMING ORGANIZATION REPORT NUMBER AFIT/GAE/ENY/08-J04		
9. SPONSORING / MONITORING AGENCY NAME(S) AND ADDRESS(ES) Dr. Marc Polanka, AFRL/RZTE 1950 Fifth Street WPAFB, OH 45433-7251			10. SPONSOR/MONITOR'S ACRONYM(S)		
			11. SPONSOR/MONITOR'S REPORT NUMBER(S)		
12. DISTRIBUTION / AVAILABILITY STATEMENT APPROVED FOR PUBLIC RELEASE; DISTRIBUTION UNLIMITED					
13. SUPPLEMENTARY NOTES					
14. ABSTRACT Experiments were conducted to examine the effects of film cooling on a gas turbine engine's high-pressure turbine section. The focus for this effort was in the tip/shroud region of a rotor stage and a high pressure turbine vane. A primary goal was to understand the unsteady flow effects. Attempts were also made to characterize the effects as caused by the fully-cooled rotor stage. Data for this investigation was taken at the U.S. Air Force's Turbine Research Facility (TRF), a transient blow-down facility with instrumentation fitted to a full-scale, high-speed, fully-cooled vane and rotor stage of proprietary design. Measurements of pressure, temperature, and heat flux were taken at flow conditions non-dimensionally matched to actual engine operation. From this high speed data the relevant film-cooling parameters (heat transfer coefficients, film cooling effectiveness, and overall effectiveness) were determined over a range of operating conditions. Of specific interest were the high frequency events associated with the blade passage frequency on both the vane and shroud surfaces. It was found that tip flow and vane wake-rotor interaction result in noticeable heat flux variations in time.					
15. SUBJECT TERMS Film-cooling, Adiabatic effectiveness, overall effectiveness, unsteady heat transfer, TRF, rotor shroud					
16. SECURITY CLASSIFICATION OF:			17. LIMITATION OF ABSTRACT U	18. NUMBER OF PAGES 137	19a. NAME OF RESPONSIBLE PERSON Dr. Mark F. Reeder
a. REPORT U	b. ABSTRACT U	c. THIS PAGE U			19b. TELEPHONE NUMBER (Include Area Code) (937) 255-3636, ext 4530; e-mail: mark.reeder@afit.edu